Confinement of Colloidal Liquid Crystals

Oliver James Dammone

University College
University of Oxford

Supervisors: Dirk Aarts and Pavlik Lettinga

A thesis submitted for the degree of
Doctor of Philosophy

Hilary Term 2013

"the journey is the destination"

Abstract

The behavior of colloidal liquid crystals in confinement is addressed on the single particle level using laser scanning confocal microscopy. We seek to disentangle how equilibrium director fields are controlled by the complex interplay between confinement, elasticity and surface anchoring.

First, we study the nematic phase confined to wedge structured channels. Varying the wedge opening angle leads to a splay to bend transition mediated by a defect in the bulk of the wedge. Our results are in quantitative agreement with lattice Boltzmann simulations, and we show that comparison between experiments and simulation yields a new method to obtain the splay-to-bend elasticity ratios of colloidal and biological liquid crystals. Next, we extend our study of the wedge structured channels to the cholesteric phase, and measure a splay to twist transition with increasing wedge angle. We directly visualise the 3D nature of the twisted state, and explain how the transition is intricately determined by the anchoring strength and the splay, bend, and twist elasticities. Next, we investigate the effect of rectangular confinement on the nematic phase. The rectangle aspect ratio is systematically varied and we observe five distinct director fields. Comparison with computations of the Frank-Oseen energies yields the extrapolation length, which we find to be of the order of the rod length. Next, we confine the nematic phase to annular geometries of varying dimensions, and observe the novel director fields that are adopted. We approach a level of confinement which is of the order of the particle size. Interpreting our observations with Monte Carlo simulations, which take into account the finite size of the particles, illuminates the applicability of continuum theories down to microscopic lengthscales. We finish with a study of the isotropic-nematic interface in bulk and confinement. We show that parallel anchoring occurs at the interface, and measure the width of the interface to be of the order of the rod length.

Declaration

This thesis is submitted for the degree of Doctor of Philosophy in Physical and Theoretical Chemistry at the University of Oxford. No part of this thesis has been accepted or is currently being submitted for any degree, diploma, certificate or other qualification in this University or elsewhere. This thesis is wholly my own work, except where indicated.

Contents

Chapter 1

Introduction

1.1 Liquid crystals

Liquid crystals are an array of phases that exist between the liquid and solid phase [1,2]. As the name implies the properties are intermediate of a liquid and a crystal. A crystal has a regular repeating pattern of molecules and is characterised by elasticity, whereas a liquid has no long range molecular order, is able to flow, and is characterised by viscosity. A liquid crystal is able to flow like a liquid, but molecular order exists in at least one dimension. Liquid crystals arise due to the anisotropy of the particles: the particles have a direction. In reality this means the particles are rod [3,4] or disk [5,6] shaped, or a variant of these two shapes, such as 'banana' [7,8] and board-like [9, 10] particles. In this thesis we focus on liquid crystals formed by rod-shaped particles.

Several liquid crystalline phases exist with increasing order: nematic, smectic and columnar, and in figure 1.1 we illustrate the ordering of some of the more common phases [11]. The phases displayed vary from one liquid crystal to another, and it is not fully understood why different liquid crystalline molecules exhibit different phases. The phase transitions from an isotropic liquid to higher order liquid crystalline phases are triggered by decreasing the temperature, or by increasing the concentration, and the respective liquid crystals are called thermotropic or lyotropic. The lyotropic phase transitions from lower to higher symmetry are driven by an entropy gain of the system, as explained by Onsager in 1949 [12].

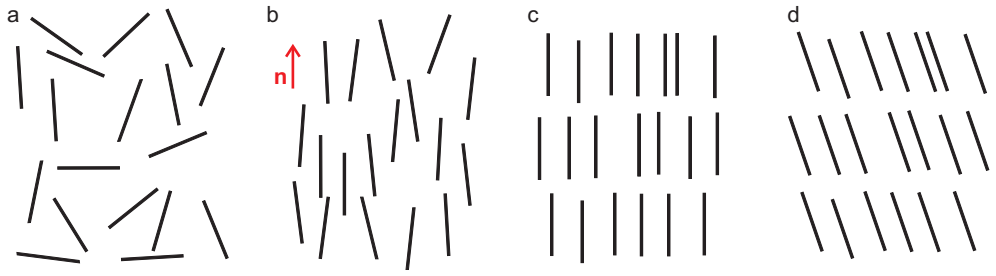

Figure 1.1: Schematic illustration of the order in the: (a) isotropic, (b) nematic, (c) smectic A, and (d) smectic C phases.

The defining characteristic of the nematic phase is that all the particles are orientated along a common axis, called the director, which at a given position, $\mathbf{r}$, points in the direction of a unit vector, $\mathbf{n}(\mathbf{r})$. Due to symmetry the states $\mathbf{n}$ and -$\mathbf{n}$ are indistinguishable. A uniformly aligned nematic is strongly birefringent. The fluidity of the nematic phase comes from the ease with which particles can slide along each other while maintaining their preferred axis of orientation.

The cholesteric phase is a chiral nematic phase in which the director rotates along an axis, creating a helical distortion, as illustrated in figure 1.2(a). It is very similar in energy to the nematic phase and liquid crystals will naturally adopt either a nematic or a cholesteric phase, but not both. The twist may be left or right handed depending on the specific liquid crystal. The phase is quantified by the cholesteric pitch, p, the distance over which the director, $\mathbf{n}$, rotates 360° [13]. We note that with $\mathbf{n}$ and -$\mathbf{n}$ being equivalent the period of repetition is half the pitch. If we arbitrarily choose the helical axis to be the z-axis then $\mathbf{n}$ reads:

$$n_x = \cos(q_0 z + \theta) \qquad n_y = \sin(q_0 z + \theta) \qquad n_z = 0, \tag{1.1}$$

where θ is the angle between the rod and the x-axis, and $p = 2\pi/q_0$. An optical property of cholesterics is that the helical structure gives rise to Bragg reflections at wavelengths equal to the pitch. Consequently, if the pitch is equal to a wavelength of light in the visible spectrum a colour is observed [14,15]. Since the pitch is very sensitive to temperature, for thermotropic liquid crystals, this property has been exploited to create liquid crystal thermometers and temperature sensors [16, 17].

Smectic phases are identified by the the molecules being arranged in layers in addition to having a common director. Several smectic phases have been observed with varying degrees of positional and orientational order [1, 11]. In figure 1.1, we illustrate the smectic A phase

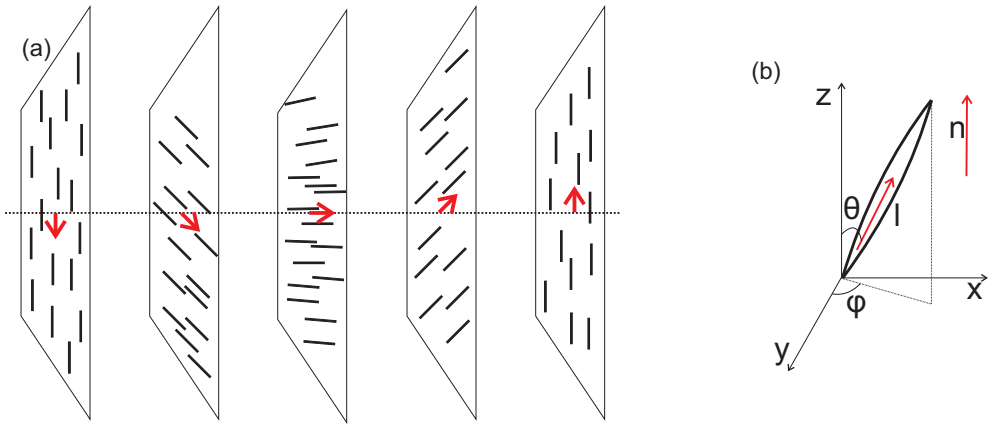

Figure 1.2: (a) Schematic illustration of the twist of the cholesteric phase. (b) Angles and vectors required to define the order parameter. The director, **n**, is taken to be pointing along the z-axis and we define θ as the angle between the z-axis and a unit vector, **l**, along the molecular axis of the rod.

where the layers are perpendicular to the director, and the smectic C phase where the director is tilted in each layer. The fluidity arises from the lateral forces between the molecules being much greater than the interlayer forces enabling layers to slide over each other. Smectic phases are much more viscous than nematic phases due to the greater order.

The columnar phase is characterised by the molecules arranging themselves into columns, with no long range order existing along the columns. The columns are packed hexagonally or rectangularly [18, 19], and in some columnar phases the molecular axis is tilted relative to the column axis [20, 21].

1.1.1 Order parameter

It is essential to define a parameter to quantify the degree of ordering of the nematic phase to distinguish it from the isotropic phase and to calculate how external factors influence the degree of ordering. Firstly, the director **n** is taken to be pointing along the z-axis and we define θ as the angle between the z-axis and a unit vector, **l**, along the molecular axis of the rod, see figure 1.2(b). The distribution of rods can then be described by the function $f(\theta)d\Omega$, which gives the probability of finding a rod in a small solid angle around (θ, ϕ). Thus the director **n** is given by the angles where $f(\theta)$ peaks. The function f is independent of ϕ as the nematic has complete cylindrical symmetry about **n**. The simplest way of defining the degree of alignment is by using

the second Legendre polynomial, first quantified by Tsvetkov [22]:

$$q =< P_2(\cos\theta) >= \frac{1}{2} < 3\cos^2\theta - 1 > . \tag{1.2}$$

The square brackets denote an ensemble average over $f(\theta)$. For a perfectly aligned nematic phase $q = 1$, while for an isotropic phase $q = 0$. We note, that for lyotropic liquid crystals, $q = 1$ will only occur at $T = 0K$ due to thermal fluctuations. Equation (1.2) assumes that the liquid crystal consists of rigid rods which have complete cylindrical symmetry about **l**. However, since many liquid crystal molecules are flexible, a more complicated parameter has been defined without assuming rigidity [23]. For the liquid crystals used in this thesis eq. (1.2) is sufficient.

1.1.2 Non-ideal director fields

The nematic director field can be easily distorted. The slightest external perturbation, for example the presence of a micrometer sized particle, can trigger a significant distortion to the director field [24]. The director field is also very sensitive to more substantial external factors such as confining surfaces, shear forces, electric and magnetic fields. The result is that a perfect undistorted nematic will very rarely exist, and much of the interest in liquid crystals is focused on understanding these distortions. The director field can either change continuously, creating textures called deformations, or it can change suddenly creating disclinations/defects [1]. When nematics are viewed between crossed polarisers the deformations and defects result in the characteristic threadlike (Schlieren) texture and single points, observed [25].

All continuous changes in **n** can be described by either one, or a combination of the splay, bend and twist deformations, which are illustrated in figures 1.3(a) - (c). The deformations have an elastic energy cost F_e that can be determined from the director **n** using the Frank-Oseen energy [26, 27]:

$$F_e = \frac{1}{2}K_1(\text{div } \mathbf{n})^2 + \frac{1}{2}K_2(\mathbf{n} \cdot \text{curl } \mathbf{n})^2 + \frac{1}{2}K_3(\mathbf{n} \times \text{curl } \mathbf{n})^2. \tag{1.3}$$

The elastic constants K_i with $i = 1, 2, 3$ are associated with the splay, twist and bend deformations, respectively, and indicate the respective energy costs for a given liquid crystal. These values depend on the specific physical properties of the molecules, with typical values being of the order $K \approx 10^{-13} - 10^{-11}$N [28–31]. From the reported experimental values we see that the bend

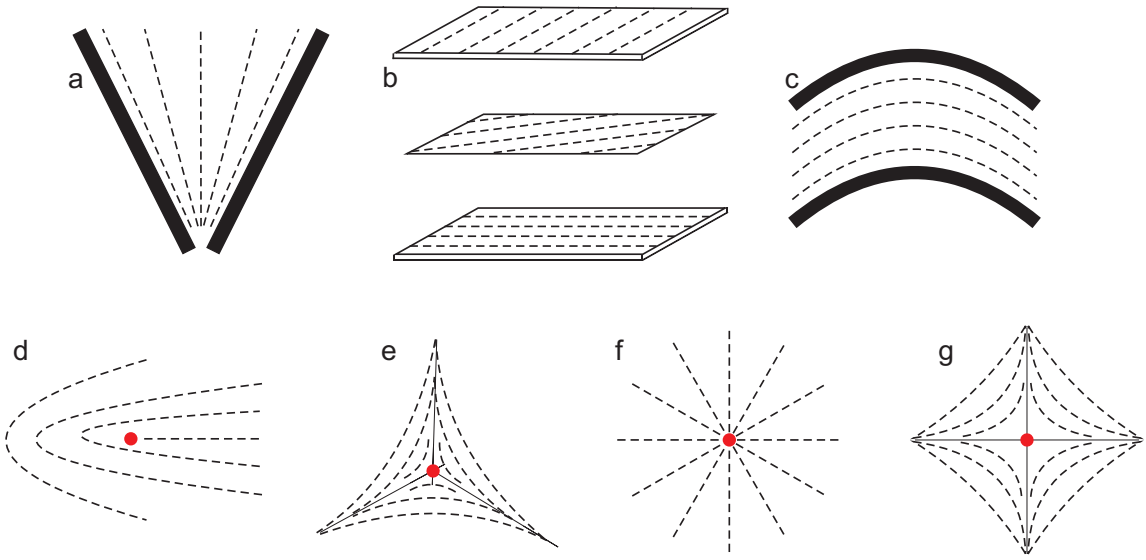

Figure 1.3: Top row, director field for three nematic deformations: (a) splay, (b) twist, and (c) bend. Bottom row, director fields in the region of four disclinations of strength: (d) $s = +1/2$, (e) $s = -1/2$, (f) $s = +1$, and (g) $s = -1$.

constant is typically larger than the splay and twist constants [1,11]. For a cholesteric phase the natural preferred twist is taken into account by including q_0 in the K_2 term; $\frac{1}{2}K_2(\mathbf{n}\cdot\text{curl }\mathbf{n}+q_0)^2$. *Saddle-splay* and *splay-bend* terms [27,32] can be added to eq. (1.3). The need for them has been widely discussed, and they are often ignored, but it has been proposed that they are important for liquid crystals adjacent to interfaces [33, 34]. Equation (1.3) has been used extensively in theoretical work on nematics [35–37]. In many calculations a one constant approximation is used as eq. (1.3) is too complex to solve analytically [33, 38].

Non-continuous variations in the director field occur as lines or points and four types are illustrated in figures 1.3(d) - (g) [27, 39]. Disclination planes are never observed as they are unstable and will always be smeared out. Disclinations are labeled by their strength, s, which is determined by considering how the director changes around the disclination. We define $\mathbf{r}$ as the distance from the point of observation to the disclination, with $\phi(\mathbf{r})$ the angle between $\mathbf{r}$ and the x-axis and θ the angle between $\mathbf{n}$ and the x-axis. If we make one full loop around the disclination ($\triangle\ \phi = 2\pi$), the strength of the disclination is given by the rotation of the director; $\triangle\ \theta = 2\pi s$.

1.1.3 Anchoring

Anchoring is the phenomenon where surfaces disturb liquid crystal ordering by imposing a preferred molecular orientation and a preferred degree of order [1, 40]. The most common types of anchoring are planar and perpendicular (homeotropic) ordering with respect to the surface. The extrapolation length, ξ, identifies if nematic elasticity or surface anchoring, w, is the dominating factor. It is defined as:

$$\xi = \frac{K}{w}, \tag{1.4}$$

where K is a specific or average elastic constant. The anchoring, w, is of the order of E_{wn}/d^2, where E_{wn} is the interaction energy between one molecule and the surface, and d is a molecular dimension [1]. Similarly, an elastic constant has units of energy per length and is of the order E/d, where E is the interaction energy between molecules. Substituting into eq. (1.4) leads to the following scaling estimate:

$$\xi \approx d\frac{E}{E_{wn}}. \tag{1.5}$$

In the strong anchoring regime the surface dominates and elastic distortions are generated. It occurs when $E_{wn} \geq E$, and the extrapolation length becomes of the order of the molecular dimension; $\xi \lesssim d$. In contrast, in the weak anchoring limit the elasticity dominates and non-ideal anchoring occurs at the surface. It happens for $E_{wn} < E$, and ξ may become much greater than the molecular dimensions.

Often the approximation $E_{wn} \approx E \approx k\mathrm{T}$ is used, enabling values of ξ, K, and w to be obtained from a molecular dimension. For the colloidal rod *fd*, the approximation $K \approx k\mathrm{T}/d$ with d being the rod length, generates an average elastic constant K of 4.7×10^{-15} N. However the measured experimental value is two orders of magnitude lower; $K_2 \approx 4.2 \times 10^{-13}$ N[1] [31]. Implying that for *fd* the rod-rod interaction energy differs from the rod-wall interaction energy and that the approximation should be used with caution.

[1]The exact K_2 measurement depends on the nematic concentration and ionic strength.

1.2 Colloids as model systems

Colloids are particles dispersed in a solvent with one length in the range of 1 nm to 1 μm [41,42]. There are numerous examples in everyday life, ranging from milk to fog: roughly speaking, milk is a colloidal suspension of fat globules in water and fog is a suspension of liquid drops in air. The key feature of colloidal particles is that they exhibit Brownian motion: the random collisions of solvent particles with the colloidal particles leads to the characteristic erratic motion of the colloids. Both molecules and colloids have an average translational kinetic energy of $\frac{3}{2}k_BT$ [43], with k_B the Boltzmann factor and T the temperature. This analogy can be carried further, e.g. to the osmotic pressure exerted by a dilute suspension of colloids or by a dilute solution of solute molecules [44]. These analogies allow colloids to be viewed as large atoms. However single colloids are much more accessible than atoms as their size enables them to be directly observed via various forms of microscopy. Their diffusion rates are significantly lower making it possible to observe certain phenomena in greater detail [45, 46]. Additionally, the strength of colloidal interactions can be tuned, e.g. by adding a non-absorbing polymer which creates an attractive force between the particles via a depletion interaction [47, 48].

In this thesis we focus on the behaviour of rod shaped colloids. There are several synthetic synthesis routes to produce colloidal rods that form liquid crystalline phases. Maeda observed nematic and smectic phases for suspensions of β-FeOOH, selenium, and nickel dimethylglyoxime rods [4]. Boehmite rod systems are well established in the literature and their phase behavior has been explored in detail [49–51]. Recently a silica rod system has been produced [52] and current experiments indicate it will be possible to produce phase separating samples. However these synthetic routes come with one of both of the following disadvantages: high refractive index of the suspensions making 3D visualisation difficult, and/or polydisperse suspensions. An alternative to synthetic routes is to use a biological liquid crystal such as the rod-like tobacco mosaic virus (TMV) [53] or *fd* virus [54]. *Fd* has attracted more attention than TMV, as its aspect ratio is greater, and the synthesis of TMV is very involved and time consuming: tobacco plants must be grown and then infected with the virus, and the virus is then obtained by extracting it from the plants [55]. The key advantage of a virus system is the high monodispersity of the samples, as viruses replicate by cloning [56]. This enables a direct comparison with theory and simulation by avoiding the complication of polydispersity. The usual colloidal advantages are presented as well: the viruses can be modified after they have been expressed [57]. For example, the polymer

polyethylene glycol can be covalently bonded to the *fd* virus, changing the dimensions and also sterically stabilising the virus [58]. Another example is that the *fd* virus can be fluorescently labeled, and due to the size, this enables the viruses to be visualized using laser scanning confocal microscopy.

Here we use the wild-type *fd* virus (referred to as *fd*) as a model rod like colloid. It is a polyelectrolyte with a contour length of 0.88 μm and a diameter of 6.6 nm [59]. It consists of a single strand of DNA, about which roughly 2700 copies of the major coat protein pVIII are helically wrapped. Above pH 4 *fd* is negatively charged and interacts via a combination of electrostatic repulsions and hard core interactions. At low virus concentrations the system displays an isotropic phase. Upon increasing concentration the virus exhibits a cholesteric phase and then higher order smectic and columnar phases [18]. A biphasic region occurs between each of the phase transitions, where the virus will phase separate into the two phases. We note that a cholesteric phase is very similar in energy to a nematic phase and in this thesis we will often refer to the cholesteric as the nematic phase, which is common practice in the literature. There are several variations of the *fd* virus that have a minor difference in their genetic code, triggering a difference in one specific physical property such as; contour length, flexibility, or charge [60,61]. This creates ideal model systems for testing theories on liquid crystals and allows one to tune the bulk properties of the materials. In this thesis we will also use Y21M-*fd* (referred to as Y21M). The only physical difference between *fd* and Y21M is a single amino acid of the major coat protein pVIII. This gives rise to a difference in flexibility; *fd* is a semi-flexible rod with a persistence length of 2.8$\pm$0.7 μm, whereas Y21M is a rigid rod with a persistence length of 9.9$\pm$1.6 μm [62]. Due to their identical dimensions both rods have an aspect ratio of $\sim$133, which is compatible with Onsager theory (valid for aspect ratios $\gtrsim$100) [12]. In addition, the fact that Y21M is a rigid rod, has allowed for the first quantitative test of Onsager theory [62] [2].

[2] A detailed explanation of Onsager theory is given in chapter 7.

1.3 Thesis outline

This thesis is focused on studying the behaviour of colloidal liquid crystals in confinement, on the single particle level. In an effort to explore and understand the interplay between geometrical boundary conditions and elastic distortions. As of yet, very little work has looked at lyotropic liquid crystals in confinement. Thermotropic liquid crystals have been studied in confinement. With recent examples being: confinement induced transitions of defects [63], nematics confined to sinusoidal grooves [64], and the effect of shell confinement on smectic ordering [65]. However, no studies have been carried out at the single particle level, presumably because the thermotropic particle size is on the nanometer scale.

We begin in Chapter 2 by describing the *fd* virus suspensions, the soft lithography protocols, and the microscope setup. Chapter 3 examines the nematic phase confined to wedges of varying opening angle. A splay-bend transition occurs, mediated by a defect in the centre of the wedge. The measurements are compared to Lattice Boltzmann simulations, enabling us to demonstrate that the transition angle and position of the defect depends on the splay and bend elastic constants. In Chapter 4 we extend the problem to the cholesteric phase by decreasing the pitch of the system. A splay-twist transition is observed, and we directly visualise the 3D nature of the problem. Chapters 5 and 6 present the nematic phase in rectangular and annular 2D confinement, where the features become the order of the rod length. The rectangular confinement results are compared to Frank-Oseen energy computations, enabling the extrapolation length to be estimated. The annular confinement results are interpreted in light of recent Monte Carlo simulations. We reach levels of confinement where the finite size of the rod length becomes relevant which may imply a deviation from continuum theory. In Chapter 7 we demonstrate that the isotropic-nematic can be observed at the single particle level. We discuss why reducing the sample volume to the micrometer scale decreases phase separation times and we measure the width of the interface. We finish with a summary of the main statements of this thesis.

Chapter 2

Experimental system

Abstract

We outline the virus synthesis protocols and explain the soft lithography techniques, used to fabricate micrometer scale structures. Laser scanning confocal microscopy is the main imaging tool used in this thesis, and we discuss the optical set-up and its advantages. The image analysis routines that identify the rod's position and orientation are introduced as well.

2.1 Virus sample preparation

The *fd* and Y21M viruses were grown by infecting a strain of *E.Coli* with the respective virus. The standard protocol [66] is outlined in the appendix. The yield is approximately 50 mg of virus per litre of infected bacteria. We dispersed the virus in 20 mM tris buffer at pH 8.15 with 100 mM NaCl and 15% EtOH. The ethanol was added to prevent the growth of bacteria. The concentration of *fd* and Y21M samples were measured using UV spectrometry. The optical densities are 3.84 cm^{-1} and 3.63 cm^{-1}, respectively, at 269 nm for a path length of 1 cm [62].

The viruses were fluorescently labeled with the ester Alexa-488 by mixing 1 mg of virus with 1 mg of the dye [67]. The dye reacted with the free amine group on the virus surface forming covalent bonds. The reaction was carried out in small volumes $\sim$100 μm to ensure high labeling, and excess dye was removed by centrifugation steps. There were approximately 300 dye molecules per virus, determined by absorbance spectroscopy. We found the phase behaviour of the labeled and unlabeled viruses to be very similar [57]. We thus assume the interaction potential is very similar, with phase behaviour being a sensitive test of interaction potential. However we expect the flexibility and aspect ratio to change for the labeled virus, and this may affect the subtle chiral interactions between the individual particles. An anti-bleaching solution was added to the stock virus solution (2 mg/ml glucose oxidase, 0.35 mg/ml catalse, 30 mg/ml glucose and 5% β-mercaptoethanol).

Microscope samples had a ratio of labeled to unlabeled rods of approximately 1:25000. If the ratio was significantly greater than this, the whole sample would fluoresce, and we would not be able to image individual rods. If the ratio was significantly less than this, there would not be enough rods to see the subtleties of the director field.

We note that for both viruses we would observe dimers; double length particles containing two phage genomes [68]. Approximately 5-10 % of the labeled particles would be dimers, and we did not notice a difference between *fd* and Y21M. Polydispersity affects the phase behaviour by increasing the width of the isotropic-nematic biphasic region [69]. In our system the polydispersity will not have a significant effect, as we do not have a range of lengths, we simply have two lengths with 90-95 % of the particles being the same length.

2.2 Soft lithography: producing structures on the μm scale

Over the past 20 years creating channels on the μm scale has become inexpensive and quick through the technology of soft lithography [70]. With 1-100 μm being the lengthscale of colloidal particles and cells the soft matter and biological communities have made considerable use of this technology [71–73]. Soft lithography is attractive due to the small volumes of reagents required and also due to the minute physical size of the channels, which allows complex designs to be fabricated on a single slide, creating the idea of 'lab on a chip' [74]. In our case as the length of the *fd* virus is 0.88 μm, soft lithography provides the ideal tool to create confining channels. In addition, with the protocols being independent of the 2D design, only our imagination is the limiter to the type of channels we can create.

Figure 2.2 shows a schematic diagram of the standard protocols used to make the channels. In the initial steps photolithography was used to create an SU-8 structure on a chosen substrate (silicon wafer or glass slide) [75]. Firstly, SU-8 2000 (Micro Chem) was spin coated onto a substrate and then softbaked for 2 min 20 secs at 95°C, to remove the solvent and improve SU8-substrate adhesion. The wafer was then irradiated for 15 secs through a photomask with UV light (130 mJcm^2) and then baked for a second time for 3 min 30 secs at 95°C. The SU-8 was polymerized by the UV light and the second bake increased the polymerized regions stability. In a developing step, the unexposed regions of SU-8 were washed away (the exposed polymerized regions were insoluble). The SU-8 structure was then completed with a final hard bake step for 15 mins at 150°C, making the structure temperature stable. The type of SU-8 used, the exact baking, irradiation and development times depended primarily on the height of the structures (the greater the channel height, the longer the times), but also the complexity of the 2D shape. The numbers given here, were used to make wedge structured channels 10 μm high. Once the SU-8 structure was made, the channel could be made out of three materials as outlined below [76, 77].

SU-8: A device could be made directly onto a glass coverslip by following the protocol above. A glass coverslip was used as the substrate and the resulting SU-8 structure directly formed the channel walls. The channel was filled by pipetting a drop of the sample onto the structures, and then immediately sealed by clamping a glass slide with a very thin coating ($\lesssim 0.1$ μm) of PDMS. Finally, the edges of the glass slide would be sealed with wax to prevent leaking.

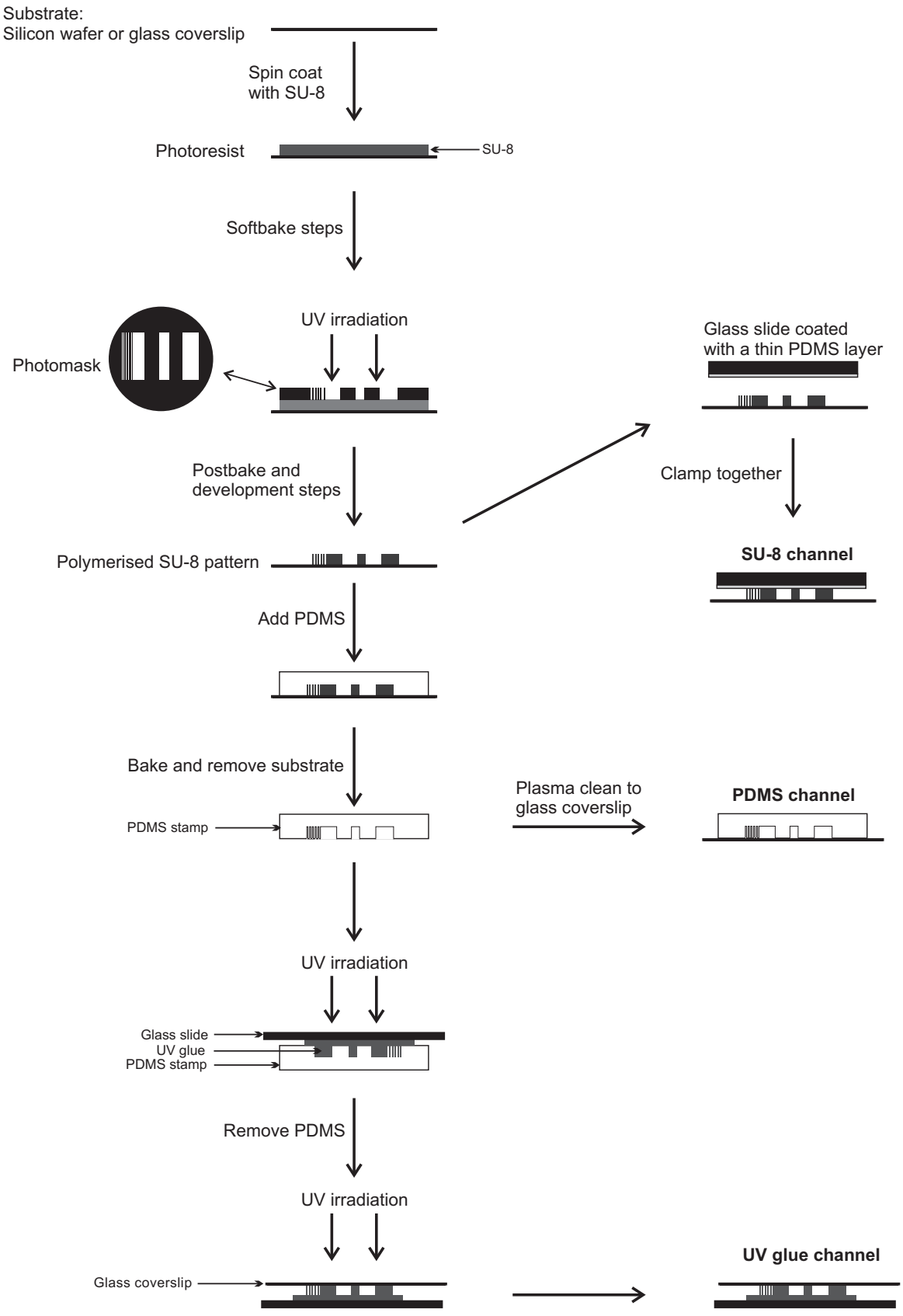

Figure 2.1: Schematic diagram of the soft lithography techniques.

Polydimethylsiloxane (PDMS): A silicon wafer was used as the substrate for the SU-8 structure. The resulting wafer was used as a mould to create a PDMS (Sylgard 184 silicon elastomer kit, Dow Corning) slab with the opposite structure indented. The silicon wafer mould could be used multiple times. Treating the PDMS slab and a glass coverslip with oxygen plasma, and then gently pressing the two together, caused them to covalently bond, creating a channel. The channels were designed so that they remained open, enabling them to be filled by capillary action, and then sealed with UV glue (Norland optical adhesive 81).

UV glue: A PDMS structure was created as described above, and this was then used as a mould for the UV glue (Norland optical adhesive 81). The UV glue was pipetted onto the PDMS and then irradiated. The PDMS was subsequently pealed off and a glass coverslip was quickly placed on top of the UV glue channel. The channel and glass coverslip were then immediately irradiated to bind them together. The channels were designed so that they remained open, enabling them to be filled by capillary action and subsequently sealed with UV glue. The irradiation times depended on the height of the channels, but typically we irradiated for 55 secs at 130 mJcm^2, for a channel 10 μm high.

PDMS channels were the quickest and cheapest to make, but unfortunately PDMS is permeable to air and solvents, causing samples to dry out in an hour. We used PDMS channels for initial experiments. Making channels out of SU-8 or UV glue avoided this problem, as both of the materials are impermeable to air; we were able to make channels, which would remain airtight for a week. However UV glue and SU-8 are more expensive than PDMS (especially SU-8). We note, that it was much easier to make fine structures in SU-8, due to the fewer steps in the channel synthesis.

2.3 Confocal microscopy

In 1955 Minsky's frustration at being unable to produce clear images of brain neural connections with a light microscope spurred him to build the first confocal microscope [78]. Confocal microscopy has since become a popular tool especially for studying biological and colloidal systems [45, 79]. In this thesis we used laser scanning confocal microscopy (LSCM) as our main tool for observing the *fd* virus at the single particle level. Here we describe the optical set-up and explain the advantages, using the reviews [80–82].

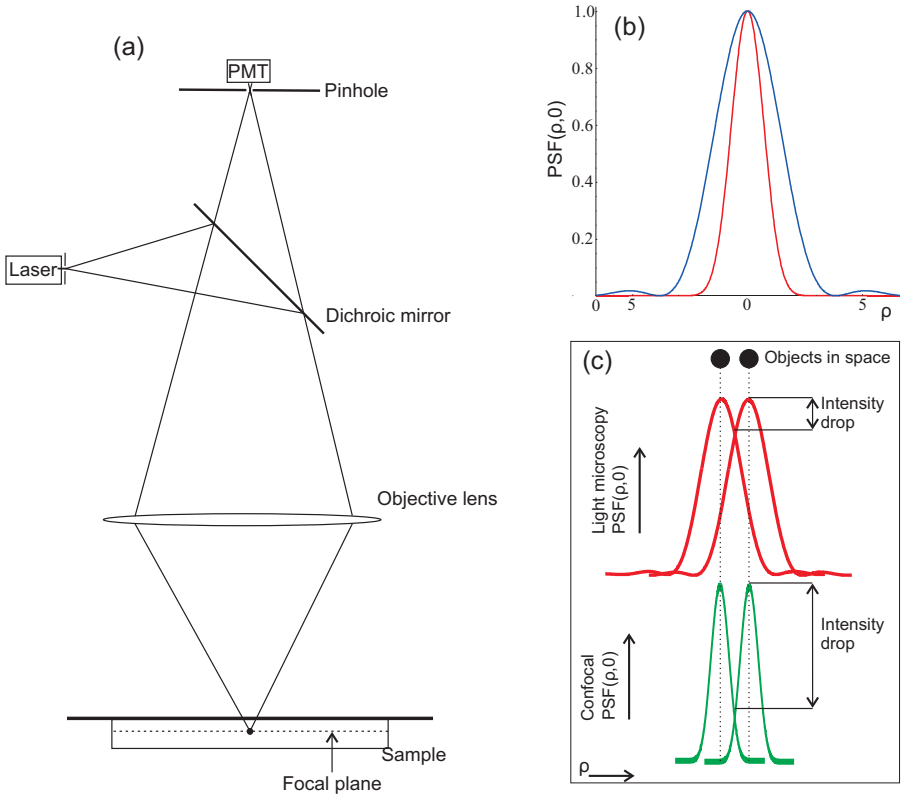

Figure 2.2: (a) Schematic diagram of the optics of a confocal microscope. (b) Comparison of the radial PSFs of light (blue) and confocal (red) microscopy. (c) Radial PSFs for two points separated by the light microscopy Rayleigh distance. The confocal has a much greater intensity drop, and thus lower Rayleigh distance, giving rise to improved resolution. PSF plots in the axial direction show similar effects.

Figure 2.3(a) shows the optical paths of a confocal microscope. Light from a laser source is focused by an objective lens onto a point in the sample via a dichroic mirror. The light from the fluorescent sample is then focused onto a detector (usually a photo-multiplier tube) using the same objective lens and dichroic mirror. A pinhole is placed before the detector. Importantly, its at the conjugate focal plane to the imaged point. The pinhole ensures that any light originating from points outside the focal point is blocked from the detector. A 2D image is then produced by scanning the sample point by point. Changing the focal depth enables 3D images to be produced. A laser is used as it enables deeper scanning due to the greater signal from more intense light, but the confocal principle works with any light source. A spinning disk confocal is analogous, but it scans many points at once by using two rotating Nipkow disks: one to generate the multiple light sources and the other to form the respective pinholes. The greater number of pinholes creates a huge increase in scanning speed.

Confocal microscopy has the advantage over standard transmission light microscopy of a significant increase in contrast and a slight improvement in resolution. The advantages are

explained by comparing the point-spread functions (PSF). The PSF can be viewed as the probability that a photon will reach a certain point in space (e.g. the detector) [80]. We define ρ and ξ, as the optical coordinates in the focal plane and optical axis respectively, which are related to the real distances r and z by:

$$\rho = r(2\pi NA/\lambda) \qquad\qquad \xi = z(2\pi NA^2/n\lambda),$$

where λ is the wavelength of the light, n the refractive index of the medium, and NA the numerical aperture of the objective. NA is defined as NA$= n\sin\alpha$, where α is the half-angle of the maximum cone of light that can enter or exit the objective. High NA objectives are desirable as more light is collected, giving a greater resolving power. The relevant PSFs are given by:

$$p(\rho,0) = \left(\frac{2J_1(\rho)}{\rho}\right)^4 \qquad \text{PSF for a point in the focal plane} \tag{2.1}$$

$$p(0,\xi) = \left(\frac{\sin(\xi/4)}{\xi/4}\right)^4 \qquad \text{PSF for a point along the optical axis} \tag{2.2}$$

Here J_1 is the first order Bessel function. Note that both equations are simply the square of the PSF of a light microscope.

The Airy disk is the radius of an illuminated point on the sample, it is quantified by where the PSF first drops to zero. In figure 2.3(b) we plot eq. (2.1) and the corresponding PSF for light microscopy. We have plotted the radial PSF, but the same trends are seen axially. Comparison of the PSFs reveals that the width of the PSF is less for a confocal microscope. Furthermore, the outer maximum is significantly lower for a confocal microscope. Thus confocal microscopy gives a greater contrast over light microscopy as each point is 'tighter' and contains more light.

The resolution is determined by the ability to distinguish between two points. This is quantified by the Rayleigh criterion, which states that two points can be resolved if the intensity drop between the maxima is 26%. In figure 2.3(c) we plot the light and confocal microscopy PSF intensity profiles, for two objects separated by the distance corresponding to the light microscopy Rayleigh criterion. The intensity drop is much greater for the confocal microscope, and thus the confocal Rayleigh distance is less and the resolution of confocal microscopy is greater. The radial resolution is 3.82 (in ρ) for light and 2.76 for confocal microscopy, and the axial resolution is 13.12 (in ξ) for light and 9.53 for confocal microscopy. Finally, we stress that although there is

an increase in resolution the main advantage of the confocal microscope is the greater contrast.

We use the following confocal set-ups in this thesis, with high NA objectives and a 488nm laser source: (1) Zeiss LSM 5 Exciter, (2) Leica inverted microscope with a Yokogawa CSU22 spinning disk unit, and (3) Nikon C1 confocal microscope.

2.4 Birefringence and polarized light microscopy

The birefringence of a virus sample was ingeniously shown by Bawden in 1936, when a a swimming fish was used to orient the tobacco mosaic virus [3]. The birefringence of the nematic phase comes from the ordering of the particles, and causes light to be transmitted when samples are placed between crossed polarisers. In contrast, the absence of ordering in the isotropic phase causes it to appear dark between crossed polarizers, but flow can align the particles, making samples temporarily birefringent [83].

A polarization microscope is simply a light microscope equipped with two crossed polarizers, one placed before the light source, the other placed before the detector. It is used in this thesis as a quick way to determine the phase of a sample and a guide to the concentration of nematic samples. We note it was particularly useful for preparing samples at or near the isotropic-nematic biphasic region.

2.5 Particle detection

In our work it is crucial to identify the single rods and accurately determine their position and orientation. This enables us to obtain the vector fields of the director and measure the order parameter. Due to the rods small size and aspect ratio of $\sim$133, a pixel resolution of at least 200 nm was required to ensure the rods were represented by a sufficient number of pixels for the anisotropy to be observed. In the majority of images a pixel size of 130 nm was used. A range of scanning speeds were used from 0.03 seconds to 50 seconds, for an image of dimensions 512 $\times$ 512 pixels. For the greater scanning speeds the images are not snapshots and the rods appear longer than they actually are due to the diffusion of the rods during image capture.

We use IDL (Interactive Data Language) to determine the rods centre of mass and ori-

entation. We based our programs on the particle tracking routines by Crocker and Grier [84]. Initially, a bandpass was applied to smooth the image and then the rods were located by fitting a 2D Gaussian to the raw data around the centre of the particle. From these fits the orientation of the rod was obtained by finding the two perpendicular Gaussians with the greatest aspect ratio. The method is illustrated in figure 2.5 and the resultant coordinates and rod angle are plotted over the original image.

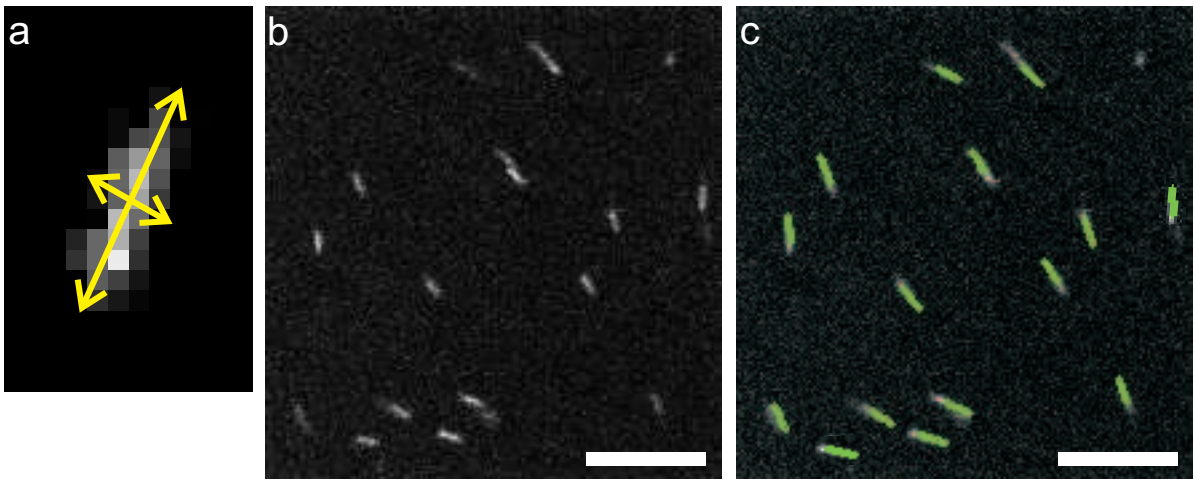

Figure 2.3: (a) Two-dimensional Gaussian fits along the long and short axis of the rod. Pixel size = 0.130μm. (b) Raw microscope image. (c) Raw microscope image with overlaid detected rods. Scale bar = 5 μm.

Appendix: Virus synthesis

The synthesis involved growing a bacterial culture which was then infected with the virus.

During the synthesis it was vital that no contamination occurred. The lab was kept as clean as possible and when handling sterilized equipment gloves were worn and care was taken not to breathe heavily. All the tubes and flasks, which were sterilized, were firstly covered with aluminum foil fixed to the tube/flask with sterilization sensitive adhesive tape and then autoclaved. In the autoclave program the temperature rose to 120°C and then took about two hours to cool down to 80°C, which was when the door could be opened and the tube/flask removed.

Preparation

MEDIUM: To make the medium the following reagents and quantities were used:

	Conc.	1.5l	3l	6l
Tryptone (Pancreatic digest of caesin)	10g/l	15g	30g	60g
Yeast extract	5g/l	7.5g	15g	30g
NaCl	10g/l	15g	30g	60g

The pH would be adjusted to 7.00 with 2M NaOH.

AGAR PLATES: To make the hard or soft agar plates, 15 g/L or 7 g/L of agar were added to the medium. This mixture was autoclaved and then poured into a sterile petri dish. The plates would be left to cool down overnight and then be checked for bacterial growth; if bacterial growth occurred, the plate would be binned. The plates were stored in a refrigerator to prevent bacterial growth and upside down to prevent condensation dripping on the agar.

XL1-blue BACTERIAL CULTURE PLATE and SOLUTION: Using an infection eye the bacterial solution was carefully streaked onto an agar plate; three streaks on each plate. The plates were incubated at 37^{o}C for 1-2 hours. If separate colonies were formed the plate was a success.

To make the solution one bacterial colony was added to a sterile tube containing 3 ml of medium. This was done twice and the two tubes were incubated for 12-14 hours at 37^{o}C. After

this time the tubes became highly turbid: the clear brown medium solution became a cloudy brown solution.

BASIC VIRUS SOLUTION: Using an existing virus solution ten dilutions were carried out, with a factor of 10 per dilution step, by taking 0.1 ml on 1 ml each time. Soft agar was prepared and kept liquid using a hot plate and 0.3 ml of the bacterial culture solution and 0.1ml of the virus dispersion was added to the agar. The solution was mixed carefully so that air bubbles did not form and then poured into a petri dish. This was repeated for each of the 10 dilutions. Once the plates were set they were incubated for 12-16 hours at 37^oC. The plates with clear spots in the background of bacterial growth were kept. To make the virus solution a plaque was stabbed with a sterilized pipette and this plaque was then released into 50 ml of medium, which was incubated overnight for 16-18 hours at 37^oC. If necessary, bacteria could be removed from the virus solution by centrifugation at 5000 rpm for roughly 30 minutes.

Synthesis

Day 1: Eight 750 ml solutions of medium were prepared in 2 litre Erlenmeyer flasks. The flasks were sterilized for 2 hours. After sterilization each flask was infected with 0.5 ml of the bacterial suspension and then incubated for 3 hours. Then each of the Erlenmeyer flasks were infected with 0.5 ml of the basic virus solution and incubated for about 14-16 hours. Note that in this step is was important to work sterile.

Day 2: Firstly, the bacteria was removed by centrifugation for 30-60 minutes at 5000 rpm. Then 120 g NaCl and 120 g polyethyleneglycol (MW 8000) were added to the combined 6 litres of solution. The clear solution became turbid due to aggregation of the *fd* viruses from depletion by the PEG; this was a sign of successful virus production. The virus was then separated from the NaCl and polyethyleneglycol by centrifugation for 30 minutes at 5000 rpm. We would then re-disperse the virus in as little deionized water as possible and store the virus in the refrigerator to prevent the growth of bacteria.

Final Purification: The viruses produced from several one day cycles were centrifuged for 30-60 minutes at 10000 rpm. The sediment was waste. The virus solution would then be centrifuged for 8 to 16 hours to separate it from the remainder of the medium and polymer. The pellet produced from the first cycle through the previous steps would normally have a black dirty spot

in the middle. We would re-disperse the pellet and then repeat the cycle untill a clean pellet was produced. The *fd* would be re-dispersed and stored in; 85%; 100 mM NaCl and 20 mM Tris at pH=8.2, and 15% Ethanol. The ethanol prevented the growth of bacteria.

Acknowledgments

All virus suspensions were produced in Jan Dhont's lab, at the Forschungszentrum Jülich. In addition to the samples I synthesised, samples synthesised by M.P.Lettinga and M. Stiakakis were also used. Both are thanked. Julia Schollick is thanked for reading the manuscript.

Chapter 3

Confinement induced splay to bend transition of colloidal rods

Abstract

We study the nematic phase of rodlike *fd* and Y21M virus particles confined to channels with wedge structured walls. Using laser scanning confocal microscopy we observe a splay-to-bend transition at the single particle level as a function of the wedge opening angle. Lattice Boltzmann simulations help reveal the underlying origin of the transition and its dependence on nematic elasticity and wedge geometry. Our combined work provides a simple method to obtain the splay-to-bend elasticity ratios of the virus and offers a way to control the position of defects through the confining boundary conditions.

3.1 Introduction

Packing and confinement problems emerge in fields ranging from biology to engineering. In biological systems the organization of the cell is determined, among other things, by the packing of fibril-like particles (actin filaments, DNA) [72, 85]. An example of the subtlety of packing phenomena is the plethora of liquid crystalline phases that can be found in arrangements of anisotropic particles by increasing concentration [1, 18]. Confinement of liquid crystals adds to the complexity, since the interactions of the particles with the walls may lead to structures that compete with those formed in the bulk [86, 87]. Many of the next generation liquid crystal display devices exploit this interplay by using structured or patterned surfaces as an essential element of their design [88, 89]. Very recently, the ordering at sawtoothed structures has been studied theoretically within a Landau-De Gennes framework [90, 91], with a focus on the wetting behaviour.

In this chapter, in a combined experimental and theoretical effort, we show the rich phenomenology that emerges when confining a nematic liquid crystal to a microfluidic channel with a wedge structured wall. We seek to disentangle how the wedge geometry and elasticity of the *fd* -virus' nematic phase determine the adopted deformation in the wedge. We introduce a new method for estimating elastic constants suitable to colloidal and biological systems, as an alternative to previous methods using magnetic fields [55] or light scattering [92]. Specifically, we determine the transition from a splay to a bend director field, with increasing wedge angle.

The chapter is organized as follows; we begin by describing the interplay between the splay and bend elasticities when confining the nematic phase of a liquid crystal to an isolated wedge (section 3.2). We then introduce the experimental set-up (section 3.3) and present the results (section 3.4). Experimentally, the geometry is more complex than that of an isolated wedge and in the subsequent section we present the numerical part of the study which takes into account the channel geometry (section 3.5). Finally we compare experimental and numerical results (section 3.6) before discussing the implications of the work and concluding (section 3.7).

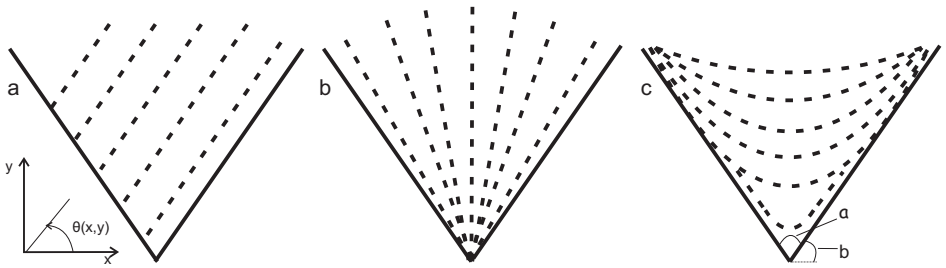

Figure 3.1: Possible director fields of a nematic confined to a wedge. (a) An elastically undistorted director field with an anchoring penalty at one wall. (b) A pure splay deformation. (c) A deformation with both bend and splay contributions, which we refer to as the bend* configuration.

3.2 Elastic energy of an isolated wedge

A nematic liquid crystal phase confined to a wedge has to elastically distort the director field, $\mathbf{n}$, or pay an anchoring penalty, see figure 3.1. The liquid crystal will naturally adopt the director field which is lowest in energy. Experimentally we observe strong anchoring, and for this case with increasing wedge opening angle there will be a transition from a splay (figure 3.1(b)) to a bend (figure 3.1(c)). Strictly speaking the director field in figure 3.1(c) has bend and splay contributions. To highlight this we will refer to it as bend*. We evaluate the splay and bend* energies for a wedge of opening angle, a, and find the splay-bend* transition angle using the Frank-Oseen energy (eq. (1.3)):

$$F_e = \int\int \left(\frac{K_1}{2}(\nabla \cdot \mathbf{n})^2 + \frac{K_3}{2}(\nabla \times \mathbf{n})^2 \right) dxdy. \tag{3.1}$$

A 2D evaluation is sufficient as the director has no component in the z-direction for both deformations. We start by evaluating eq. (3.1) using a general expression for the director field which applies to both splay and bend*, $\mathbf{n} = (\cos\theta(x,y), \sin\theta(x,y), 0)$, with θ the angle between $\mathbf{n}$ and the x-axis:

$$\begin{aligned} F_e &= \frac{1}{2}K_1 \int\int (\nabla \cdot \mathbf{n})^2 d\mathbf{r} + \frac{1}{2}K_3 \int\int (\nabla \times \mathbf{n})^2 d\mathbf{r} \\ &= \frac{1}{2}K_1 \int\int \left(-\sin\theta \frac{\partial\theta}{\partial x} + \cos\theta \frac{\partial\theta}{\partial y} \right)^2 d\mathbf{r} + \frac{1}{2}K_3 \int\int \left(\cos\theta \frac{\partial\theta}{\partial x} + \sin\theta \frac{\partial\theta}{\partial y} \right)^2 d\mathbf{r} \\ &= \frac{K}{2} \int\int (\nabla\theta)^2 d\mathbf{r}, \end{aligned} \tag{3.2}$$

where in the final step we have used the one constant approximation $K = K_1 = K_3$. Minimising this functional using calculus of variations yields the Laplace equation:

$$\nabla^2\theta = 0. \tag{3.3}$$

By solving this equation an expression for θ, and then $\mathbf{n}$ is found. A common technique for solving a 2D Laplace equation is by conformal mapping [93]. This technique has been frequently used for evaluating nematic director fields in confined geometries, including a wedge. For examples see references [35, 94, 95]. Here, we simply state the result of Mottram [95], which is identical to Barbero's result [35]:

$$\theta = \frac{n\pi - 2b}{\pi - 2b}\tan^{-1}\left(\frac{y\cos(b) - x\sin(b)}{x\cos(b) + y\sin(b)}\right) + b. \tag{3.4}$$

Where $n = 0$ or 1 for the bend* or splay deformations respectively, a is the opening angle of the wedge, and $b = (a - \pi)/2$ as shown in figure 3.1. The one constant approximation has been used to derive the vector field in eq. (3.4) and we will now assume that the director field is valid for all K_1/K_3 ratios. Using eq. (3.1) and eq. (3.4) we evaluate the elastic energies of the splay and bend* deformations.

$$\begin{aligned} \textit{Splay} \qquad F_s &= \frac{1}{2}K_1\int(\nabla\cdot\mathbf{n})^2 dxdy \\ &= \frac{1}{2}K_1\int_{\frac{\pi}{2}-\frac{a}{2}}^{\frac{\pi}{2}+\frac{a}{2}}\int_{r_{min}}^{r_{max}}\left(\frac{1}{r}\right)^2 r dr d\theta \\ &= \frac{1}{2}aK_1\ln\left(\frac{r_{max}}{r_{min}}\right). \end{aligned} \tag{3.5}$$

r_{min} and r_{max} are introduced as the lower and upper cut-off radii of the wedge to avoid the divergence of the integral.

$$\begin{aligned} \textit{Bend*} \qquad f_b^1 &= (\nabla\cdot\mathbf{n})^2 \\ &= \frac{(a-\pi)^2\sin\left(\frac{a}{2} + \theta + \left(\frac{\pi}{a} - 1\right)\tan^{-1}\left(\frac{-r\cos(\frac{a}{2})}{r\sin(\frac{a}{2})}\right)\right)}{a^2r^2}, \\ f_b^2 &= (\nabla\times\mathbf{n})^2 \\ &= \frac{(a-\pi)^2\cos\left(\frac{a}{2} + \theta + \left(\frac{\pi}{a} - 1\right)\tan^{-1}\left(\frac{-r\cos(\frac{a}{2})}{r\sin(\frac{a}{2})}\right)\right)}{a^2r^2}. \end{aligned} \tag{3.6}$$

Which leads leads to:
$$F_b = \frac{K_1}{2}\int f_b^1 d\mathbf{r} + \frac{K_3}{2}\int f_b^2 d\mathbf{r}$$
$$= (K_1 + K_3)\frac{(a-\pi)^2}{4a}\ln\frac{r_{max}}{r_{max}}. \tag{3.7}$$

Note that the integrals for the K_1 and K_3 contributions to the bend* state are equal, eq. (3.6). By equating the energies F_b and F_s we extract the transition angle between the two deformations as a function of the elastic constant ratio, K_1/K_3:

$$\frac{K_1}{K_3} = \frac{(a-\pi)^2}{a^2 + 2a\pi - \pi^2}. \tag{3.8}$$

We highlight that the transition is independent of the wedge height and length. Equation (3.8) has physical positive solutions for a $> 74.5°$. In figure 3.2 we plot K_3/K_1, versus wedge opening angle, a. As the elasticity ratio K_3/K_1 increases, and the energy cost of the bend becomes increasingly greater than the splay, we observe the splay-bend* transition shift to higher wedge opening angles. $K_3 = K_1$ occurs for $a = 90°$ and this is expected due to the symmetry of the problem: when the bend and splay have equal energy costs, the transition occurs midway between 180° (a flat wall) and 0°.

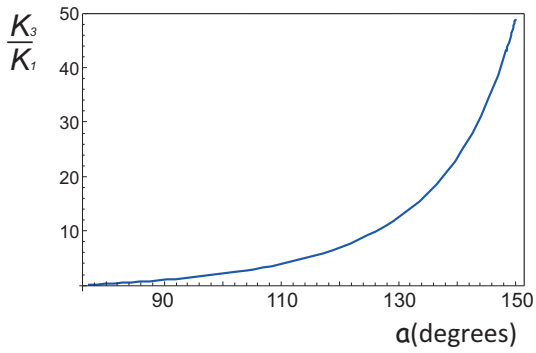

Figure 3.2: Plot of elasticity ratio, K_3/K_1, versus wedge opening angle, a (eq. (3.8))

In our experiments, we have a different geometry where the wedge is connected to a channel. It turns out that the energy minimum of a wedge connected to a channel differs to that of an isolated wedge. This will be discussed later, with the calculation of an isolated wedge providing a useful starting point as to what to expect experimentally.

In the above method we have calculated the lowest energy director field $\mathbf{n}$ for a wedge, and then used the expression for $\mathbf{n}$ to calculate the energies of the splay and bend* deformations. An alternative method would have been to simply 'guess' expressions for the splay and bend*

director fields in figure 3.1. This method yields a very similar result and is performed in the appendix at the end of the chapter.

3.3 Experimental set-up and image analysis

We used the *fd* and Y21M viruses, which are excellent model liquid crystal systems, for both static and dynamic behaviour, as described in chapter 1. The two viruses have a contour length = 0.88 μm, and a diameter = 6.6 nm. The only physical difference between the viruses is a single amino acid in the major coat protein, which causes a difference in their flexibility, with Y21M being rigid and *fd* semi-flexible [62]. We used the *fd* and Y21M viruses at nematic concentrations of 24 mg/ml and 20 mg/ml respectively, prepared as described in chapter 2. The two concentrations were 1 mg/ml above the isotropic-nematic biphasic region. Imaging of the labeled particles was carried out with two setups: (1) a laser scanning confocal microscope (LSCM); Zeiss LSM 5 Exciter, 63x 1.4 NA oil-immersion objective, and (2) a video fluorescence microscope; Zeiss Axiovert, 100x PlanFluor NA 1.35 oil objective, equipped with a mercury lamp and a high sensitivity electron-multiplying-CCD camera (Hamamatsu C9100).

Microfluidic channels were constructed out of UV glue (NOA 81) with a side wall structured with wedges with a range of opening angles, see figure 3.3. The radius of curvature of the tip of the wedge is smaller than 2.5 μm and the walls are smooth on the colloidal lengthscale ($\sim$1 μm). The measurement range was 20-110° in steps of 5-10°. The height of the channels was 10 μm, which is smaller than the cholesteric pitch for both viruses [31], giving 'pseudo 2D' confinement. This was confirmed by three dimensional LSCM scans. Due to the thin samples polarization microscopy was not possible. The height of the channels is characterized by h_c and h_w (figure 3.3). We constructed channels with dimensions: $h_c = 500$ μm and $h_w = 75$, 750 and 1125 μm. The larger wedges (h_w= 750 and 1125 μm) enabled detailed images of the splay and bend* deformations to be obtained, and the small wedges ($h_w = 75$) enabled the director field for the entire wedge to be visualized in one microscopy image.

The structured microfluidic channels were filled by capillary action. Directly before filling the channels were plasma cleaned, which changes the hydrophilicity of the channels [96] and offers a way to control the speed of filling. This enabled us to set the initial conditions of the experiment due to the coupling between the nematic director and flow: low filling speeds created

an initially disordered configuration due to the tumbling motion of the rods, while high filling speeds resulted in the rods immediately adopting metastable aligned deformations, which only slowly found the equilibrium state [97]. We filled the channels slowly and from a disordered configuration the equilibrium was reached within a couple of hours.

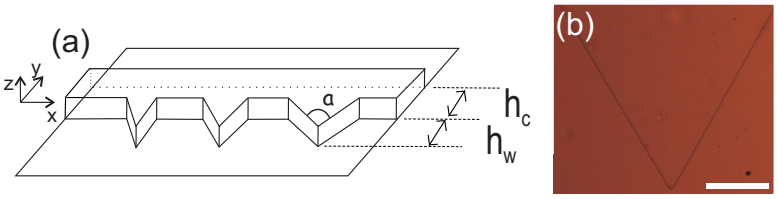

Figure 3.3: (a) Geometry of the microfluidic channel. (b) Light microscopy image of the tip of a wedge. Scale bar = 40 μm.

To quantify the LSCM images we first identified each rod's position and orientation, as explained in chapter 2. Director fields were then obtained by dividing a series of LSCM images into squares of a suitable area and then averaging the orientation of the rods in each square. The average number of rods per square would always be greater than 50 rods and the standard deviation in the orientation would always be less than 10%. The lapse time between images was always longer than the typical self-diffusion time, ensuring the images were statistically independent.

3.4 Results

Figures 3.4(a) and (b) display LSCM images of the fluorescently labeled *fd* virus in a splay and a bend* deformation, respectively. The nematic deformations are clearly seen from movies in which the rods move along the director lines. Plots of the particle trajectories obtained from fluorescent microscopy, also show that the rods diffuse more strongly along the director lines, as shown in figure 3.4(c) and (d). By tracking the particles close to the walls we verified that no rods were sticking to the walls. In addition, for splay deformations, we calculated the order parameter q in piece-wise segments across the wedge, see the inset of figure 3.4(a). We found that the order parameter would be in the range 0.7-0.9, and constant across the wedge, which is an indication of strong planar anchoring. For bend* deformations the director lines are curved, which makes it more difficult to select regions in which to calculate the order parameter q, but we have no indication that q is less than in the splay configurations.

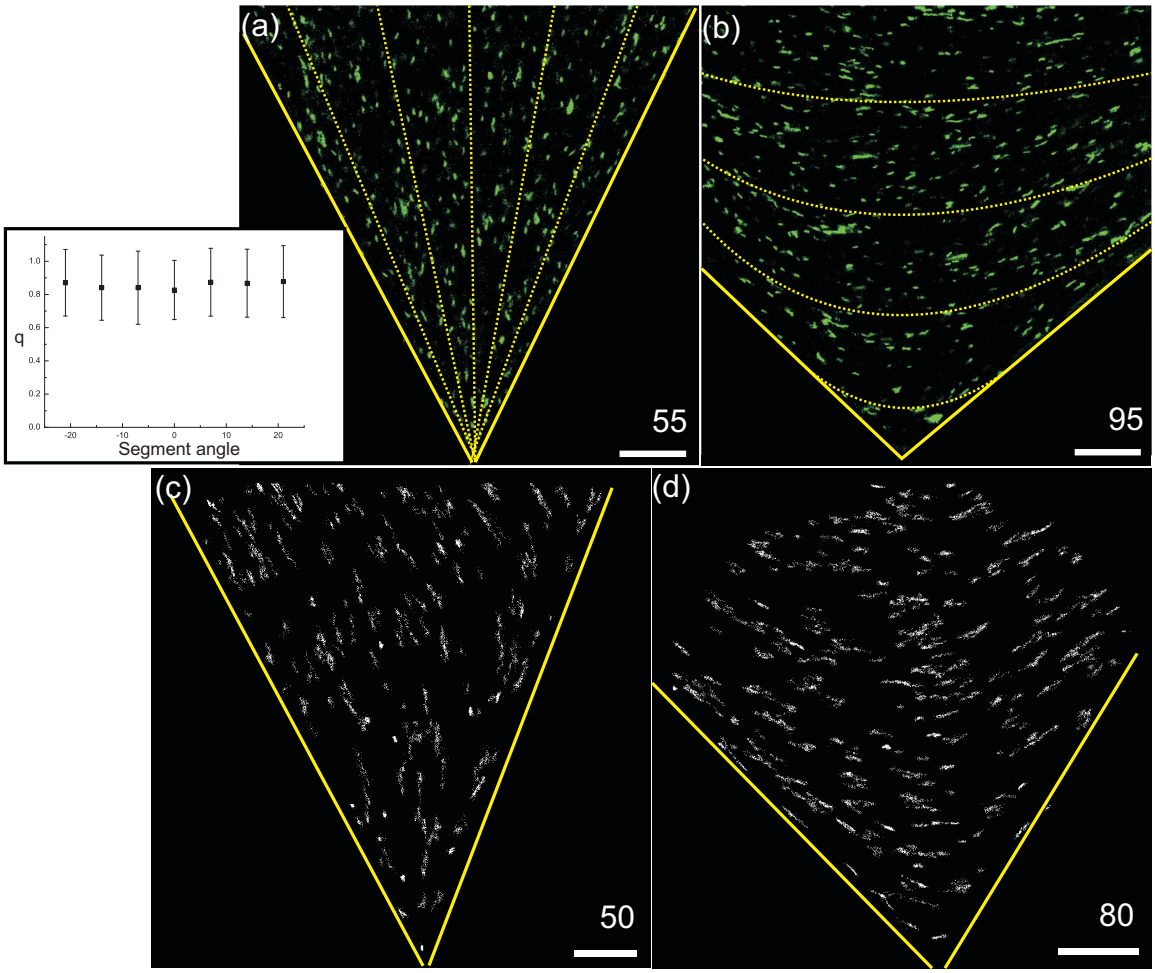

Figure 3.4: (a) and (b): LSCM microscopy pictures of the *fd*'s nematic phase in a splay (a) and a bend* (b) deformation, obtained by overlaying 7 LSCM images. Only the fluorescent *fd* virus particles are visible. The overlaid dashed lines are a guide to the eye of the director. Inset in (a): Plot of order parameter versus segment angle for the movie corresponding to the image in (a). (c) and (d): Trajectories of fluorescently labeled *fd* virus in a splay (c) and a bend* (d) deformation. Scale bar = 10 μm, and wedge height $h_w = 1125$ μm, in all four images.

We observe splay deformations, accompanied by a defect in the bulk of the wedge, below 70°, and bend* deformations above 80°, for *fd*. Figure 3.5(a) shows *fd*'s director fields for $h_w = 1125$ μm. Similarly, for Y21M we observe a splay-bend* transition around 90°. At 90° we observe bend* or splay with a defect very close to the tip in roughly equal frequencies, indicating that 90° is at the cusp of the transition. Figure 3.6 shows LSCM images alongside experimental director fields for Y21M for $h_w = 70$ μm. The transitions for both viruses were observed for all h_w values.

Figure 3.7(a) shows a LSCM image of an $s = -1/2$ defect and in figure 3.8(a) we plot the relative position of the defect, defined as $\tilde{h} = z_d/h_w$, with z_d the height of the defect with respect to the tip, as a function of the opening angle a. It is not possible to map the defect for the

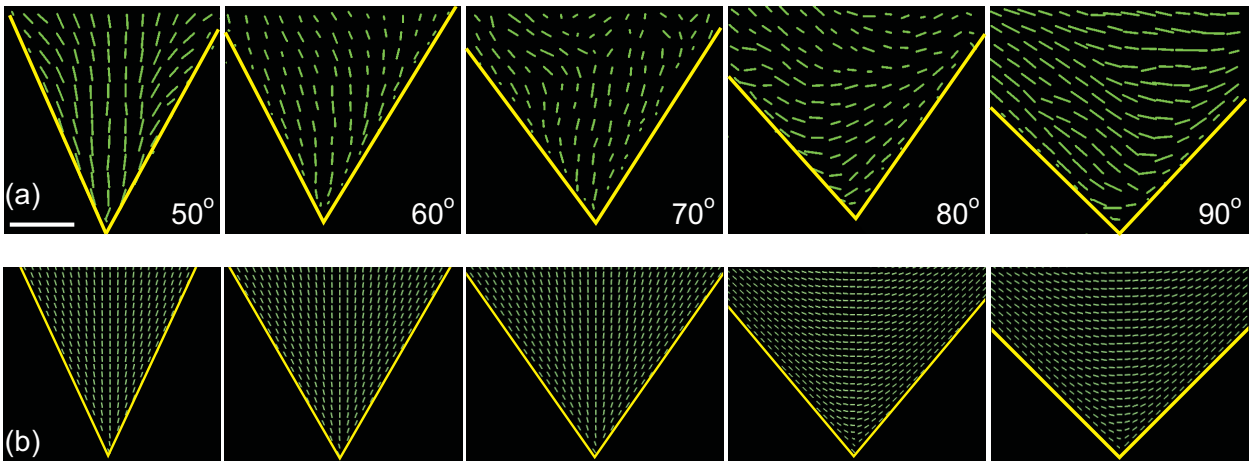

Figure 3.5: Director field in the wedge for varying wedge angle $\theta = 50° - 90°$: (a) Director fields from experiments with the *fd* virus, calculated by averaging over 10 images. $h_w = 1125$ μm and $h_c = 500$ μm. Scale bar = 50 μm. (b) Director field from lattice Boltzmann simulations. In both cases the transition from a splay to a bend* configuration occurs between $70 - 80°$.

larger channels with $h_w = 750$ and 1125 μm, as rather than a defect, multidomains (Schlieren texture) are observed near the top of the wedge due to the lack of confinement. However, we do observe the defect for angles close to the splay-bend* transition angle where the defect is close to the tip of the wedge, and the confining side walls.

Comparing the transition angles for *fd* and Y21M to the indicative calculation presented in section 3.2 we see that K_1/K_3 is greater for *fd* than Y21M, which is what we expect: with increasing rod stiffness the energy cost of bending the director field increases, whereas we expect rod stiffness to have a minimal effect on the cost of the splay due to the straight director lines. However, figure 3.2 suggests that $K_1 > K_3$ for *fd*, and this would be slightly surprising as all previous measurements have found $K_1 \leq K_3$, with $K_1 \approx K_3$ for semi-flexible rod-like molecules [1, 62, 92]. The reason for this seemingly surprising result is that the calculations in section 3.2 have been done for a large wedge without taking into account the channel. The major effect of the channel is clearly illustrated by the presence of the $s = -1/2$ defect. To describe the geometry correctly lattice Boltzmann simulations were performed, which we will now discuss in section 3.5.

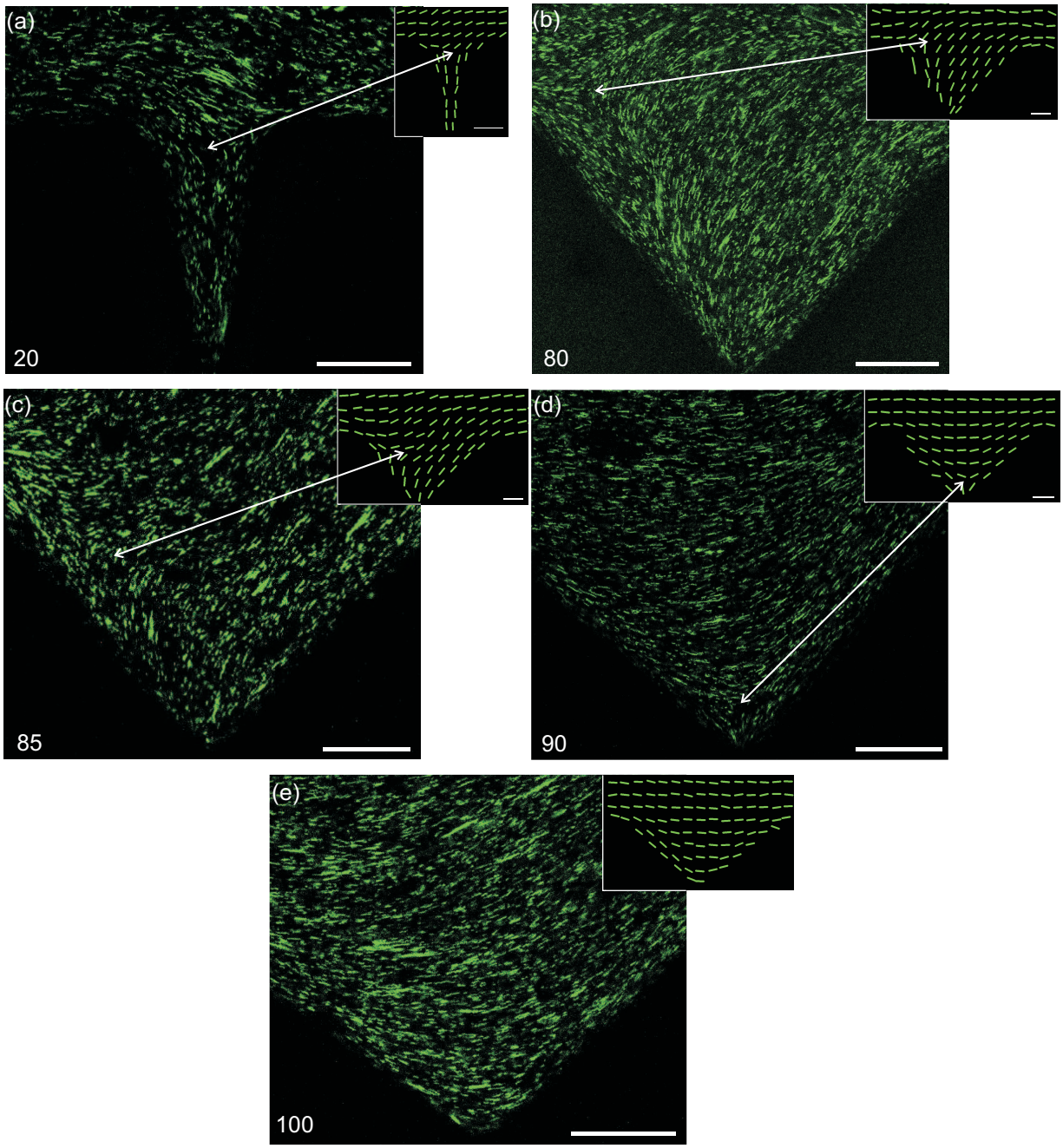

Figure 3.6: (a)-(e) LSCM microscopy pictures of the Y21M virus in wedge channels of geometry; $h_w = 70$ μm and $h_c = 500$ μm. Each image is obtained by overlaying 7 LSCM images and only the fluorescent Y21M particles are visible. The inset shows the corresponding director fields, calculated by averaging over 12 images. The arrows highlight the $s = -1/2$ defect. Scale bar = 20 μm in both the LSCM images and director fields.

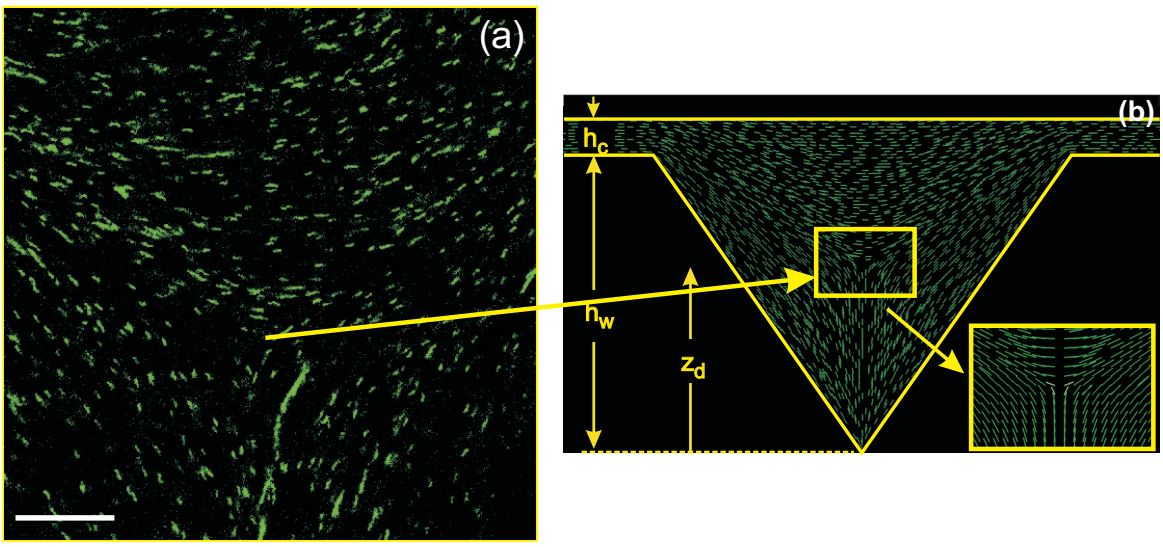

Figure 3.7: (a) Microscopy picture of a defect of strength $s = -1/2$, where the splay configuration meets the bend configuration, obtained by overlaying 5 LSCM images. Only the fluorescent *fd* virus particles are visible. Scale bar = 10 μm. (b) Director field from a simulation for a wedge angle of 70° showing the corresponding defect. The inset shows a zoom of the defect.

3.5 Lattice Boltzmann simulations

The simulations were run by Ioannis Zacharoudiou supervised by Julia M. Yeomans, Ard Louis and Dirk Aarts at the Rudolf Peierls Centre for Theoretical Physics, University of Oxford.

To elucidate our experimental observations numerical simulations were performed taking the actual channel geometry into account [1]. The simulations were based on the Beris-Edwards [99] model for liquid crystal hydrodynamics where the continuum equations of motion were written in terms of a tensor order parameter $Q_{\alpha\beta} = q(3n_\alpha n_\beta - \delta_{\alpha\beta})/2$. Its largest eigenvalue gives the nematic degree of order q and the corresponding eigenvector the director field $\mathbf{n}$. The equilibrium properties of the liquid crystal were described by the Landau-de Gennes free energy [1,100]. This comprises a bulk term f_b and an elastic term f_{el}:

$$f_b = A_0\left[\frac{1}{2}(1-\frac{\gamma}{3})Q_{\alpha\beta}^2 - \frac{\gamma}{3}Q_{\alpha\beta}Q_{\beta\gamma}Q_{\gamma\alpha} + \frac{\gamma}{4}(Q_{\alpha\beta}^2)^2\right], \tag{3.9}$$

[1] Here we sketch out how the simulations were run. For the full details necessary to re-run the simulations the reader is referred to [98].

$$f_{el} = \frac{L_1}{2}(\partial_\alpha Q_{\beta\gamma})^2 + \frac{L_2}{2}(\partial_\alpha Q_{\alpha\gamma})(\partial_\beta Q_{\beta\gamma}) + \frac{L_3}{2}Q_{\alpha\beta}(\partial_\alpha Q_{\gamma\epsilon})(\partial_\beta Q_{\gamma\epsilon}). \quad (3.10)$$

In eq. (3.9) γ is a measure of the rod concentration, which sets the location of the first order isotropic-nematic transition to $\gamma = 2.7$ and the nematic degree of order, and A_0 is a constant. In eq. (3.10) the prefactors L_n with $n = 1, 2$ or 3 are linear combinations of the Frank elastic constants, K_n [101]:

$$\begin{aligned} K_1 &= \frac{9q^2}{4}(2L_1 + L_2 - qL_3) \,, \\ K_2 &= \frac{9q^2}{4}(2L_1 - qL_3) \,, \\ K_3 &= \frac{9q^2}{4}(2L_1 + L_2 + 2qL_3) \,. \end{aligned} \quad (3.11)$$

The anchoring of the director on the walls was modeled by using a Rapini-Papoular-like surface free energy density, $f_s = W^{uni}(Q_{\alpha\beta} - Q^0_{\alpha\beta})^2$, where W^{uni} denotes the uniform anchoring strength and $Q^0_{\alpha\beta} = q(3n^0_\alpha n^0_\beta - \delta_{\alpha\beta})/2$ corresponds to the preferred director orientation $\mathbf{n^0}$ imposed by the walls. The equations of motion were solved using a hybrid lattice Boltzmann scheme [38]. Although only results in equilibrium are reported, solving the full hydrodynamic equations was found to be an efficient way of accessing the free energy minimum.

Apart from reproducing the geometry of the microchannel, there are several conditions that needed to be fulfilled in order to match the experimental conditions. First, the nematic degree of order q was kept around 0.8 to match the ordering in the experiments. Second, the starting configuration was matched by choosing an isotropic configuration in the wedge ($q = 0$), and a nematic state with a horizontal director $\mathbf{n}$ in the channel above the wedge. Third, the experimental situation was approached by using $\xi_N/h_w \sim 1/100$. The nematic correlation length ξ_N sets the lengthscale for the variations in the nematic degree of order q. Experimentally, ξ_N is of order of the rod dimensions, i.e. $\sim \mu$m. Strong planar surface anchoring was used, that lead to perfect alignment of the rods with the surfaces, as in the experiments. Finally, a value for K_3/K_1 was inputted.

Numerically a splay-bend* transition is observed, with the angle of the transition being

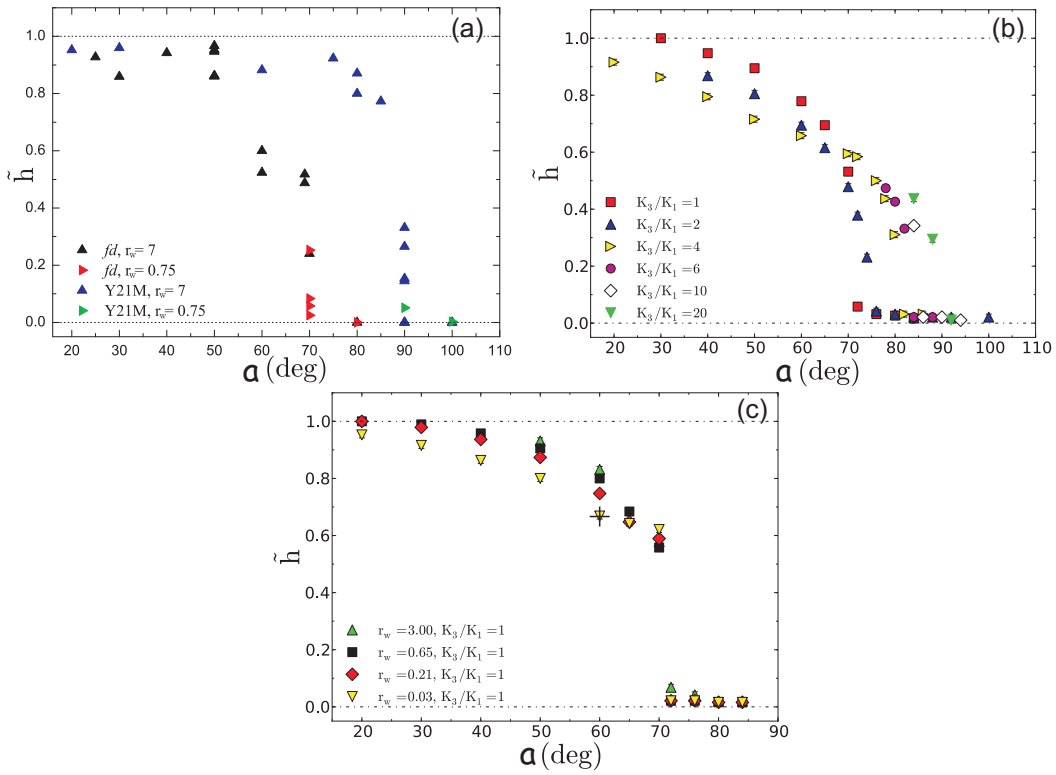

Figure 3.8: The relative position of the defect within the wedge $\tilde{h} = z_d/h_w$. (a) Experimental values for both *fd* and Y21M. (b) and (c): Lattice Boltzmann simulations plotted as a function of the wedge angle a, for varying: (b) elasticity ratio K_3/K_1, and (c) channel geometries $r_w = h_c/h_w$. The cross in (c) denotes the position $\tilde{h} = 0.667$ at $a = 60°$, which is the position of the orthocentre of an equilateral triangle and the expected position of the defect in the case of $r_w \to 0$. We highlight that the *fd* and Y21M defect transitions best match the simulations with elasticity ratios; $K_3/K_1 = 1$ and $K_3/K_1 = 10 - 20$ respectively.

determined by K_3/K_1. Figure 3.5(b) shows numerical director fields for $K_1 = K_3$. The $s = -1/2$ defect for splay deformations is also observed numerically, as shown in figure 3.7(b). In figures 3.8(b) and (c) we plot the relative defect height for various K_3/K_1 ratios, and channel geometries $r_w = h_c/h_w$.

3.6 Discussion

We have clearly identified splay and bend* deformations for *fd* and Y21M. Figure 3.5 compares the director fields obtained for *fd* in experiment, with the director fields of simulations, run with $K_1 = K_3$, showing very good agreement. In particular, both sets of data display a splay-to-bend* transition at opening angles ∼70°. This gives us the confidence to use the simulations to help demonstrate the mechanism behind the transition, and measure the K_3/K_1 elasticity ratio.

In the case of splay deformations, the inevitable frustration of the director field due to the horizontal configuration in the main channel leads to a $s = -1/2$ defect in the wedge, see figure 3.7. Figure 3.8 presents the relative position of the defect for; (a) experiments, (b) simulations with different K_3/K_1 ratios, and (c) simulations with different values of the ratio of channel height to wedge length, $r_w = h_c/h_w$. For small wedge angles the defect lies close to the top of the wedge, and with increasing wedge angle the splay deformation becomes less favourable, and the defect is pushed into the wedge by the dominance of the nematic order in the microchannel. Experimentally an abrupt transition is observed just above 70° for *fd* and at 90° for Y21M, for all wedge heights h_w. This corresponds to the splay to bend* transition: for higher wedge angles the defect is no longer present and a bend* deformation is adopted. In figure 3.8(b) as we numerically increase K_3/K_1 the splay-bend* transition is shifted to higher opening angles. In figure 3.8(c) we numerically vary the channel dimensions, r_w, for $K_3 = K_1$, and observe very similar curves, which converge with increasing wedge angle. Thus our experimental and numerical results show the transition is sharp and does not depend on the height of the wedge or channel, r_w. Furthermore, our results illustrate that the position of the defect can be controlled through the wedge angle and the elasticity of the system.

The transition occurs when the energy of the splay configuration plus the energy of the defect becomes equal to the energy of the bend* configuration. The main channel maintains its horizontal director field as we encounter the splay to bend* transition, thus the channel height h_c does not have a significant effect. It is at first sight surprising that the location of the transition is predominantly determined by the wedge angle a and is independent of the wedge height h_w. However, this can be explained by noting that the energy of the defect (per unit length and using the one elastic constant approximation) is given by $E_d = K\left\{\epsilon_d + \frac{\pi}{4}\ln\left(\frac{R}{r_c}\right)\right\}$ [1], where the first term is the contribution from the core of the defect and R is the distance to the walls of the wedge. A lower cut-off r_c is introduced, which is related to the size of the defect core and can be approximated by the nematic correlation length ξ_N. The second term in the defect energy is proportional to the elastic constant K and depends logarithmically on the system size. The same is true for the energies of the splay and bend* configurations [95]. Hence, given that we may ignore the first term in the defect energy, the splay-bend* transition will be independent of the size of the wedge. The energetic contribution of the defect core ϵ_d can be quantified by the ratio of the nematic correlation length to the height of the wedge ξ_N/h_w. We expect that experimentally ξ_N is of order of the dimensions of the rods. Hence $\xi_N/h_w \ll 1$ and ϵ_d is indeed

negligible. (We find numerically that the transition can be shifted to higher opening angles due to the effect of the defect core energy, but this effect only becomes non-negligible for $h_w \sim 10$ rod lengths.)

A different splay-bend* transition is observed for the *fd* and Y21M viruses. A bend* deformation has curved director lines and with increasing rod flexibility the rods are able to bend along the director lines, making it 'easier' to adopt the deformation and lowering the value of K_3. Thus the stiffer Y21M adopts the bend* deformation at a higher wedge angle due to a greater K_3 constant. As we approach the transition angle, for Y21M the defect accompanying the splay deformation is much higher in the wedge compared to *fd* . We suggest this reduces the curvature of the bend at the top of the wedge, and thus the respective energy cost. We note that with the splay deformation's director lines being straight no significant energy costs are associated with differences in flexibility. Similarly, simulations show that increasing K_3/K_1 gives an increase in the angle of the splay-bend* transition. Comparison of the experimental (figure 3.8(a)) and numerical (figure 3.8(b)) results enables us to estimate K_3/K_1.

fd: Simulations show the splay-bend* transition occurs at 72° for $K_3/K_1 = 1$ and at 82° for $K_3/K_1 = 4$. Moreover, for a fixed channel geometry the defect lies at a lower position in the wedge for increasing K_3/K_1. For $K_3/K_1 = 2$ the transition shifts to 76° but the position of the defect is lower than in the experiment. Thus, from the splay-bend* transition angle and the defect height we estimate $K_3/K_1 \approx 1$.

Y21M: Simulations show the transition occurs at 86° for $K_3/K_1 = 10$, and shifts to 92° for $K_3/K_1 = 20$. Thus we estimate $10 < K_3/K_1 < 20$. We comment that the transition is more abrupt for Y21M in contrast to the simulations. Currently we do not have an explanation for this slight discrepancy.

3.7 Conclusion

To conclude, we have used laser scanning confocal microscopy to image the director field of colloidal liquid crystalline virus suspensions on the single particle level. Thus it was possible to directly observe the nematic ordering in a microchannel patterned with wedges of varying opening angle. The complex interplay between confinement, elasticities and surface anchoring led to a splay to bend* transition mediated by a defect in the centre of the wedge. Numerical

results, in quantitative agreement with the experiments, enabled us to predict the position of the defect as a function of opening angle and elasticity, and elucidate its role in the change of director structure. We have shown that the rigid Y21M virus has an elasticity ratio, K_3/K_1, an order of magnitude greater than the more flexible *fd* virus. Our experiments have relevance to novel energy saving, liquid crystal devices [102] which rely on defect motion and pinning to create bistable director configurations.

Appendix: Elastic energy of an isolated wedge: method 2

We analytically evaluate the elastic free energy of the splay and bend* deformations by guessing expressions for the splay and bend* director fields in figures 3.1(b) and (c).

Splay: The splay deformation is described by $\mathbf{n} = \hat{\mathbf{r}}$, which we substitute into eq. (3.1):

$$\begin{aligned} G_s &= \frac{1}{2}K_1 \int (\nabla \cdot \mathbf{n})^2 dxdy \\ &= \frac{1}{2}K_1 \int_{\frac{\pi}{2}-\frac{a}{2}}^{\frac{\pi}{2}-\frac{a}{2}} \int_{r_{min}}^{r_{max}} \left(\frac{1}{r}\right)^2 r dr d\theta \\ &= \frac{K_1 a}{2} \ln\left(\frac{r_{max}}{r_{min}}\right). \end{aligned} \tag{3.12}$$

r_{min} and r_{max} are again introduced as the lower and upper cut-off radii of the wedge to avoid the divergence of the integral.

Bend:* We assume that the bend* deformation is described by the hyperbolas [103]:

$$y^2 = -p^2 + \tan^2\left(\frac{a}{2}\right) x^2, \tag{3.13}$$

where $x = y = 0$ defines the tip of the wedge, and p the point of intersection of the field lines with the x-axis. The director field in cartesian coordinate reads:

$$\mathbf{n} = (n_x, n_y) = \left(-\frac{y}{\sqrt{y^2 + x^2 \tan^4\left(\frac{a}{2}\right)}}, -\frac{x \tan\left(\frac{a}{2}\right)}{\sqrt{y^2 + x^2 \tan^4\left(\frac{a}{2}\right)}} \right). \tag{3.14}$$

Using eq. (3.14) the K_1 and K_3 terms in eq. (3.1) are evaluated and lead to:

$$\begin{aligned} g_b^1 &= (\nabla \cdot \mathbf{n})^2 \\ &= \frac{x^2 y^2 \tan^4\left(\frac{a}{2}\right)}{\sqrt{y^2 + x^2 \tan^4\left(\frac{a}{2}\right)}} \\ G_b^1 &= \frac{1}{2}K_1 \int_{\frac{\pi}{2}-\frac{a}{2}}^{\frac{\pi}{2}+\frac{a}{2}} \int_{r_{min}}^{r_{max}} g_b^1 r dr d\theta = K_1 \frac{2\pi - 2a + \sin(2a)}{8 \sin^2 a} \ln\left(\frac{r_{max}}{r_{max}}\right), \end{aligned} \tag{3.15}$$

$$
\begin{aligned}
g_b^2 &= (\nabla \times \mathbf{n})^2 \\
&= \frac{\tan^4\left(\frac{a}{2}\right)\left(y^2 - x^2\tan^2\left(\frac{a}{2}\right)\right)^2}{\sqrt{y^2 + x^2\tan^4\left(\frac{a}{2}\right)}} \\
G_b^2 &= \frac{1}{2}K_3\int_{\frac{\pi}{2}-\frac{a}{2}}^{\frac{\pi}{2}+\frac{a}{2}}\int_{r_{min}}^{r_{max}} g_b^2 r dr d\theta = K_3\frac{(2\pi - 2a)(2+\cos(2a)) + 3\sin(2a)}{8\sin^2 a}\ln\left(\frac{r_{max}}{r_{max}}\right).
\end{aligned}
\tag{3.16}
$$

Combining eq.'s (3.15) and (3.16) the total energy of the bend* configuration reads:

$$
G_b = \frac{(K_1(2\pi - 2a + \sin(2a)) + K_3((2\pi - 2a)(2+\cos(2a)) + 3\sin(2a))\ln\left(\frac{r_{max}}{r_{max}}\right)}{8\sin^2 a}. \tag{3.17}
$$

Equating G_s and G_b we find the transition angle between the two deformations as a function of the elastic constant ratio, K_1/K_3:

$$
\frac{K_1}{K_3} = \frac{(2a - 2\pi)(2+\cos(2a)) - 3\sin(2a)}{-4a + 2\pi + 2a\cos(2a) + \sin(2a)}. \tag{3.18}
$$

We note that the transition is independent of the wedge height, h_w, as we also found in section 3.2.

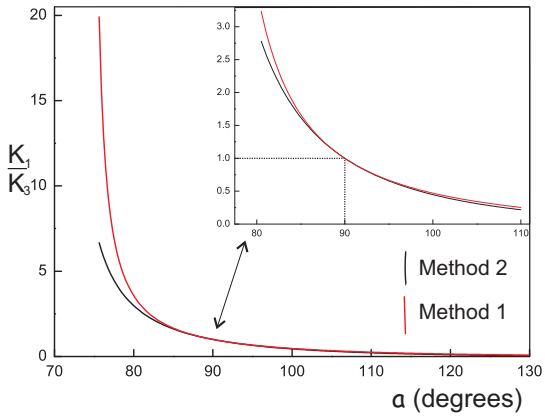

Figure 3.9: Plot of elasticity ratio, K_1/K_3, versus wedge opening angle, a (eq.'s (3.18) and (3.8)). Inset is a zoom for angles a=80-110°, with the dotted line highlighting the intersection of the two lines at $K_1 = K_3$, $a = 90°$.

Comparison of the two methods: By inspection the two methods find the same elastic energy of the splay deformation, $F_s = G_s$, but the bend* differs for the two methods $F_b \neq G_b$. In figure 3.9 we plot K_1/K_3 versus wedge opening angle, a (eq.'s (3.18) and (3.8)). We see that the two curves are in close agreement and intersect at $K_1 = K_3$ for $a = 90°$. The curves differ

as they diverge at different angles; $a \approx 71.0^\circ$ for method 2, and $a \approx 74.5^\circ$ for method 1.

Acknowledgments

This work was a collaboration with Ioannis Zacharoudiou and Julia M. Yeomans. We thank Paul van der Schoot and Ronald Otten for useful discussions.

Chapter 4

Effect of chirality on colloidal rods in wedge structured confinement

Abstract

We study the cholesteric of rod-like *fd* virus particles confined to channels with wedge-structured walls. Using laser scanning confocal microscopy we are able produce high resolution, 3D images of the cholesteric phase enabling us to visualise the twist at the single particle level. We observe a splay-to-twist transition as a function of the wedge opening angle, and interpret this in light of the various energies at play.

4.1 Introduction

Chirality occurs everywhere in the biological world [104] and liquid crystals are no different with the occurrence of a chiral cholesteric phase. The study of the cholesteric phase is of fundamental and technological importance. Fundamental, as the link between phase chirality and the microscopic properties of the particles is not yet fully understood for certain liquid crystals [105]. Technological, as the cholesteric phase of thermotropic liquid crystals can be used for the optical filtering of light in liquid crystal displays [106, 107]. New liquid crystal display technology is continuously emerging, a recent example being; cholesteric liquid crystal displays have been constructed on flexible substrates [108].

The cholesteric differs from a nematic in that its lowest energy state has a non-zero twist [2, 109]. This is explained within continuum theory by two elastic terms: K_t describes how the energy of the phase is lowered by twisting, and the familiar twist elastic constant, K_2 describes how the energy can be raised by twisting distortions of the director [31, 110]. The Frank-Oseen free energy accounts for the cholesteric phase by the q_0 term: $F_e = \frac{1}{2}K_1(\text{div } \mathbf{n})^2 + \frac{1}{2}K_2(\mathbf{n} \cdot \text{curl } \mathbf{n} + q_0)^2 + \frac{1}{2}K_3(\mathbf{n} \times \text{curl } \mathbf{n})^2$, where q_0 is related to the elastic constants and pitch, p, by $q_0 = -K_t/K_2 = 2\pi/p$.

Here we used the *fd* virus as a model colloidal rod suspension. *Fd*'s cholesteric pitch has been measured as a function of concentration, ionic strength and temperature [31], and as the concentration is increased the pitch decreases. This enabled us to decrease the pitch of the *fd* virus and extend our study of wedge structured microfluidic channels (chapter 3) to the cholesteric phase. We confined *fd*'s cholesteric phase to wedge structured channels of varying opening angle. The wedge geometry frustrates the cholesteric phase because it can not adopt both an undistorted twist and its preferred anchoring at the side walls: there will be an anchoring and/or elastic penalty. This means the cholesteric phase has three options, for the case of strong planar anchoring: (1) the twist can be suppressed causing an elastic penalty (figure 4.1(a)), (2) the twist can occur causing an anchoring penalty (figure 4.1(b)), or (3) the twist and planar anchoring can occur via the director bending, causing an elastic penalty (figure 4.1(c)). The option that is adopted is determined by the subtle interplay between anchoring strength and all three elastic deformations: splay, twist and bend, and thus sheds light on the respective energies. Furthermore, on moving away from the wedge tip, the distance between the side walls

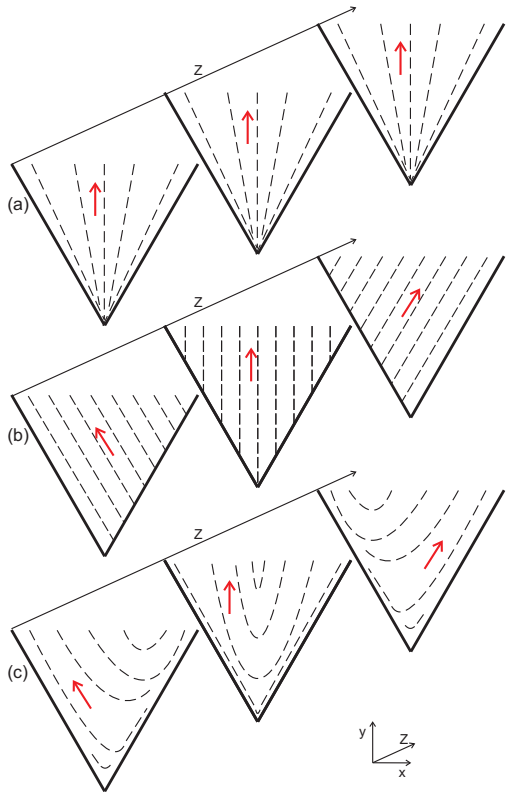

Figure 4.1: Three possible director fields for a cholesteric phase confined to a wedge. (a) The twist can be suppressed, causing an elastic penalty. (b) The twist can occur, causing an anchoring penalty. (c) The twist and planar anchoring can occur, via the director bending, causing an elastic penalty. The arrows highlight the local director.

of the wedge continuously increases, making the wedge a detailed tool for studying the effect of confinement on the cholesteric phase.

The chapter is organised as follows: we begin by explaining what is known about the origin of the cholesteric phase (section 4.2), we then briefly mention the experimental set-up (section 4.3), before presenting and discussing the results (section 4.4), we then finish with a conclusion (section 4.5).

4.2 Background: origin of the cholesteric phase of virus suspensions

Despite significant work, it is still not known what determines if a colloidal virus suspension adopts a nematic or cholesteric phase. All the filamentous viruses have a chiral microscopic structure, and you would expect this to be transferred to the macroscopic scale. However this

is not the case. Some viruses do display a cholesteric phase (e.g. *fd* and Y21M), but some are immune to the microscopic chirality and display an untwisted nematic phase (e.g. TMV and pf1) [61, 62, 111]. It has been shown that screening the chiral structure of *fd* by grafting an achiral polymer to the virus surface, surprisingly resulted in a cholesteric phase whose twist varied with ionic strength [58]. Implying that the molecular interactions determining the phase behaviour are very subtle [57].

The direction of the cholesteric twist and helix of the virus protein coat are not always complementary; the M13 virus has a right handed helix but the cholesteric phase has a left handed helix [110]. This led to the explanation that the cholesteric phase is formed from the helical charge distribution on the virus surface. Another explanation has been put forward that assumes viruses in solution form a helical structure and that mesoscopic interactions of these helices trigger the formation of a macroscopic cholesteric helix [58]. Tomar *et al.* have suggested that the helices are formed by interactions between positively charged major coat proteins and negatively charged DNA, because the addition of metal ions, which disrupt the DNA-protein interactions, changes the pitch of the cholesteric phase [111]. This helical suggestion is further supported by a study of *fd* and Y21M [62], where it is 'tentatively suggested' that the tighter pitch of the *fd* virus is related to the greater disorder in the viruses coat proteins.

4.3 Experimental

We used the *fd* virus and wedge structured channels as explained in chapter 3. We constructed channels with the dimensions; $d = 10$ μm, $h_c = 500$ μm, and $h_w = 70$ μm (illustrated in figure 4.2), and used *fd* at a concentration $[fd] = 105$ mg/ml. This concentration was just below the cholesteric-smectic phase boundary [112] and has a cholesteric pitch of $p \approx 19$ μm. We note that, Y21M has a pitch 1-2 orders of magnitude greater than *fd* for a given concentration. This means that to observe the twist significantly larger channels would be required. This complicates the problem because in our channels the top and bottom walls have a much greater area than the side walls, and consequently the anchoring at the top and bottom walls dominates, causing the twist axis to be parallel to the side walls. When one increases the depth of the channels and thus the area of the side walls, the twist axis is no longer restricted to the axis parallel to the side walls.

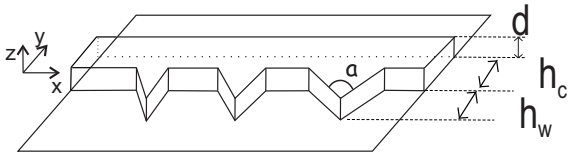

Figure 4.2: Geometry of the microfluidic channel.

4.4 Results and discussion

In the main channel we always observe the cholesteric twist, and in the wedge we observe a splay-twist transition, which is a function of the wedge opening angle. Figure 4.3 presents LSCM images at different z positions for a wedge with an opening angle of 32°, and we observe a twist in the channel and upper part of the wedge, and a splay in the lower half of the wedge. Figure 4.4 similarly presents LSCM images at different z positions for a wedge with a greater opening angle of 60°, and we observe a twist in the wedge, and a splay only in the tip of the wedge. Due to the presence of the main channel when a splay is adopted, there is always a splay-twist boundary present. The orientation of the rods at the splay-twist boundary changes with z position. For example in figure 4.3 at $z = 0.0$ μm we see a splay-bend boundary with a $s = -1/2$ defect, and at $z = 4.5$ μm we see an unsymmetrical boundary with defects at the walls. For all wedge angles we observe parallel anchoring with the side walls for both splay and twist deformations. In the main channel however we observe rods not anchoring parallel with the walls, but the channel is not our current focus.

Overlaying a series of images taken at different heights in the sample is equivalent to looking through the sample along the z-axis (we define the z-axis as the axis parallel to the side walls). A nematic's appearance does not depend on the axis it is viewed from, however, a cholesteric appears disordered/isotropic when viewed along the twist axis, see figures 4.5(a) and (b). Thus the splay twist boundary can be illustrated in 2D by overlaying the images of a z-stack. In figure 4.5(c) we overlay the 30 images from the z-stack corresponding to figure 4.3. Using this method we measure the height of the splay twist boundary by eye along the central axis of the wedge. In figure 4.6(a) we plot the splay-twist boundary height against wedge opening angle. The plot shows that for angles below 75° we observe a splay deformation accompanied by a splay-twist boundary, that moves up the wedge with decreasing wedge angle. For angles $\geq 75°$ a twist is observed in the whole wedge.

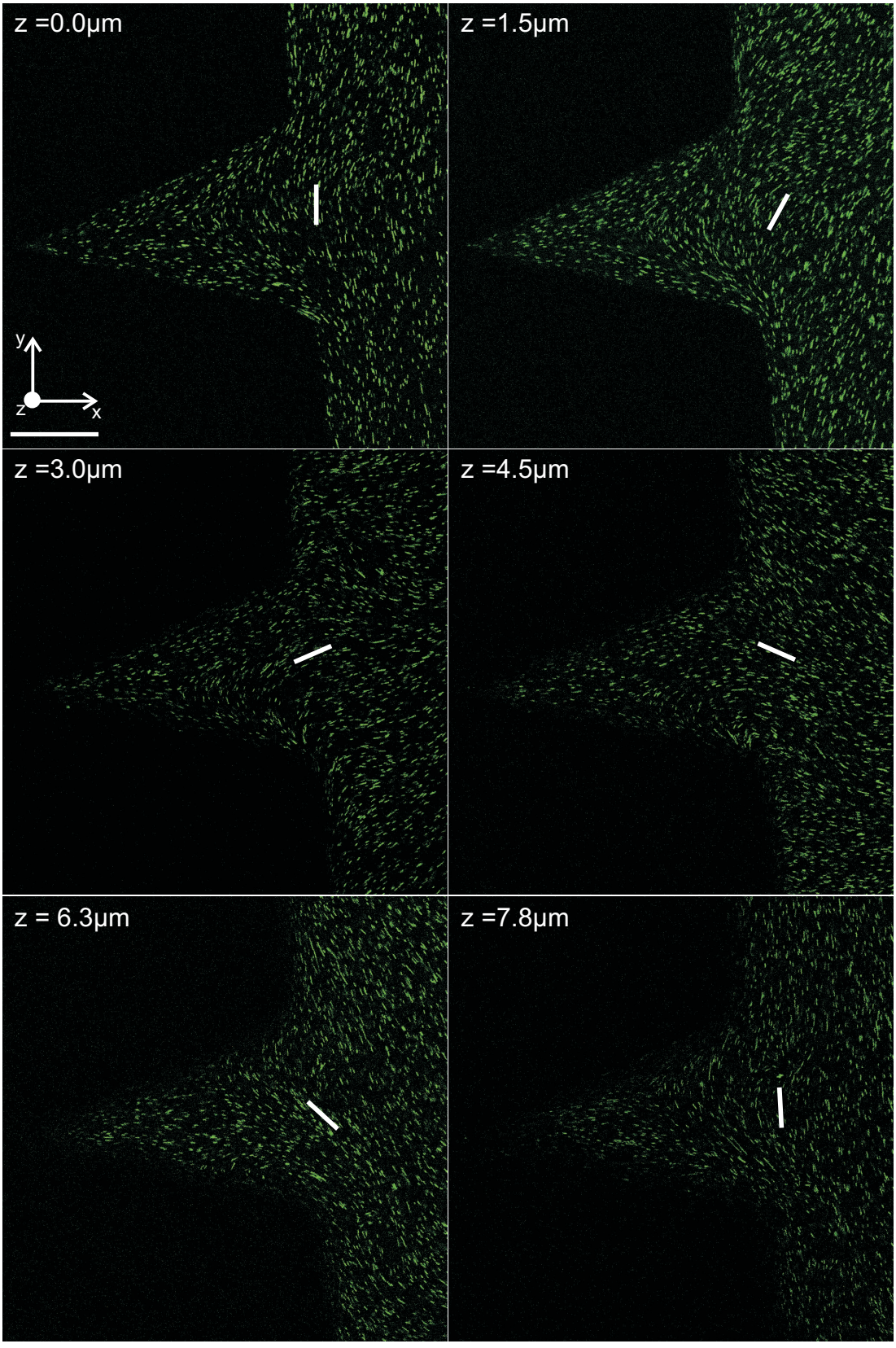

Figure 4.3: LSCM pictures at different z positions for a wedge with an opening angle of 32°. The director adopts a splay in the lower half of the wedge, and twists in the upper half of the wedge and channel. The overlaid white lines are a guide to the eye of the local director. The LSCM pictures are at the z positions specified, and each picture is obtained by overlaying 5 LSCM images. Scale bar = 20 μm.

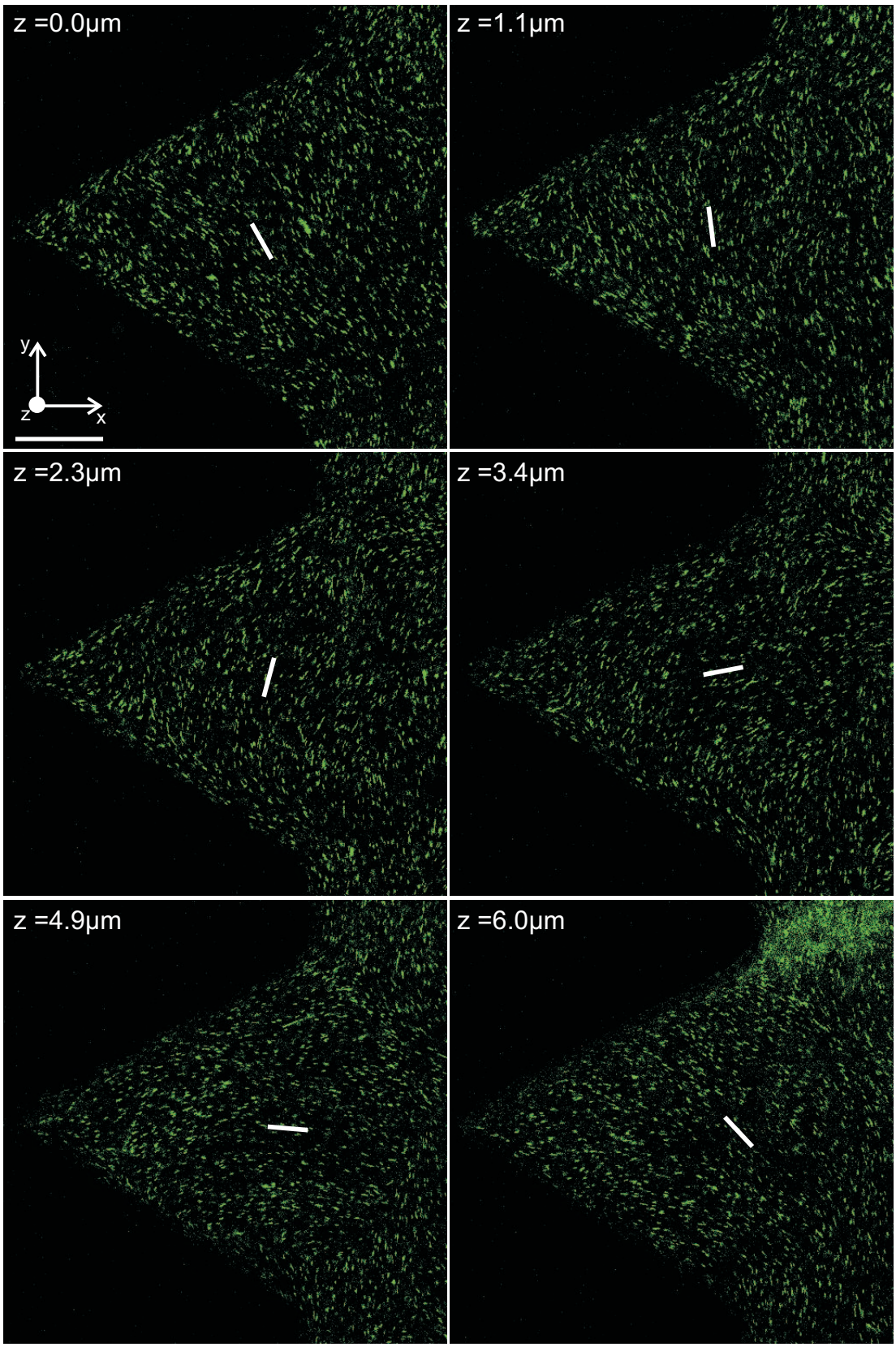

Figure 4.4: LSCM pictures at different z positions for a wedge with an opening angle of 60°. The director adopts a splay in the tip of the wedge, and twists above the wedge tip. The overlaid white lines are a guide to the eye of the local director. The LSCM pictures are at the z positions specified, and each picture is obtained by overlaying 5 LSCM images. Scale bar = 20 μm.

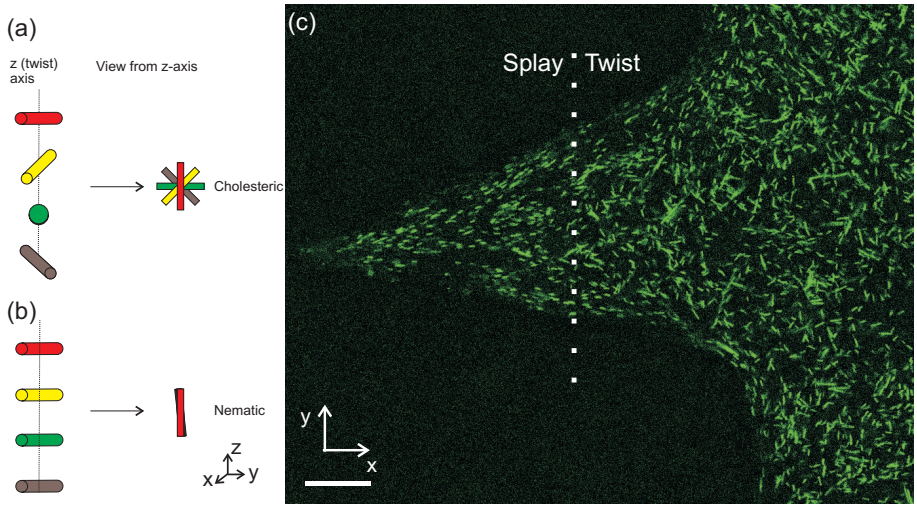

Figure 4.5: (a) and (b) Sketches of the cholesteric and nematic phase respectively. (a) Illustration of how the cholesteric phase appears disordered when viewed along the twist axis. (b) Illustration of how the appearance of the nematic does not change when the axis of view is changed. (c) Overlaid LSCM picture of the 30 images from the z-stack corresponding to figure 4.3 (z-stack step = 0.37 μm). The cholesteric phase appears disordered, enabling the splay-twist boundary to be visualized.

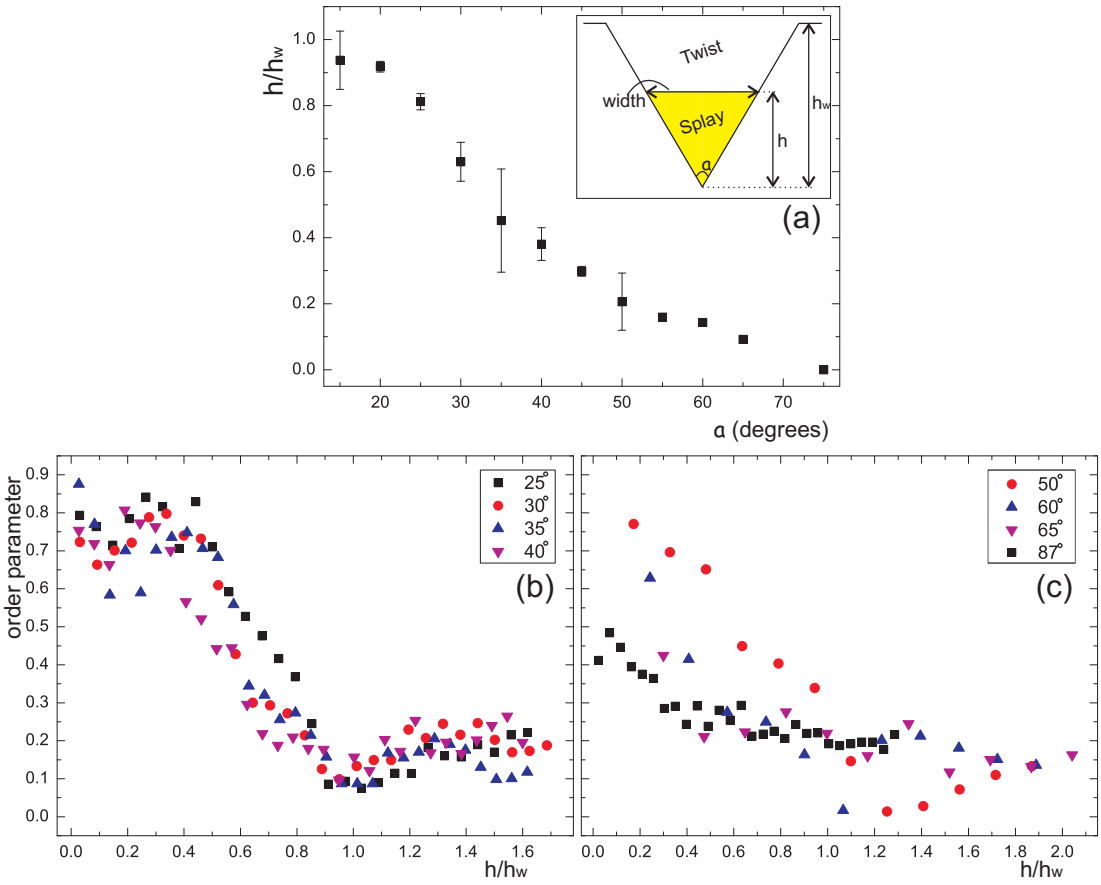

Figure 4.6: (a) Plot of height of the splay-twist boundary versus wedge angle. Inset: sketch of parameters used to define the wedge dimensions. (b) and (c) Plots of order parameter versus height in wedge.

To further quantify the splay-twist boundary we calculate the order parameter across the overlaid z-stacks. Calculating the order parameter from a z-stack will give low values for the cholesteric, and high values for the splay, as illustrated in figure 4.5. For each wedge we analyse 10 z-stacks of 30 images, giving us sufficient rods to be able to accurately measure the change in order parameter. The z-stacks are divided into rectangular segments from the tip of the wedge to the main channel. The rectangles in the tip of the wedge have the smallest number of rods due to the smaller area, but the minimum number of rods in these rectangles was still 80. In figures 4.6(b) and (c) we plot the order parameter versus rectangle height for a range of wedge angles. In figure 4.6(b), for angles 25-40°, we observe a drop in the order parameter from 0.8 to 0.2 as we move from the tip of the wedge to the main channel. This drop occurs closer to the wedge tip as the opening angle increases, which is expected as the splay-twist boundary is closer to the wedge tip. In figure 4.6(c) for angles 50-65°, we observe a very gradual drop in order due to splay only occurring in the tip of the wedge. For 87° we observe low order parameters throughout the wedge in agreement with the twist occurring throughout the wedge.

Splay-twist transition. When a twist occurs in the wedge, the fact parallel alignment also occurs at the side walls, as opposed to non-planar anchoring. Implies that the elastic energy cost of bending the director to align with the walls is less than the anchoring penalty. This is in-line with all other chapters in this thesis where strong anchoring is observed for the *fd* virus.

We observe a splay in wedges with opening angles less than 75°. For these wedges the energy cost of the splay must be less than the penalty that would occur if the director twisted and bent to align parallel to the side walls. The elastic energy cost of the splay is complicated and will have three contributions. Firstly, there will be a term for the energy cost of the splay proportional to K_1. In chapter 3 we derived the energy for the 2D case (eq. (3.12)), and it can trivially be extended to 3D by multiplying by the wedge depth. Secondly, there will be a K_t term describing the cost of suppressing the cholesteric twist. Thirdly, there will be a term proportional to the elastic constants, K_1 and K_3, describing the splay-twist boundary. The elastic energy cost of the twist that bends to align parallel to the side walls, will have a significant K_3 contribution but will also have contributions from K_1 and K_t. The anchoring penalty that would occur if the phase twisted will be proportional to the area of the side walls and the surface anchoring energy, w.

To try to understand the driver behind the splay-twist transition in figure 4.7(a) we plot

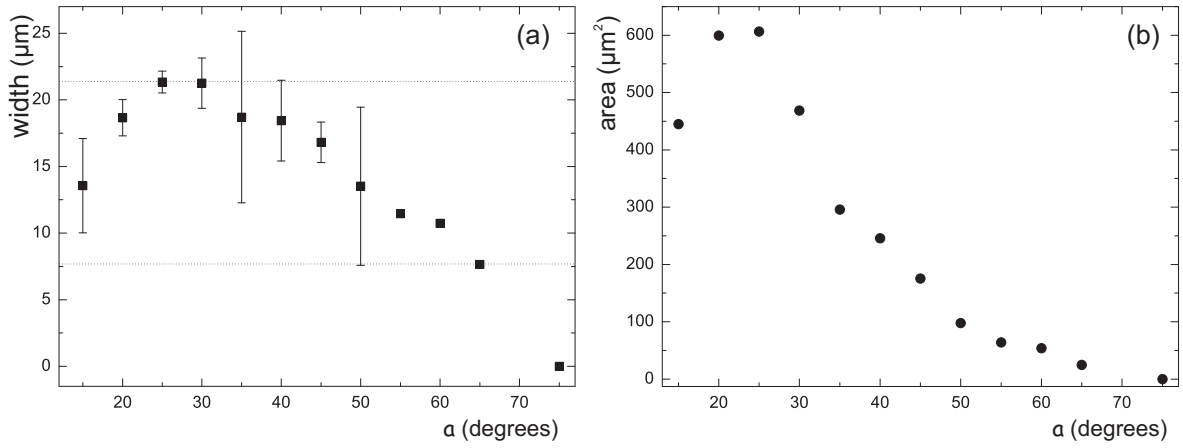

Figure 4.7: (a) Plot of width of the splay-twist boundary versus wedge angle a. (b) Plot of splay area versus wedge angle a.

the width of the splay-twist boundary, and in figure 4.7(b) we plot the total area of the splay. In both plots upon increasing wedge opening angle we observe a slight increase and then a decrease. Indicating that it is not simply the distance between the side walls that determines if a splay or a twist is adopted, but both the distance between the side walls and the area of the wedge.

The splay-twist and the splay-bend (chapter 3) transitions occur at the same wedge angle. This may be a coincidence, but it makes sense for the splay deformation to occur for a similar range of wedge opening angles. The difference between the two transitions is that the splay-bend transition is more sudden with the splay-bend boundary being pushed to the upper half of the wedge immediately after the transition angle.

Twist in the main channel. In contrast to the wedge in the main channel we observe the cholesteric twist and non planar anchoring at the side walls. Here the anchoring penalty is proportional to $\sim w\times$ wall area, and the elastic penalty from suppressing the twist is proportional to $\sim K_t^2/K_2\times$ channel volume [113]. We note that the anchoring energy w will vary with the specific angle of the director with the wall. The twist dominates over the anchoring penalty due to the volume of the channel being significantly greater than the area of the side walls, this effect must outweigh any differences in the elastic constants, K_t^2/K_2, and w.

4.5 Conclusion

We have measured a splay-twist transition and explained how the location and nature is determined by a subtle interplay of elasticity and anchoring strength. When the director twists in the wedge, it additionally bends to align parallel to the side walls. Indicating that the elastic bend penalty is lower than the anchoring penalty. Comparison with a theoretical analysis would yield an expression involving the elastic constants and/or the extrapolation length.

Chapter 5

Colloidal liquid crystals in rectangular confinement

Abstract

We investigate the director fields of rodlike viruses confined to shallow rectangular wells of varying aspect ratio. Laser scanning confocal microscopy is used to directly observe five distinct director fields. Results are interpreted in light of the Frank-Oseen energies, enabling the extrapolation length to be estimated. We measure an extrapolation length of the order of one rod length, in agreement with the strong anchoring boundary conditions we typically observe.

5.1 Introduction

Flat, portable, liquid crystal displays are taking a more prominent place in society. Over the past fifty years there has been a constant stream of new technology entering the market, from basic calculator screens to flexible tablet devices. It is well known that multistable liquid crystal devices in which the liquid crystal can adopt several stable orientations significantly reduce (and thus improve) power consumption [114,115]. A conventional liquid crystal display requires a continuous voltage to each pixel to maintain the 'on' and 'off' states, whereas a bistable liquid crystal display only requires a pulse voltage to switch between the states. The promise of bistability has inspired a significant amount of work on finding novel geometries that induce bistability, from arrays of posts to patterned surfaces [116–118]. Recently, square wells have been shown to induce bistablity for thermotropic liquid crystals [119,120]. Consequently the director profiles' energies have been evaluated numerically within the Landau-de Gennes theory [121] and also using the Frank-Oseen energy via conformal mapping [95].

Here, motivated by the recent interest, we study rodlike viruses confined to rectangles of varying aspect ratio. We begin this chapter by introducing the Frank-Oseen free energy calculations (section 5.2) and the experimental system (section 5.3). The subsequent sections present (section 5.4) and discuss (section 5.5) the observed director fields as a function of rectangle size and aspect ratio. Finally we conclude by considering the implications of this work (section 5.6).

5.2 Elastic energy of a 2D rectangle

The calculations were performed by Alexander Lewis supervised by Apala Majumdar, Peter Howell, Stephen Peppin, and Dirk Aarts at the OCCAM, University of Oxford [122].

To illuminate our experimental results the energies of a nematic liquid crystal confined to a shallow rectangular well of varying aspect ratio are computed. The energy of the well is considered using the Frank-Oseen energy: $F_e = \frac{1}{2}K_1(\text{div } \mathbf{n})^2 + \frac{1}{2}K_2(\mathbf{n} \cdot \text{curl } \mathbf{n})^2 + \frac{1}{2}K_3(\mathbf{n} \times \text{curl } \mathbf{n})^2$. The rectangular wells are modeled as 2D rectangles and strong anchoring is assumed, where the director aligns parallel to the side walls. Using the one constant approximation finding stable states of the director is equivalent to solving the Laplace equation, $\nabla^2\theta = 0$ (as was shown in section 3.2). The angle, $\theta(x, y)$ gives the orientation of the director field at a specified point.

From solving the Laplace equation an expression for $\theta(x, y)$ is obtained, which depends on the aspect ratio. From considering all combinations of strong anchoring boundary conditions three director fields are possible, one diagonal and two U-shaped structures, which are shown in figure 5.1(a). We note that each of the director fields in figure 5.1(a) has a degenerate mirror image.

The Frank-Oseen energies of the director fields are evaluated using $E = \frac{K}{2} \int \int |\nabla\theta|^2 dxdy$. A consequence of the strong anchoring boundary conditions is that in the rectangle corners defects are created. These are of strength $+1 \times \frac{1}{4}$ or $-1 \times \frac{1}{4}$, if a splay or a bend deformation is adopted, respectively. Point defects in two dimensions have an infinite Frank-Oseen energy. Thus to enable the integrals to be evaluated, arcs of radius ϵ are removed from the rectangle corners. In figure 5.1(b) the relative energies of the three director fields are plotted against one of the rectangle lengths l_j with the other length set to one, $l_i = 1$.

The diagonal director field has the lowest energy for all l_j values. As the aspect ratio increases, $l_j \to 0$ the energies of the D and U1 director fields converge, and similarly as the aspect ratio increases for larger channels, $l_j \to \infty$ the energies of the D and U2 structures converge. For $l_j < 1$ the director field bends with the longest edge for U1, and the shortest edge for U2. At $l_j = 1$ there is a crossover and for $l_j > 1$ the director field bends with the shortest

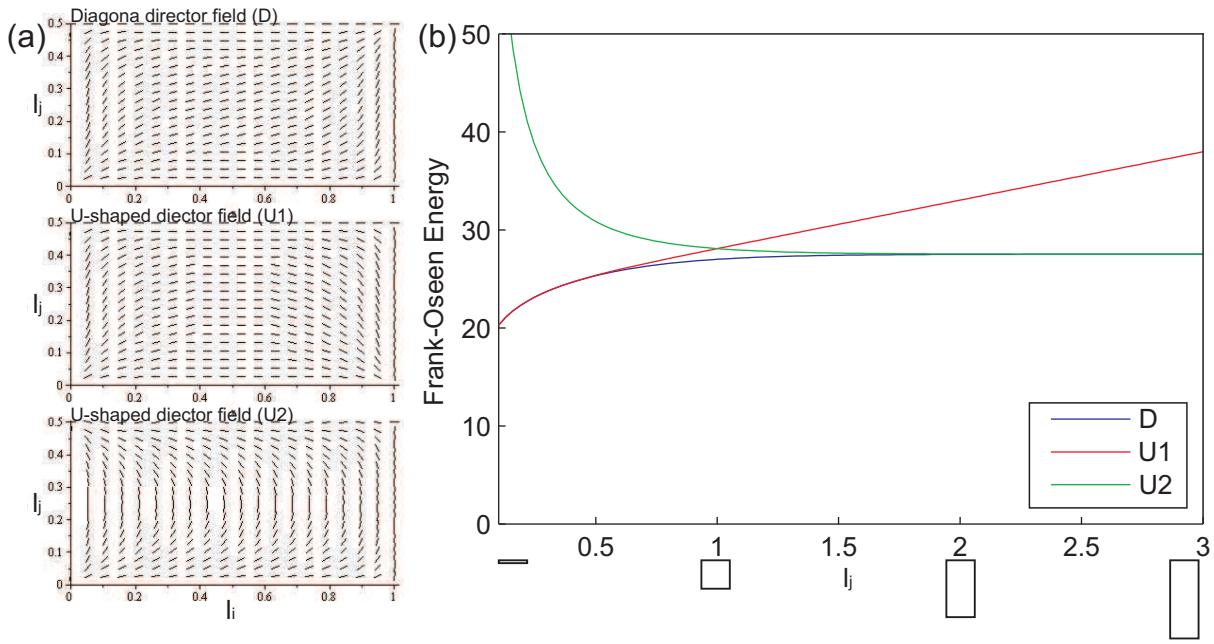

Figure 5.1: (a) Possible director fields for nematics confined to rectangles with dimensions: $l_j = 0.5$ and $l_i = 1$. (b) Plot of relative energies of the director fields in (a), versus rectangle length l_j, with the other length set to unity $l_i = 1$ ($\epsilon = 0.0001$).

edge for U1, and the longest edge for U2. This explains why at $l_j = 1$ the lines intersect, with the bend with the shortest edge always higher in energy.

5.3 Experimental set-up

We used the *fd* and Y21M viruses at concentrations; $c_{fd} = 24$ and 18 mg/ml, and $c_{Y21M} = 20$ and 13 mg/ml prepared as described in chapter 2. These concentrations are just above and below the isotropic-nematic biphasic region. We chose the lowest possible nematic concentration, as the lower the density of the nematic the lower the energy cost to re-arrange from one director field to another. This means that the rods are less likely to get stuck in high energy metastable states. Similarly, we chose the highest isotropic concentration possible to check if the confinement induced a nematic phase. Imaging of the labeled viruses was achieved using the Leica inverted microscope with the Yokogama CSU22 spinning disk unit and the Nikon C1 confocal microscope. The confocal microscope enabled us to acquire high resolution images and the spinning disk enabled us to follow the dynamics of the rods.

Soft lithography was used to create rectangular cells out of SU8 as described in chapter 2. The aspect ratio of the rectangles is characterised by $\lambda = l_i/l_j$, where l_i is the shorter side and l_j the longer side, as illustrated in figure 5.2(a). We constructed rectangles of size $l_i = 2$ to 50 μm with $\lambda = 0.0545$ to 1. The size enabled us to create 'chips' containing several hundred separate rectangular cells, see figure 5.2(b). This has the obvious advantage of enabling us to observe a large number of cells in one experiment. We used cell heights of 0.7, 2.5, 3, and 5 μm. The aim was to create cells as thin as possible to approximate 2D confinement. However, the cells of height 0.7 μm were very difficult to fill, thus we used 3 μm for the majority of experiments. We found that for all heights the rods lay in the plane of the rectangle. Additionally, 3D z-scans confirmed that the cholesteric twist was suppressed. Thus we are confident in assuming that all heights used can be considered as pseudo 2D confinement.

Before filling the chips were plasma cleaned for 1 minute. This ensured they were contamination free and hydrophilic. The chips were filled by pipetting a drop of the sample onto the chip, with the droplet spreading out due to the chip hydrophilicity. This resulted in the droplet 'hitting' the different cells at slightly different speeds and angles, meaning the initial orientation of the rods would vary from one cell to another. However, this variation was not significant as

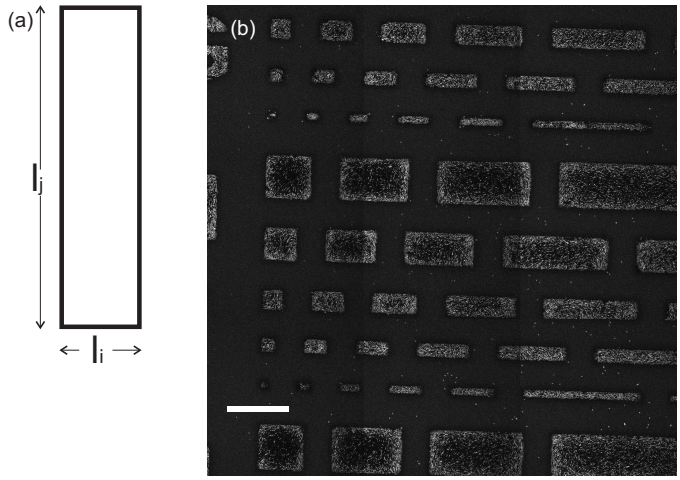

Figure 5.2: (a) Aspect ratio of rectangular cells; $l_i \equiv$ shortest edge and $l_j \equiv$ longest edge, with $\lambda = l_i/l_j$. (b) Microscope image of rectangular cells of varying size and aspect ratio. The area shown is $\sim \frac{1}{50}$ of the total chip area. Scale bar = 50 μm.

there was no pattern to the structures we saw, i.e. we did not see a given structure at the edge of the chip where the lowest filling speeds would have occurred. In each chip approximately 40% of the cells would be filled, with the remainder being partially filled or having deformed walls (the remainder were ignored).

5.4 Results

In figure 5.3 we present microscope and analysed images for the following observed director fields:

D Diagonal alignment with splay and bend deformations in opposite corners.

U U-shaped, bent alignment with splay and bend deformations in adjacent corners.

D* Diagonal alignment similar to D except one or both of the bend deformations is now a splay creating a s = -1/2 defect.

U* U-shaped, bent alignment similar to U except one or both of the bend deformations is now a splay creating a s = -1/2 defect.

L Alignment parallel to the longest edge, with perpendicular anchoring at the shortest edge.

The time between filling and observation on the microscope was roughly 20 minutes and in this time a nematic director field would have been adopted for nematic concentrations above the

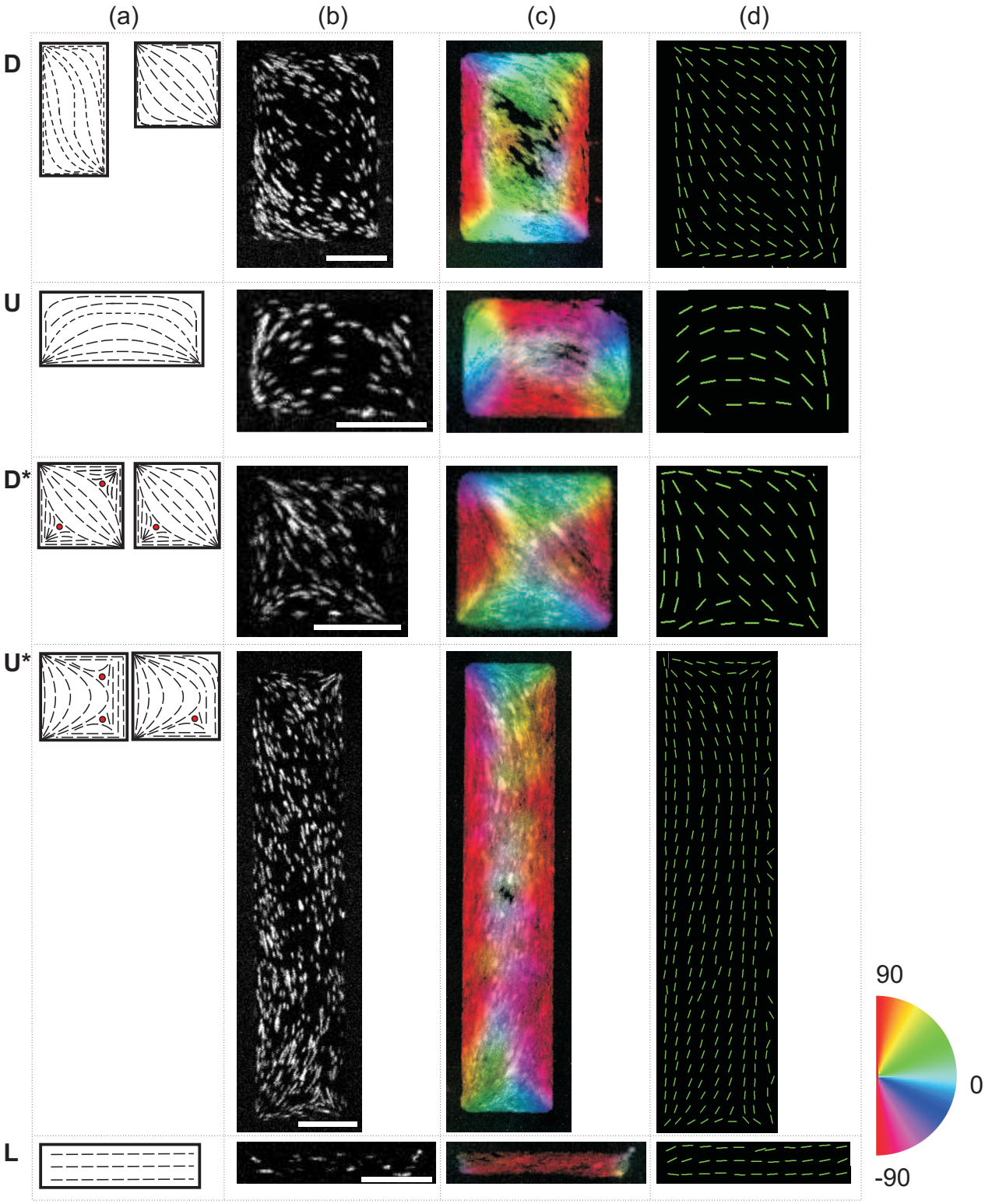

Figure 5.3: Director fields observed in rectangular cells for *fd* and Y21M, which we label: D, U, D*, U*, and L. We deliberately choose rectangles with different dimensions to illustrate the range used. (a) Sketch of the director field. D* and U* have defects highlighted with a red circle. (b) Four overlaid spinning disk confocal images. Scale bar = 10 μm. (c) 1000 overlaid microscope images with an added colour map. (d) Experimental director field calculated from a series of 1000 images.

biphasic region. We followed the director fields over 24 hours and found no change in the initial nematic director field. Thus in the initial twenty minutes the rods are able to find an energy minimum and adopt a metastable director field. We carefully say metastable, as certain director fields will be similar in energy, but have high energy barriers between them, with switching requiring a significant rearrangement of the director field. Numerically two mechanisms where the director changes from D to U have been studied for square chambers. In one, the defect moves along one of the side walls [119], and in the second, the anchoring at one wall is weaker than the remaining three, allowing the director field to change by non-planar anchoring occurring at one wall [121]. With no change of director fields occurring, we were not able to observe a switching process, but we suggest the former mechanism is more likely as we regularly observe defects but rarely non-planar anchoring.

Due to the rods rapidly finding a stable director field, we were not able to check if filling induced a certain director field (as we did for the wedges in chapter 3 and chapter 4). However, when we filled the cells with the isotropic phase below the biphasic region, a nematic was not induced and the sample remained isotropic. This implies that the filling (and confinement) were not sufficient to induce a nematic, and gives us confidence that our results are not filling dependent.

For the D and U director fields we do not distinguish between the degenerate mirror images. We note that for the specific case of a square ($\lambda = 1$) there are four degenerate U director fields. For D* and U* the majority of director fields had one defect but we group the director fields with one and two defects due to the low frequencies.

5.5 Discussion

In figure 5.4 we plot the phase space and in figure 5.5 we plot the director field frequencies against rectangle aspect ratio, λ, and length, l_i. 290 cells were analysed for Y21M and 57 cells were analysed for *fd* . Significantly more cells were analysed for Y21M, but *fd* shows similar trends. The immediate trend from figures 5.4 and 5.5 is that D is the dominant director field for both viruses. Upon decreasing aspect ratio the frequency of D decreases with it becoming equally frequent to director fields L and U for $\lambda \lesssim 0.2$. U is the second most common director field and with decreasing λ we see a gradual increase in frequency. The observation and frequency of

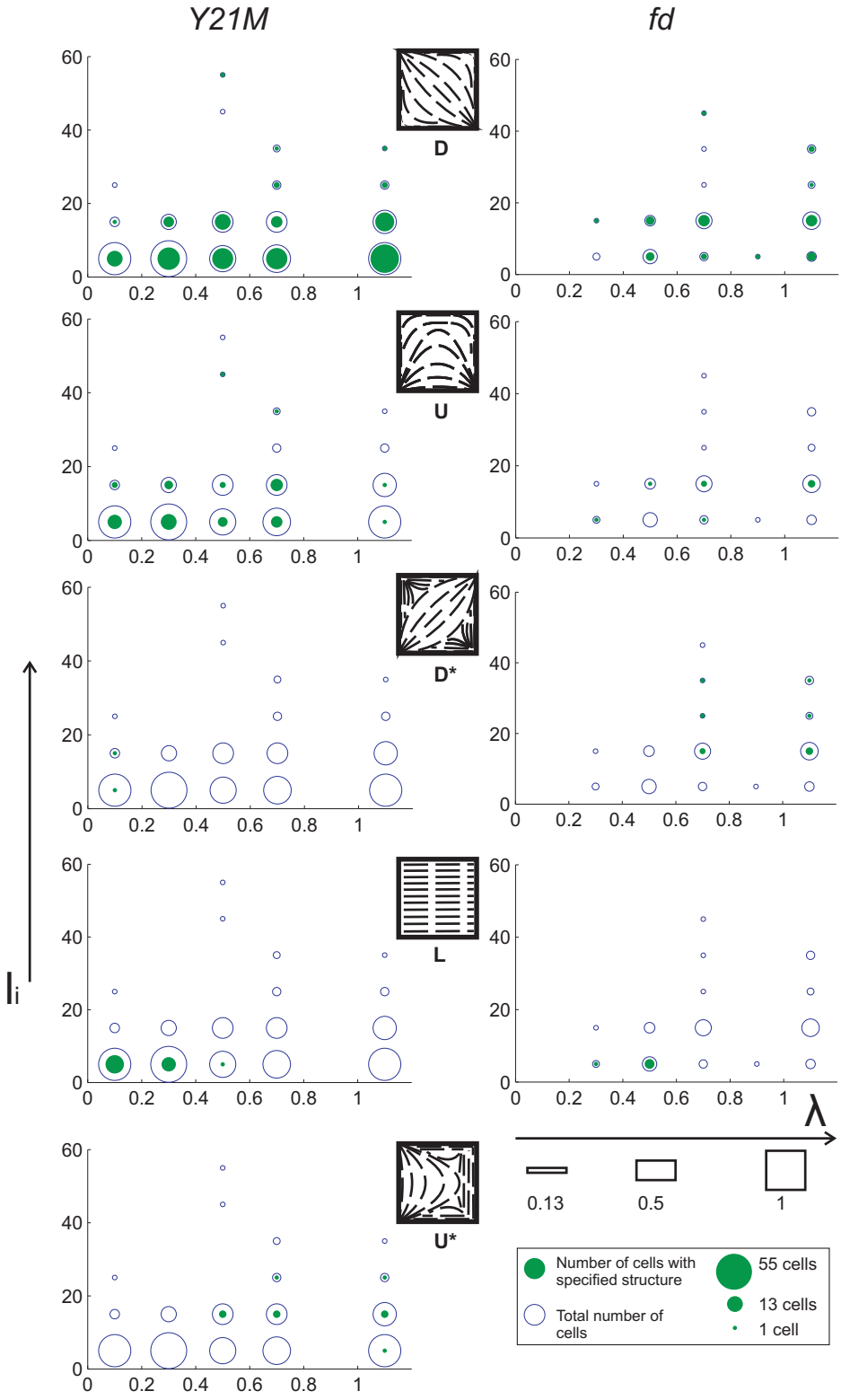

Figure 5.4: Phase space for rectangular cells. We plot the length of shortest side, l_i, versus the aspect ratio, λ, for the director fields in figure 5.3. The circle size is proportional to the frequency. The filled circle is the frequency for the specified director field. The unfilled circle is the total number of cells investigated for the given size and dimensions. The left hand side plots correspond to Y21M, and the right hand side plots correspond to *fd* .

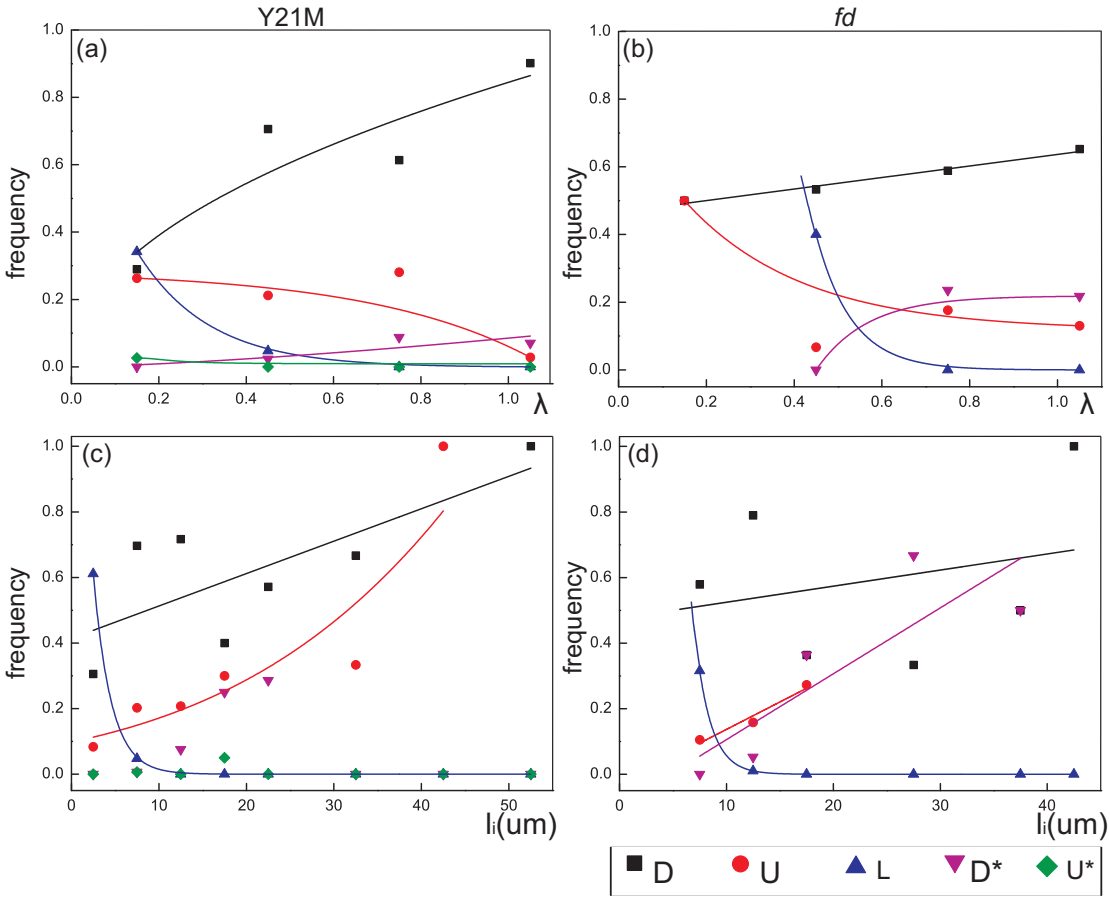

Figure 5.5: Frequency plots for the observed director fields. (a) and (b) Plots of frequency versus aspect ratio λ. (c) and (d) Plots of frequency versus length l_i. Lines are a guide to the eye of the trends.

these two director fields is in qualitative agreement with the theoretical analysis (section 5.2), where D has the lowest energy with U and D converging for high aspect ratios $\lambda \to 0$. Director fields D and U both have two splay and bend deformations, thus their energy difference arises from the difference in the curvature of the director away from the corners. Intuitively D and U should have equal energies at low aspect ratios: with decreasing aspect ratio, the director becomes increasingly parallel to the longer side wall, l_j, and once it has become parallel the elastic energy cost does not vary with the relative position of the splay and bend deformations. D and U have been observed for thermotropic liquid crystals confined to square wells: Yi *et al.* used topological patterns to align the diagonal providing a method to switch between the two degenerate D director fields [120], and Tsakonas *et al.* observed both D and U director fields [119].

L, D*, and U* are the most striking director fields, and they have not been reported before. We only observe L for narrow high aspect ratio rectangles, but for these highly confined

rectangles it is a frequent structure. Throughout this thesis we nearly always observe strong anchoring at walls, however at these dimensions we must reach the limit where the elastic penalty equals the anchoring penalty. Director fields D* and U* are very similar to D and U with one or both the bend deformations being replaced with a splay, creating a $s = -1/2$ defect. For *fd* we have found $K_3/K_1 \approx 1$ (chapter 3) meaning the splay and bend deformations have equal energy costs. Thus we expect D* to be higher in energy than D, with the difference being the cost of the $s = -1/2$ defect. For Y21M it is less clear, with $K_3/K_1 \approx 20$ (chapter 3) there is an energy gain from the system adopting the lower energy splay, but an energy cost from the $s = -1/2$ defect. The greater frequencies of D and U strongly imply that D* and U* are higher in energy. We are wary from interpreting anything from the fact we don't observe U* for *fd* , as this could be because less rectangles were analysed than for Y21M.

We note that the U2 director field where the bend occurs with the short side of the rectangle (figure 5.1(a)), was not observed in our experiments. This is not surprising for high aspect ratios, $l_j < 0.5$ ($l_i = 1$), as U2 is very high in energy, but for $0.5 < l_j < 1$ ($l_i = 1$), U2 is not significantly greater in energy than D and U1. Combined with the fact that D is the most dominant director field, implies that the all director fields observed have energies between the Frank-Oseen energies of D and U2, i.e. we are not observing high energy metastable states.

Anchoring strength. In figure 5.5 for Y21M we observe that the L state becomes equally frequent to D and U at dimensions: $\lambda = 0.18$ and $l_i = 3$ and 5.5 μm respectively. By assuming that the energies are equal when the director fields are equally frequent we are able to estimate the anchoring strength, w, in terms of the average elastic constant, K. The energy cost of the director field L does not have an elastic contribution. The anchoring penalty is proportional to the area where perpendicular anchoring occurs:

$$E_L = 2l_i hw, \tag{5.1}$$

with h being the depth of the rectangle well. The Frank-Oseen energy evaluation discussed in section 5.2, leads to expressions for the energies of the director fields D and U, as a function of the rectangle dimensions. Inputing the dimensions: $l_i = 3$ and $l_j = 16.66$ for the L-D crossover and $l_i = 5.5$ and $l_j = 30.55$ for the L-U crossover we obtain:

$$E_D = 17.2 \text{ K}, \qquad E_U = 19.6 \text{ K}. \tag{5.2}$$

Where K is an average elastic constant, and a value of ϵ has been used that is equivalent to the rod diameter. Equating eq. (5.1) with eq. (5.2) we express the anchoring penalty, w, in terms of K and obtain the extrapolation length ξ (eq. (1.4)):

$$\begin{aligned} E_D &= E_L & E_U &= E_L \\ \xi &= \frac{\mathrm{K}}{w} = 1.05\mu m & \xi &= 1.68\mu m \end{aligned} \tag{5.3}$$

The one elastic constant has been used to obtain the energies in eq. (5.2), which does not strictly apply to Y21M, and we will discuss this below. The one constant approximation does apply to *fd* and following an identical argument of equating expressions for E_D and E_L we find:

$$\xi = 2.22\mu m, \tag{5.4}$$

for dimensions $l_i = 7.4$ and $l_j = 16.88$.

Both ξ values are of the order of the rod length, which is what you would expect for a colloidal liquid crystal system which displays strong anchoring [64, 123, 124]. The extrapolation length ξ is greater for *fd* than Y21M. ξ depends on the elastic constants K_1 and K_3, and the anchoring penalty w. K_3 will be greater for Y21M compared to *fd* (chapter 3). However it is not clear if there will be a difference in K_1. The effect of rod flexibility on the anchoring strength has not been fully studied, although it may be possible via several reported methods [125, 126]. Physically, w is the interaction of a liquid crystal particle with the wall: $\sim E_{wn}/LD$, where E_{wn} is the interaction energy between the wall and the rod, L the rod length, and D the effective diameter. For the more flexible *fd*, D will be greater, and E_{wn} will be greater due to the greater entropy penalty from confinement by the wall. It is difficult to state with certainty what is the dominant effect, but our measurements suggest that w is lower for *fd*, dominating any differences in K, resulting in *fd* having a greater ξ value.

Use of the one constant approximation. To understand the effect of using the one constant approximation for Y21M we measure the difference in θ for the experimental and numerical director fields. In figure 5.6(a) and (b) the experimental and theoretical director fields are plotted, with the blank regions corresponding to regions where there were no fluorescently labeled rods. In figure 5.6(c) a colour map illustrates the absolute difference in θ. In these three typical examples we observe reasonable agreement between the director fields. Also this indicates that

is is difficult to learn about the elastic constant ratio by simply examining the director fields.

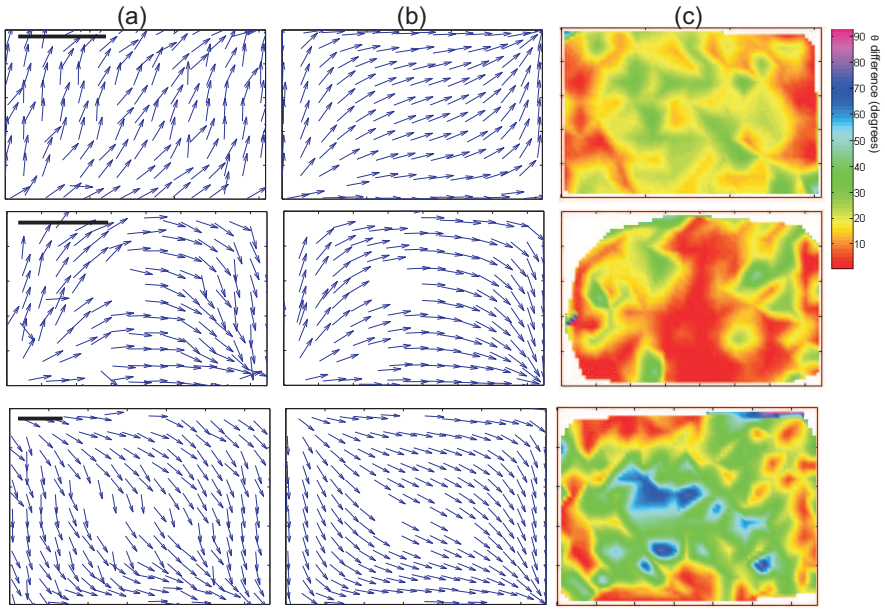

Figure 5.6: Comparison of experimental and numerical director fields for three typical rectangular cells. (a) Director fields for Y21M. (b) Director fields predicted by the Frank-Oseen energy, within the one constant approximation. (c) Colour map of the difference in θ values between the experimental and numerical director fields. Scale bar =5 μm.

5.6 Conclusion

We have used laser scanning confocal microscopy to image the director of rod-like viruses in rectangular confinement. We observe five distinct director fields whose frequency varies with rectangle aspect ratio and size. The same structures and similar trends are observed for both *fd* and Y21M. The Frank-Oseen energy computations show that D is the lowest energy director field with U converging for high aspect ratios, and the observed experimental frequencies are in agreement. Additionally, we observed director field L in similar frequencies to D and U for high aspect ratio rectangles. By assuming that for these rectangle dimensions the energy of L is similar to that of D and U, the extrapolation length has been estimated and found to be of the order of a rod length for both viruses. The low frequencies of U* and D* indicate that these director fields are slightly higher in energy, with the difference being related to the energy cost of defects of strength $s = -1/2$. Future theoretical work that calculates the Frank-Oseen energies without the one constant approximation would enable a more accurate comparison for Y21M.

Acknowledgments

This work was a collaboration with Gijsje Koenderink's group and Apala Majumdar's group. The experiments were undertaken with José Alvarado, supervised by Gijsje Koenderink, at the AMOLF, Amsterdam. The energy calculations were performed by Alexander Lewis, supervised by Peter Howell, Dirk Aarts, Stephen Peppin, and Apala Majumdar.

Chapter 6

Colloidal liquid crystals in annular confinement

Abstract

We investigate the director fields of rodlike viruses confined to shallow circular and annular cells. Laser scanning confocal microscopy is used to directly observe the director fields. The experimental observations are interpreted using Monte Carlo simulations of finite sized rods. This work shows the nematic structures that emerge when confinement is on the length scale of the particles and shines light on the applicability of continuum theories down to microscopic lengthscales.

6.1 Introduction

Confinement of nematic liquid crystals causes the director field to elastically distort and/or pay an anchoring penalty. For the *fd* virus we have already seen examples of distorted director fields, defects and non-planar anchoring, created when wall geometry and the nematic director are incompatible (Chapters 3-6). We have made successful comparisons between our experimental results and the Frank-Oseen and Landau-de Gennes theories. Both these theories assume the liquid crystal is a continuum, and ignore the particle dimensions [1, 127]. At significantly confined geometries, where the dimensions approach the rod length, we expect continuum theories to no longer be accurate. Accessing this regime with thermotropic liquid crystals is an experimental challenge. The lengthscale of thermotropic liquid crystals are of the order of nm [1] and producing cells on the nm scale is now possible, but involved and expensive [128, 129]. We assume this is why there have been few studies of thermotropic liquid crystals in geometries where the confinement is of the order of the particle size. In contrast, colloidal liquid crystals rod lengths are on the μm scale, and well established soft lithography protocols can produce structures on the μm scale quickly and inexpensively [73] (chapter 2). Despite this little work has been done on colloidal rods, although experiments have studied spherical colloids in highly confined geometries [130, 131]. Possibly, this is because polarized light microscopy, a common technique for visualising the director, will not produce sufficient contrast on geometries $\lesssim 10^3 \mu m^3$ [124]. Previous work on granular rods in circular chambers less than 10 rod lengths in diameter, observed a switch from a bipolar structure to a uniform structure with increasing density [132]. The experiments were compared to Frank-Oseen energy evaluations enabling the elastic constant ratio to be estimated. Similarly, bipolar and uniform director fields have been observed in nematic tactoids for several systems such as TMV, carbon nanotubes, and gibbsite platelets [61, 124, 133]. However for these systems the tactoids dimensions were much greater than the particle length.

Here we study colloidal rods confined to circular and annular cells. In moving from a circular to an annular geometry the presence of the inner hole puts an additional anchoring constraint on the system. That competes with the anchoring at the outer wall and the nematic bulk order. For finite-sized particles, one expects that the size of the inner hole with respect to the particle length becomes relevant. We access this regime by making the diameter of the cells of the order of the rod length. This work shows the new nematic structures that emerge when

confinement is on the length scale of the particles.

The chapter is organised as follows; we begin by presenting numerical results of Monte Carlo simulations that take into account liquid crystal particle size (section 6.2), and then briefly describe the experimental set-up (section 6.3). We then present and discuss the experimentally observed director fields for circular and annular confinement (section 6.4), and finish with a conclusion (section 6.5).

6.2 Monte Carlo simulations

The simulations were performed by Ioana C. Garlea and Pieter Mulder supervised by Bela M. Mulder at the AMOLF.

The simulations modeled rigid hard spherocylinders with diameter D, which sets the length (D = 1), and length L in the range 15-25 units. The particles were confined to thin geometries with a height of 1 (the true 2D case), 3 or 6 units between the top and bottom walls. This limitation on the height of the sample precluded the particles from rotating out of the plane and enforced an effectively planar configuration of the particle axes, whilst not completely constraining the in plane centre of mass for sample heights 3 and 6 units. The only interactions were steric: particles were not allowed to overlap with each other, nor cross the confining walls. A standard Monte Carlo algorithm [134, 135] was used to sample the equilibrium configurations.

Simulations were run for an outer radius of 40 units. The rod length, inner radius and the height of the sample were systematically varied. Note that the packing fraction was below the bulk isotropic-nematic transition, indicating that ordering was boundary induced. For the circular geometries (inner radius = 0) with increasing rod length there is a transition from a bipolar pattern (figure 6.1(a)) to an almost homogeneous nematic state (figure 6.1(c)), via intermediate states where the defects are 'expelled' from the circle (figure 6.1(b)).

For the annular geometries (inner radius > 0) equilibrium configurations were found with n-fold symmetries consisting of well-ordered domains separated by disclination lines, as shown in figure 6.1(d)-(f). To rationalize the observed patterns it is assumed that the packing of particles around the smaller inner hole is the dominant factor. A simple geometric construction yields the ratios between the inner diameter, d_i, and the particle length, L, for which n co-planar particles

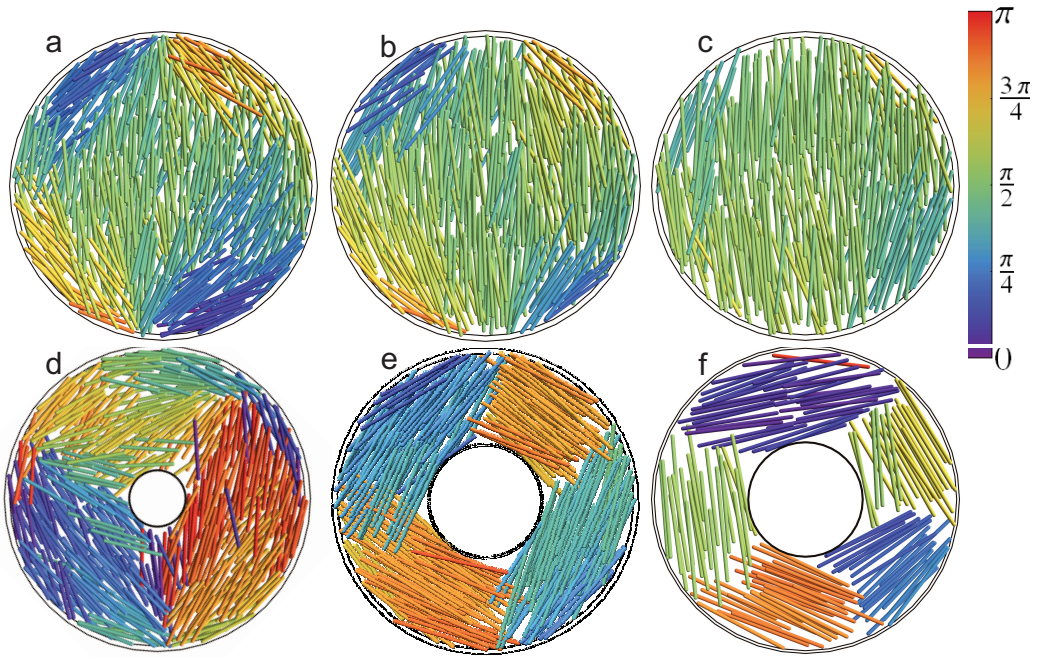

Figure 6.1: Monte Carlo simulations for finite length rods in circular and annular confinement. (a) - (c) Snapshots of equilibrated suspensions of rods in circular cells. (d) - (f) Snapshots of equilibrated suspensions or rods in annular cells. Chamber thickness = 6D. Rod colour corresponds to orientation.

tangent to the inner boundary can be fitted around the hole without overlapping:

$$d_i(n) = \frac{L}{\tan(\frac{\pi}{n})} \tag{6.1}$$

Remarkably, for the pure 2D systems where the height of the sample equals the particle diameter, the formula above correctly predicts the observed number of domains. When the height increases the number of domains observed falls behind the predicted number, the more strongly so for the less dense systems. Note also, that the formula captures the fact that the degenerate case of packing two particles around the hole is possible for any radius larger than $d_i(2) = 0$, consistent with the observation that the bipolar pattern is indeed observed for radii less than $d_i(3) = 3^{-0.5}L$.

6.3 Experimental

We used the *fd* virus, which was prepared as described in chapter 2. The following nematic and isotropic concentrations were used, which are above and below isotropic-nematic biphasic region: $[fd]_{nem} = 23$ mg/ml, and $[fd]_{iso} = 18$ mg/ml. We chose the lowest possible nematic concentration (similar to chapter 5), as the lower the density of the nematic the lower the energy cost to re-

arrange from one director field to another. This means that the rods are less likely to get stuck in high energy metastable director fields. Imaging of the labeled viruses was achieved using the Leica inverted microscope with the Yokogama CSU22 spinning disk unit and the Nikon C1 confocal microscope. The confocal microscope enabled us to acquire high resolution images and the spinning disk enabled us to follow the dynamics of the rods.

Soft lithography was used to create annular cells out of SU8 as described in chapter 2. The cell shape is specified by the outer diameter, d_o and inner diameter, d_i, illustrated in figure 6.2. We systematically controlled the annular shape, within the following ranges; $10 \leq d_o \leq 70$ μm, and $0 \leq d_i/d_o \leq 0.7$, with $d_i/d_o = 0$ corresponding to a circle. Similar to chapter 5 the small cell size enabled us to create 'chips' containing several hundred separate cells. We used a cell thickness of 1 μm for all experiments. We found that the rods lay in the plane of the cell and 3D z-scans confirmed that the cholesteric twist was suppressed.

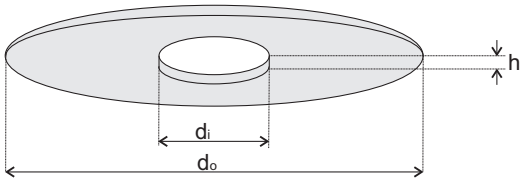

Figure 6.2: Sketch of an annular cell. Parameters d_o and d_i correspond to the outer and inner diameter.

6.4 Results and discussion

In figure 6.3 we present microscope and analysed images, for the following observed director fields:

U Director aligns with both inner and outer walls. No defects are observed.

D_2 Two $+1 \times \frac{1}{2}$ defects at the outer wall. The defects are diametrically opposite.

D_3 Three $+1 \times \frac{1}{2}$ defects spaced evenly at the outer wall.

S_1 One $+1 \times \frac{1}{2}$ defect at the outer wall.

S_2 Two $+1 \times \frac{1}{2}$ defects at the outer wall. In contrast to D_2 the defects are not diametrically opposite.

N No elastic distortion of the director.

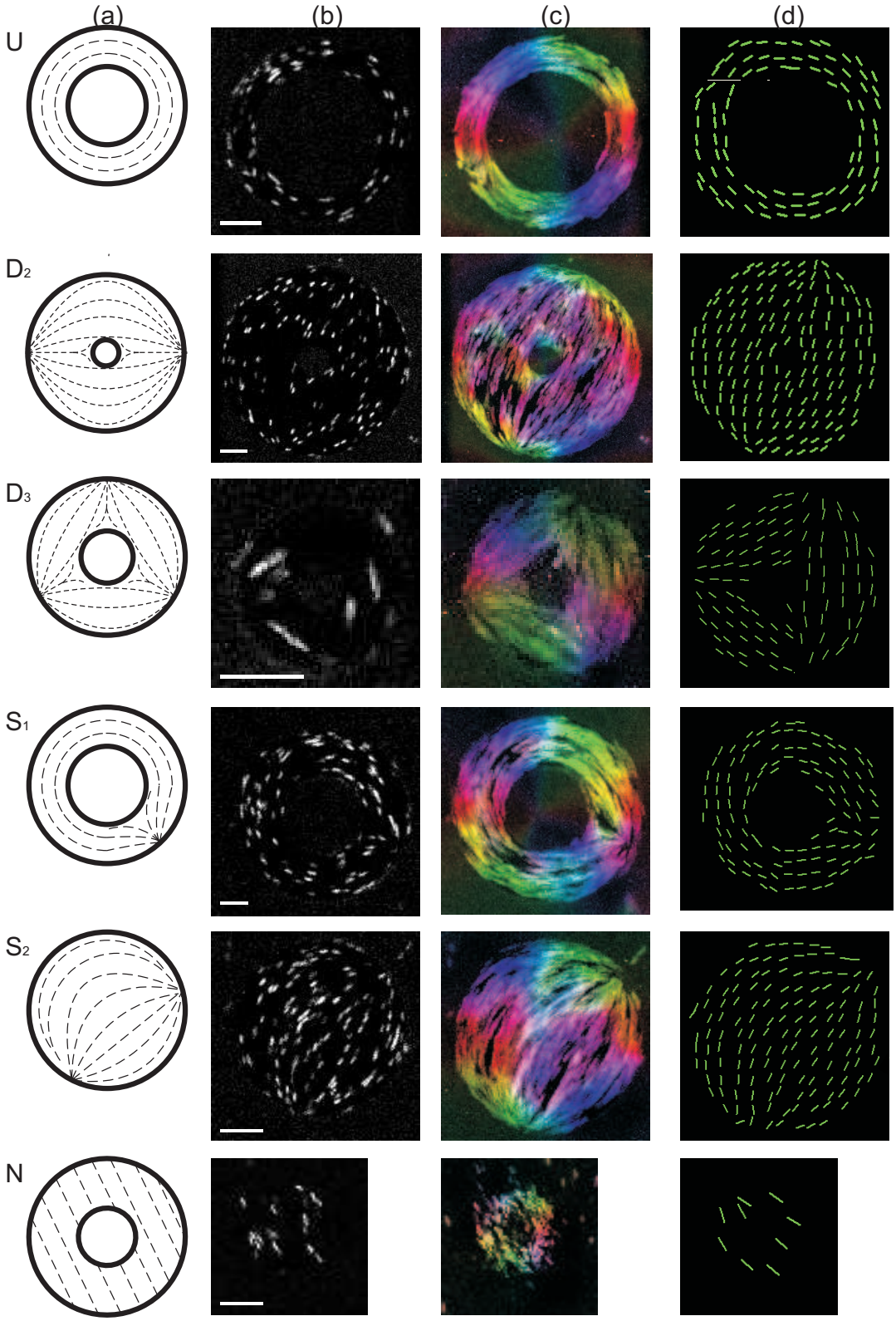

Figure 6.3: Structures observed in circular and annular cells for *fd* , which we label: U, D_2, D_3, S_1, S_2, and N. (a) Sketch of the director field. (b) Four overlaid spinning disk confocal images. Scale bar = 5 μm. (c) 1000 overlaid microscope images with an added colour map. (d) Experimental director field calculated from a series of 1000 images.

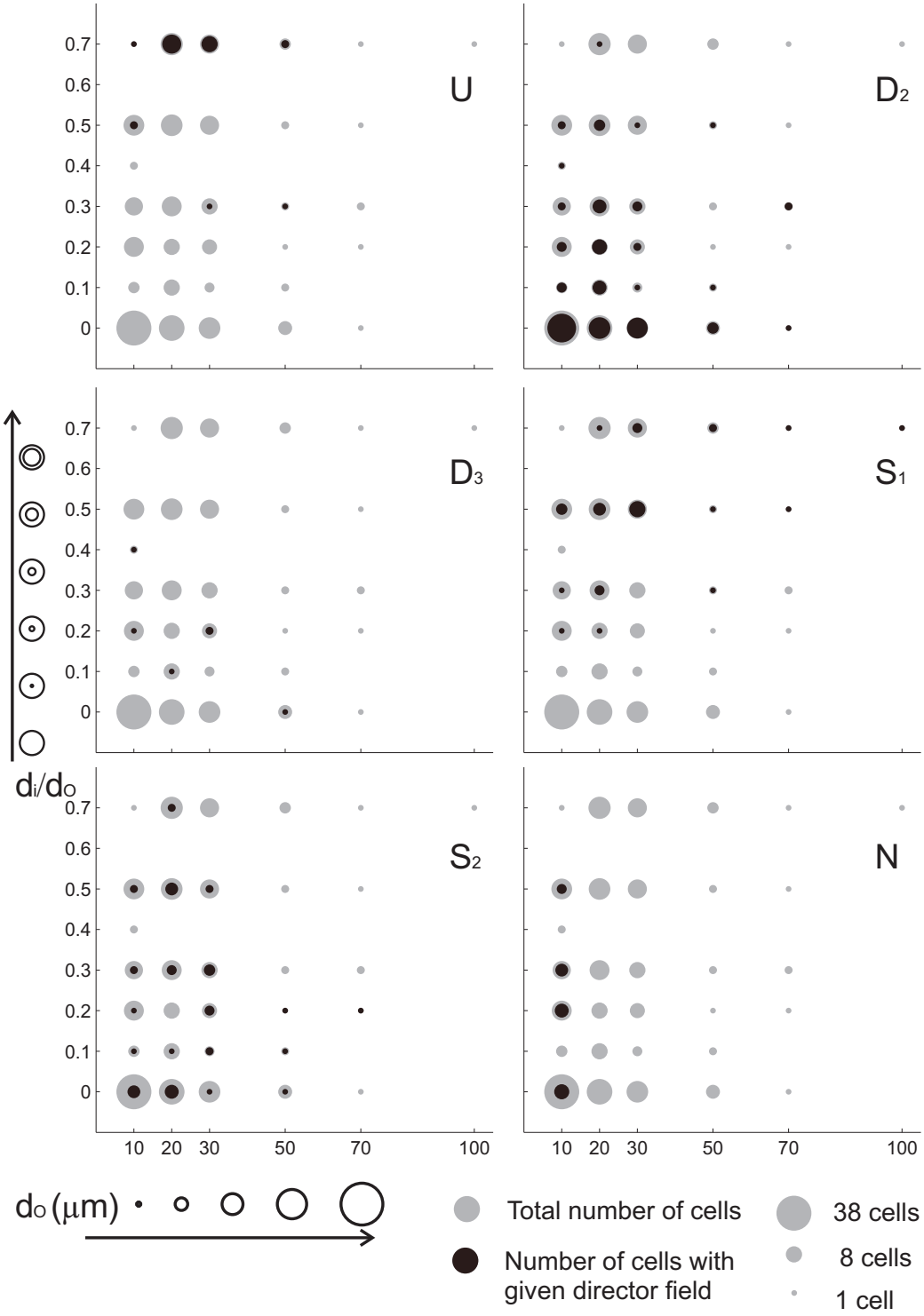

Figure 6.4: Phase space for the director fields observed in annular cells (shown in figure 6.3). We plot the ratio of the inner diameter to outer diameter, d_i/d_o, versus the outer diameter, d_o. The circle size is proportional to the number of director fields. The black circle is the number of cells with the specified director field. The grey circle is the total number of cells investigated for the given cell dimensions.

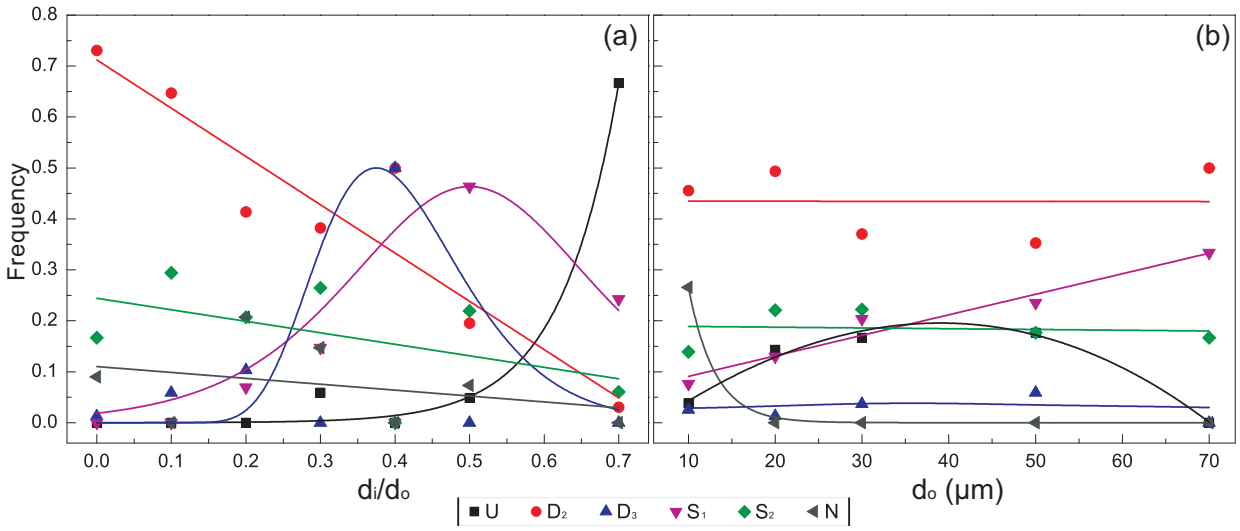

Figure 6.5: Plots of frequency versus: (a) ratio of inner to outer diameter, d_i/d_o, and (b) outer diameter, d_o, for the observed director profiles.

In total, 234 cells were analysed. The time between filling and observation on the microscope was roughly 20 minutes and in this time a nematic director field would have been adopted for nematic concentrations above the biphasic region. We followed the director fields over 24 hours and found no change in the initial nematic director field. Due to the rods rapidly finding a stable director field we were not able to check that filling did not induce a nematic director field (as we did for the wedges in chapter 3 and chapter 4). However, when we filled the cells with the isotropic phase below the biphasic region, a nematic was not induced and the sample remained isotropic. This implies that the filling (and confinement) were not sufficient to induce a nematic, and gives us confidence that our results are not filling dependent.

In figure 6.4 we plot the phase space for the director fields, and in figure 6.5 we plot the frequencies against d_i/d_o, and d_o. The clear pattern as we increase d_i/d_o and move from circular to annular cells with increasing inner hole diameter is the following; D_2 is dominant for circular cells, for intermediate values of d_i/d_o we see D_3 and then S_1 become dominant, and finally for the greatest d_i/d_o ratios, corresponding to thin annular cells U becomes dominant. The director fields S_2 and N are never the most frequent and decrease linearly with increasing d_i/d_o. Varying the cell outer diameter d_o has less of an effect on structure frequency compared to d_i/d_o. D_2 has the greatest frequency for all cell diameters d_o, and has no dependence on d_o. The frequency of S_1 increases linearly with increasing d_o. N only occurred for small diameters, $d_0 < 10$. U occurs for intermediate d_o values. S_2 occurred over the full range of observed d_o values, with its frequency having no dependence on d_o. D_3 was was only observed for cells with $d_o < 50$.

For circular chambers D_2 is the dominant director field for all cell diameters. For the lowest diameters ($d_o < 10$) N rapidly increases in frequency, and becomes approximately half as frequent as D_2. This is in agreement with the simulations where a transition from D_2 to N is observed with increasing rod length. Increasing rod length for a fixed cell diameter is equivalent to decreasing cell diameter size for a fixed rod length. This suggests that at $d_o \approx 10$ we start to approach the crossover where the anchoring penalty of N becomes of the order of the elastic energy cost for D_2. These observations complement previous work on tactoids and circular confinement, where bipolar (D_2) and uniform (N) director fields are observed [132,133].

The simulations predict the existence of higher order symmetric states for annular geometries. Experimentally, as we increase the inner hole diameter we see D_2 decrease in frequency and we clearly observe the D_3 director field (albeit infrequently) and then observe U. D_3 occurs for values of $d_i/L = 2.5 - 7.5$, which is greater than the $d_i/L = 0.58$ seen for 2D simulations (eq. (6.1)) for three fold symmetry. However, for the simulations with cells of a greater depth, greater d_i/L ratios are observed. We note that the three-fold symmetry of D_3 is of an order that lies between the two-fold symmetry of D_2 and the infinite-fold symmetry of U, indicating that D_3 is a stable intermediate state between D_2 and U. We do not observe the higher symmertic states in the experiments. In the simulations, as the n-fold symmetry of the director fields increases, they become increasingly similar to the observed U director field. We suggest that the confinement is not sufficient to induce these higher order symmetric states, and U is adopted instead; as $d_i \to d_o$ the particles can align with both walls without the need to create a defect. We believe that the difference between d_i and d_o would have to be less than the 4 μm, which was the lowest difference used in these experiments, for the higher symmetry states to be observed.

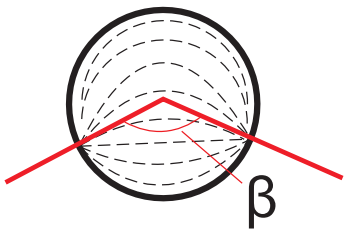

Figure 6.6: Sketch of the the angle β between the two defects in the S_2 director field.

We assume that the S_2 state is a stable intermediate. Possibly, S_2 is a precursor to the D_2 and D_3 profiles. S_2 was seen in the simulations as a precursor to D_3, where the two defects occurred at two vertices of an equilateral triangle. This observation roughly agrees with experiment, where we found a wide distribution of angles β between the defects (illustrated in

figure 6.6), with a mode at 140°. This experimental value is in reasonable agreement with 120° which corresponds to the intermediate state observed in simulations. The other possibility is that S_2 is an intermediate for D_2, intuitively having the defects diametrically opposite will be lower in energy than bringing them closer together. Parallel arguments hold for S_1 which could be an intermediate for both D_2 and D_3 (and also S_2). S_1 is frequently observed implying it is not significantly higher in energy than D_2. The energy difference between these two director fields is the difference between a bend and a $+1 \times \frac{1}{2}$ defect.

6.5 Conclusion

We have shown for the first time the director fields that are observed in annular cells. We have observed striking structures with three fold symmetry. For circular cells we have observed the expected bipolar and uniform director fields giving us confidence in our results. Our experimental observations are in agreement with Monte Carlo simulation and indicate that we have reached a level of confinement where theoretically the rod length needs to be taken into account. Future theoretical work, that could obtain expressions for the energies of the director fields, would enable us to obtain values for the ratios of the elastic constants and anchoring penalty.

Acknowledgments

This work was a collaboration with Gijsje Koenderink's and Bela Mulder's groups at the AMOLF. The experiments were undertaken with José Alvarado, supervised by Gijsje Koenderink. The simulations were performed by Ioana C. Garlea and Pieter Mulder supervised by Bela M. Mulder.

Chapter 7

A study of the *fd* virus' isotropic nematic interface in bulk and confinement

Abstract

We investigate the isotropic-nematic interface of the rodlike virus *fd* on the single particle level. Phase separation takes a long time due to tactoids merging slowly with the interface. Phase separation is considerably speeded up by moving from bulk to micrometer sized systems. Across the interface we measure a sudden drop in the order parameter, which is a measure of the width of the interface. We furthermore illustrate the possibilities of studying phase separation and wetting behaviour in the presence of structured walls.

7.1 Introduction

The isotropic nematic (IN) transition of rods was first theoretically explained in a seminal paper by Onsager, with his famous entropy argument [12]. The transition arises from competition between a packing entropy, which is maximised when the rods long axis are parallel and an orientational entropy term which favours the isotropic phase. Onsager theory has been shown to be correct for hard monodisperse rods, with an aspect ratio L/D greater than 100 [136]. Not many experimental systems fulfill these requirements. Consequently the theory has been extended to take into account flexibility [137, 138], polydispersity [139], and a range of aspect ratios [140, 141]. Here we focus on studying the IN interface where its properties depend on the complex interplay of anchoring strength, surface tension, and elasticity [142]. Additionally, there is the potential to observe capillary waves, which have been studied theoretically in IN systems [143, 144].

Detailed theoretical investigations of the IN interface for hard rods have been undertaken using density functional theory (DFT) [143, 145–147]. This work has calculated the interfacial tension and shown that it is minimised when the director is parallel to the interface. Also the DFT calculations have shown that alignment is induced in the isotropic phase adjacent to the interface. Monte Carlo simulations of the IN interface for hard rods revealed results in excellent agreement with DFT, the only difference being that DFT overestimated the bulk coexistence densities [148, 149]. Additionally, Frank elastic and Landau de Gennes continuum theories have been used to study fluctuating IN interfaces [150].

Experimental work lags behind the numerical work, but the IN phase separation has been observed for several colloidal rod and platelet systems using polarization microscopy, with the nematic phase clearly identifiable from its birefringence [50, 61, 151–153]. Additionally, light scattering methods have enabled the IN interface to be studied for thermotropic liquid crystals, enabling the anchoring energy [154] and surface tension [155] to be measured. Here we use lyotropic rather than thermotropic liquid crystals as the greater particle size enables observation at the single particle level. The capillary rise of the IN interface has been observed for gibbsite platelets enabling the interfacial tension to be measured [153]. The interfacial tension has also been measured by studying the director fields of gibbsite tactoids and was found to be two orders of magnitude greater [156]. Currently there is no explanation for this difference.

We will use the *fd* virus with its dimensions enabling single particle observation. The *fd* virus' IN phase behavior has been studied and the phase diagram has been produced as a function of ionic strength and polymer concentration [157]. Interestingly, for certain high polymer concentrations an isotropic smectic transition occurs [158]. The kinetics of *fd*'s IN phase separation have also been studied, using shear flow to stabilise the nematic phase of an initially biphasic sample [159–161]. The sample concentration determined the phase separation kinetics occuring after the shear flow was stopped, enabling the spinodal points to be determined and the morphology of phase separation to be studied.

In this work we study the IN interface at the particle level. The chapter is organised as follows; we begin by outlining Onsager theory (section 7.2), and then briefly describe the experimental set-up (section 7.3). We then present and discuss the IN interface in bulk and confinement (section 7.4), before concluding (section 7.5).

7.2 Theoretical background: Onsager theory

Here we sketch out Onsager theory for the IN transition of lyotropic hard rods, highlighting the important equations and arguments[1]. We start by obtaining an equation for the free energy of anisotropic particles, that applies to both the isotropic and nematic phases. We then show the steps to obtain the isotropic nematic coexistence concentrations. Throughout we explain the approximations and validity of Onsager theory.

We start with the Helmholtz free energy virial expansion for a non-ideal solution of spheres:

$$\frac{F}{NkT} = \mu_0\beta + \ln(\rho\Lambda^3) - 1 + B_2\rho + \frac{1}{2}B_3\rho^2 + ... \tag{7.1}$$

Here, F is the Helmholtz free energy, T the temperature, ρ the number density, μ_0 the reference chemical potential of the solute, N the number of moles, $\Lambda = \frac{h}{\sqrt{2\pi mkT}}$ the de Broglie thermal wavelength, and B_2 and B_3 the second and third virial coefficients respectively. The virial coefficients depend on the pairwise interaction energies between particles, and take non-ideality into account. The virial coefficients are related to the pairwise interaction energies, u_{ij}, via

[1] For an indepth derivation the reader is referred to [162].

the Mayer functions: $\phi_{ij} = \exp(-u_{ij}\beta) - 1$ [163]. The second virial coefficient depends on the interactions between pairs of particles and reads:

$$B_2 = -\frac{1}{2V}\int\int \phi_{ij} dr_1 dr_2. \tag{7.2}$$

We now switch the focus to rods. The difference between rods and spheres is that the orientation must be taken into account. An orientation distribution function, $f(\Omega)$, is defined, which gives the probability of finding a rod with an orientation characterized by a solid angle Ω. This distribution function must be normalized, $\int f(\Omega)d\Omega = 1$, and adhere to the symmetry properties of the nematic phase; cylindrical symmetry around the nematic director ($f(\Omega)$ does not depend on the azimuthal angle) and inversion symmetry (θ and $\theta - \pi$ are equivalent). In the isotropic phase all orientations are equally probable, $f_{iso}(\Omega) = 1/(4\pi)$. In the nematic phase, this is not the case and there is a corresponding entropy term, which is derived by considering particles with different orientations, as belonging to different species:

$$S_m = -Nk\int f(\Omega)\ln(4\pi f(\Omega))d\Omega. \tag{7.3}$$

Additionally, as the particle interactions depend on the particle orientations, the virial coefficients include the orientation distribution functions:

$$B_2 = -\frac{1}{2}\int\int\int \phi f(\Omega_1) f(\Omega_2) d\Omega_1 d\Omega_2 dr_{12}. \tag{7.4}$$

Equation (7.4) can be simplified with the integral of the Mayer function equaling the excluded volume of two rods: $\int \phi dr_{12} = -v_{excl}(\Omega_1, \Omega_2)$. Assuming the rods are cylinders, $v_{excl} \approx 2L^2 D \mid \sin\gamma \mid$, and eq. (7.4) now reads:

$$B_2 = L^2 D\int\int \mid \sin\gamma \mid f(\Omega_1) f(\Omega_2) d\Omega_1 d\Omega_2. \tag{7.5}$$

Defining the concentration of rods as $c = \frac{\pi}{4}L^2 D\frac{N}{V}$, and combining eqn's (7.1), (7.3), and (7.4)

enables us to write the Helmholtz free energy as:

$$\frac{F}{NkT} = \mu_0 kT + \ln(\rho\Lambda^3) - 1 + \int f(\Omega)\ln(4\pi f(\Omega))d\Omega + c\frac{4}{\pi}\int\int \mid \sin\gamma \mid f(\Omega_1)f(\Omega_2)d\Omega_1 d\Omega_2. \tag{7.6}$$

The first integral takes into account the orientational entropy, which is maximized when the rods are randomly distributed. The second integral takes the packing entropy into account, which is maximized when the individual rods have as much space as possible to move in. At low concentrations the orientational entropy is dominant and an isotropic phase forms, but at a certain concentration the packing entropy becomes dominant and the entropy is maximized by a nematic phase forming. The contribution of the particle interactions to the free energy is driving the system towards a nematic phase.

In eq. (7.6) we have only included the second virial coefficient neglecting collisions involving three or more rods. Intuitively this approximation will become less accurate as the rod concentration increases and multi-rod collisions get increasingly likely. The approximation only holds if the virial series is rapidly convergent. It has been verified analytically that eq. (7.6) is exact for $L/D \to \infty$ [164], and Monte Carlo simulations show it is quantitatively accurate for $L/D > 100$ [165].

For each concentration the system needs to be at a minimum of the Helmholtz free energy. At certain concentrations the minimum is obtained by a state which is part isotropic and part nematic, the so called biphasic/coexistence region. The aim is to find this region. There are two possible methods: eq. (7.6) can be minimized and solved numerically, or a trial function can be used and eq. (7.6) is solved by a variational method. The first method produces the most accurate results, but the second method gives an analytic expression for the free energy. Here we shall use a Gaussian distribution trial function, which was first suggested by Odijk [166] [2]:

$$\begin{aligned} f(\theta) &= N\exp(-\frac{1}{2}\alpha\theta^2) && 0 \le \theta \le \pi/2 \\ &= N\exp(-\frac{1}{2}\alpha(\pi-\theta)^2) && \pi/2 \le \theta \le \pi, \end{aligned} \tag{7.7}$$

with N being the normalization constant. For large α the distribution is strongly peaked and

[2] Onsager used the trial function: $f(\theta) = \frac{\alpha\cosh(\alpha\cos\theta)}{4\pi\sinh\alpha}$, which works equally well, however, the integrals are more involved.

represents strongly ordered nematics. Using eq. (7.7) the energy, eq. (7.6) can be expressed in terms of α:

$$\frac{F}{NkT} \approx constant + \ln\alpha + \frac{4c}{\sqrt{\pi\alpha}}. \tag{7.8}$$

Minimizing this expression with respect to α is simple and yields: $\alpha = \frac{4c^2}{\pi}$. The order parameter of the nematic phase can be calculated using the usual relation:

$$q = \frac{1}{2}\int f(\theta)(3\cos^2\theta - 1)\sin\theta d\theta \sim 1 - \frac{3}{\alpha}. \tag{7.9}$$

Finally, by equating the chemical potentials and pressures of the isotropic and nematic phase a first order IN transition is shown, with the following isotropic and nematic volume fractions at coexistence:

$$\Phi_i\frac{L}{D} = 3.45 \qquad q_i = 0 \qquad \Phi_n\frac{L}{D} = 5.12 \qquad q_n = 0.910. \tag{7.10}$$

Recently the Y21M virus, a rigid rod with an aspect ratio of $\sim$ 133, was shown to have IN coexistence concentrations in agreement with Onsager theory [62]. It is the first experimental system to be in quantitative agreement with Onsager theory, with all other systems deviating due to polydispersity, aspect ratio and/or flexibility.

7.3 Experimental set-up

We used the *fd* virus, synthesised as described in chapter 2. The virus stock solution was prepared in the biphasic region, for which we found crossed polarizers to be the most efficient method (as opposed to UV-vis spectroscopy). Using crossed polarizers we diluted a nematic sample dropwise until the birefringence disappeared and the sample was isotropic. The sample was then brought into the biphasic region by adding a drop of concentrated nematic.

Two sample holders were used: (1) L-shaped cuvettes, and (2) rectangular UV channels with a width = 65μm and a height = 55μm (fabricated as described in chapter 2). The sample holders contained volumes of order cm^3, and μm^3, respectively. This enabled us to observe phase separation in bulk and in confinement.

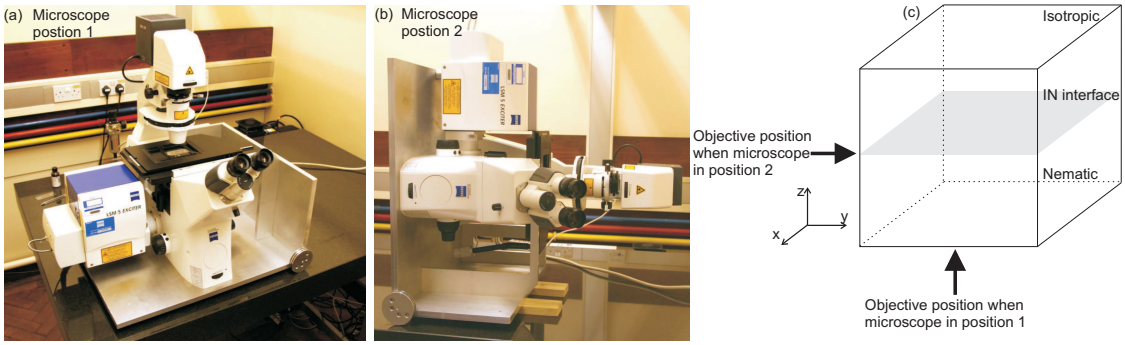

Figure 7.1: Home built confocal microscope set-up. (a) Microscope in the horizontal (conventional) position. (b) Microscope rotated onto its side. (c) Objective position relative to the sample for the two microscope positions.

Imaging of the labeled particles was carried out with a laser scanning confocal microscope (LSCM): Zeiss LSM 5 Exciter, 63x 1.4 NA oil-immersion objective. We were able to rotate the microscope onto its side, creating two objective positions relative to the sample, and enabling observation of the xz and xy planes, as shown in figure 7.1.

7.4 Results and discussion

Bulk phase separation in L-shaped cuvettes. After two days a flat interface would be observed by eye when the sample was viewed between crossed polarisers, as shown in figure 7.2(a). After 11 months (!) an interface on the single rod level could be observed. Figures 7.2(b) and (c) show a LSCM image of the interface (xz plane), and a colour map analysis of 350 images: we clearly observe a nematic and an isotropic phase. However, the interface is not flat and the rods in the nematic phase are not aligned parallel to the interface as we would expect from theory and simulations [143, 146]. This indicates that the IN interface is not fully equilibrated. To quantify these observations, we selected nine regions, 20 μm wide, where the interface was flat and measured the order parameter q in rectangular segments across the xz plane (illustrated in figure 7.2(e)). The rectangles were 10 μm high, and the minimum number of rods in a rectangle was 75 rods, giving accurate statistics. Interestingly, we observed the number of labeled rods decrease as we moved from the nematic phase across the interface to the isotropic phase. This is expected due to the density difference between the phases. Figure 7.2(d) shows a typical plot of order parameter q against the z position in the sample, where we observe a drop in q from 0.75 to 0.2. We would expect $q = 0$ for the isotropic phase. Possibly, the interface induces some order in the isotropic phase, this is seen in the simulations albeit to a lesser extent [143].

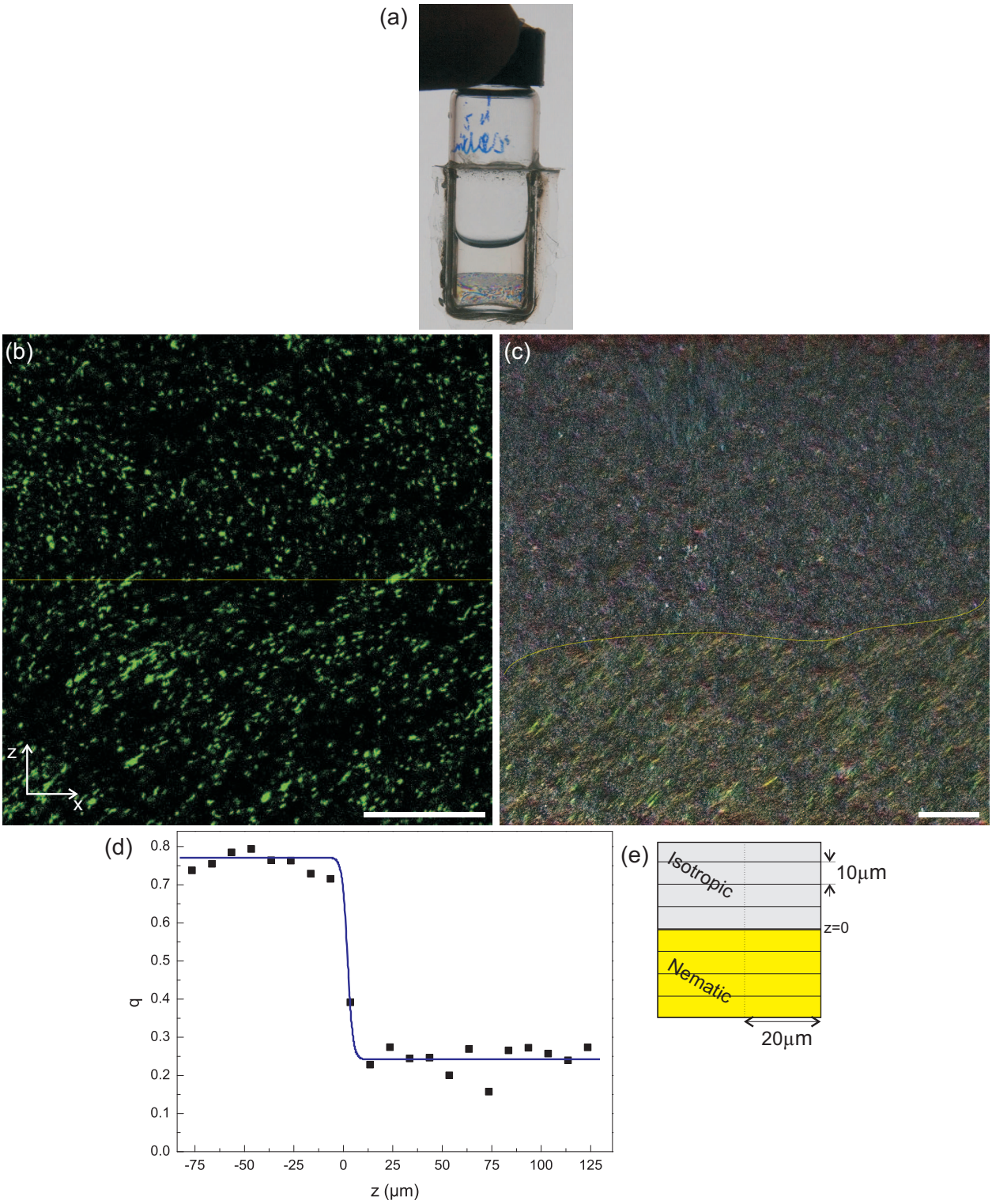

Figure 7.2: (a) Photograph of an L-shaped cuvette between crossed polarisers. The IN interface is clearly observed due to the nematic phase's birefringence. (b) Microscope image of the IN interface, obtained by overlaying 4 LSCM images. (c) A colour map of the series of 350 LSCM images corresponding to the image in (b). The yellow dotted line highlights the IN interface. Scale bar = 25 μm, in both (b) and (c). (d) Plot of order parameter q versus z position in the sample, for one of the nine selected flat regions of the interface. (e) This panel illustrates how the order parameter was measured across the interface, by dividing the image up into rectangles.

Another explanation is that our tracking routine is for rods, but in the isotropic phase the rods appear as circles or as rods with a range of aspect ratios. The tracking was thus not perfect for the isotropic phase and may have induced some spurious ordering.

The width of the interface, w_{in}, was obtained by fitting the following hyperbolic tangent expression:

$$q(z) = A + B \tanh\left(\frac{z}{w_{in}}\right), \tag{7.11}$$

where A and B are constants. This expression has been used frequently in theory and simulation to describe the profile of the interface [143, 148], and it follows from the van der Waals theory for the density profile of a gas liquid interface [167, 168]. From the hyperbolic tangent fits of the nine regions we find the width of the interface to be, $w_{in} = 2.6 \pm 2.8$ μm. This value is equivalent to two rod lengths, in agreement with the upper bound of the numerical work which finds the width w_{in} to be in the range of 0.5 - 3 rod lengths [143, 146, 148].

We suggest that the very long phase separation times occur because nematic tactoids get stuck at the interface [124]. The final stages of phase separation involve nematic tactoids sinking from the isotropic phase to the interface and isotropic tactoids rising to the interface from the nematic phase. We observe that if the director of a nematic tactoid differs to the director of the interface, the tactoid will not be able to merge with the interface. The tactoid must either rotate and/or reorganise its director field. It is reasonable to assume that tactoids in the isotropic phase will not have a preferred orientation, thus it is probable that a significant number of tactoids will land on the interface with a director that differs to the interface [3]. We believe that the long reorganisation times of these tactoids is the reason for long interface equilibration times on the single particle level. One way to test this idea would be to use a magnetic field to align the nematic phase and tactoids. We were prevented from doing this as substantial magnetic fields are required to align the nematic phase [169, 170]. Realistically this would involve a custom set-up of a confocal microscope inside a magnet.

Phase separation times of 11+ months were a significant experimental obstacle. To avoid this we moved to lower sample volumes to decrease phase separation times. Additionally to

[3] We note, that we have not assumed a certain director field for the tactoids. Previously bipolar tactoids have been observed for *fd* [61] and TMV [53], but a detailed analysis of how the director field changes with the tactoid size and shape has not been carried out, as it has been done for gibbsite platelets [83, 124].

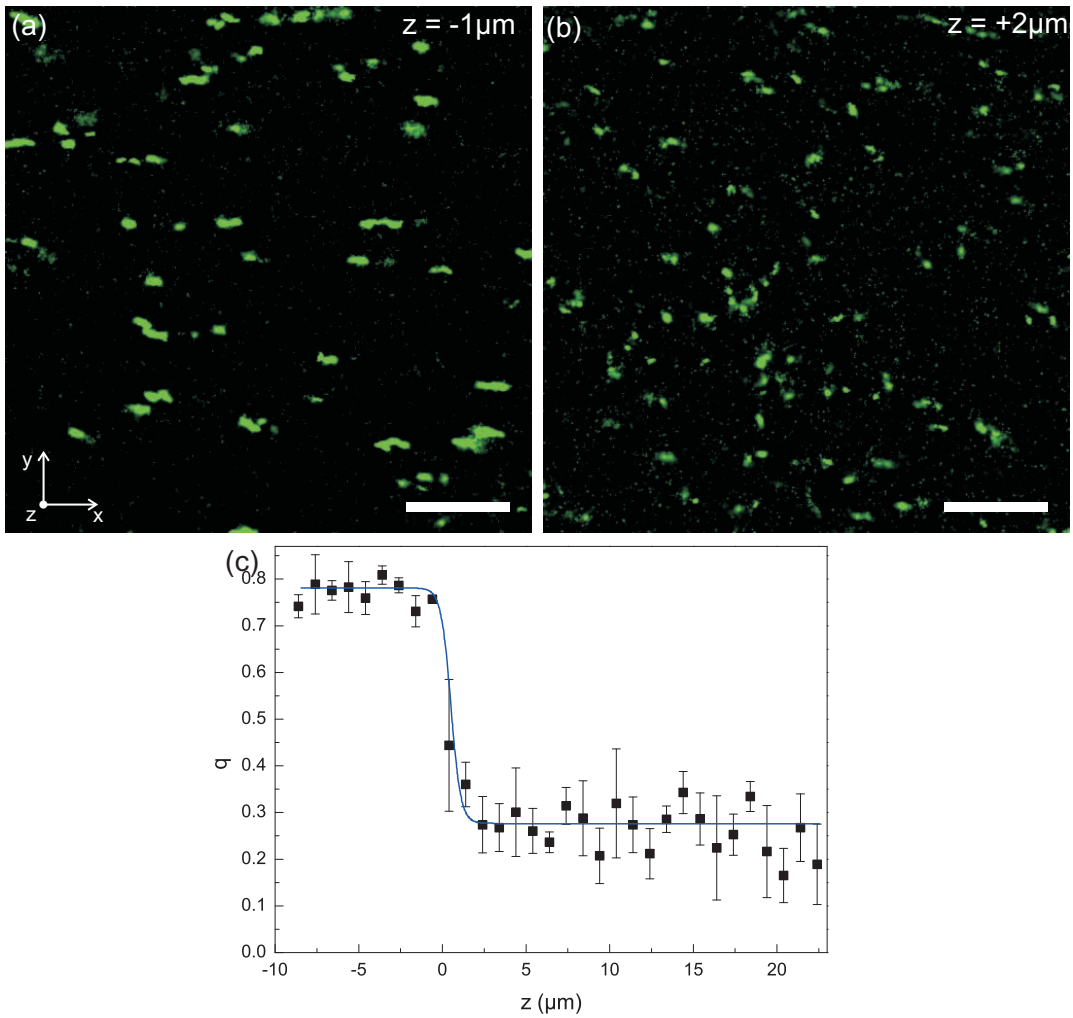

Figure 7.3: (a) and (b) LSCM microscope images of the nematic and isotropic phase respectively. Scale bar = 5 μm. (c) Plot of order parameter q versus z position.

decrease phase separation times further, we moved the concentration of *fd* to the isotropic edge of the biphasic region; after the biphasic *fd* stock had phase separated, part of the nematic phase would be removed to create a 1:10 ratio of nematic to isotropic. The argument is that, the lower the volume of nematic phase, the lower the number of tactoids getting stuck at the interface.

Phase separation in confinement. Phase separation occurred in 6 hours. We used the microscope in the horizontal position and observed the xy plane. This has the disadvantage of not being able to observe the IN interface in one microscope image (the xz or yz plane), but the advantage of giving more statistics of the ordering at the interface. By moving the focus of the microscope along the z-axis we observed a nematic and then an isotropic phase, see figure 7.3(a) and (b). We observed parallel anchoring of the nematic phase at the interface, as expected from theoretical work where the interfacial tension is minimised by parallel anchoring. To quantify the interface,

the order parameter q was calculated at 1 μm steps along the z-axis. In figure 7.3(c) we plot q versus z position in the sample and observe a similar drop in q to figure 7.2(c). From fitting the hyperbolic tangent function (eq. (7.11)) we measure an interface width of $w_{in} = 0.85$ μm. This is smaller than the previous measurement, which is expected as the system has now fully phase separated. Additionally, it is one rod length which as stated earlier is what one expects from the theory.

7.5 Conclusion and outlook

We have observed isotropic-nematic phase separation at the level of the individual rods in bulk and confined micrometer sized systems. The long phase separation times makes the *fd* virus a tough system to work with. In confinement the shorter phase separation times have enabled us to measure the width of the IN interface for the first time, and observe planar anchoring at the interface, in agreement with the theoretical work.

Finally, as an outlook in figure 7.4 we present preliminary experiments of biphasic *fd* samples in channels where the top confining wall is structured with triangles, rectangles, or sinusoidal waves. In figure 7.4(a) for a sinusoidal top wall we observe phase separation with an additional nematic layer at the top of the channel. In figure 7.4(b) for a square structured top wall we observe phase separation with no additional nematic layer. In figures 7.4(c) and (d) the channels are filled with a concentration at the nematic border of the biphasic region and a nematic phase is induced. Currently, we do not have an explanation for these observations, but clearly there is an interplay between phase behaviour, elasticity and confinement. Recent numerical work has modeled nematic liquid crystals at very similar 'complicate surfaces' using a Landau de Gennes framework [90, 91, 171].

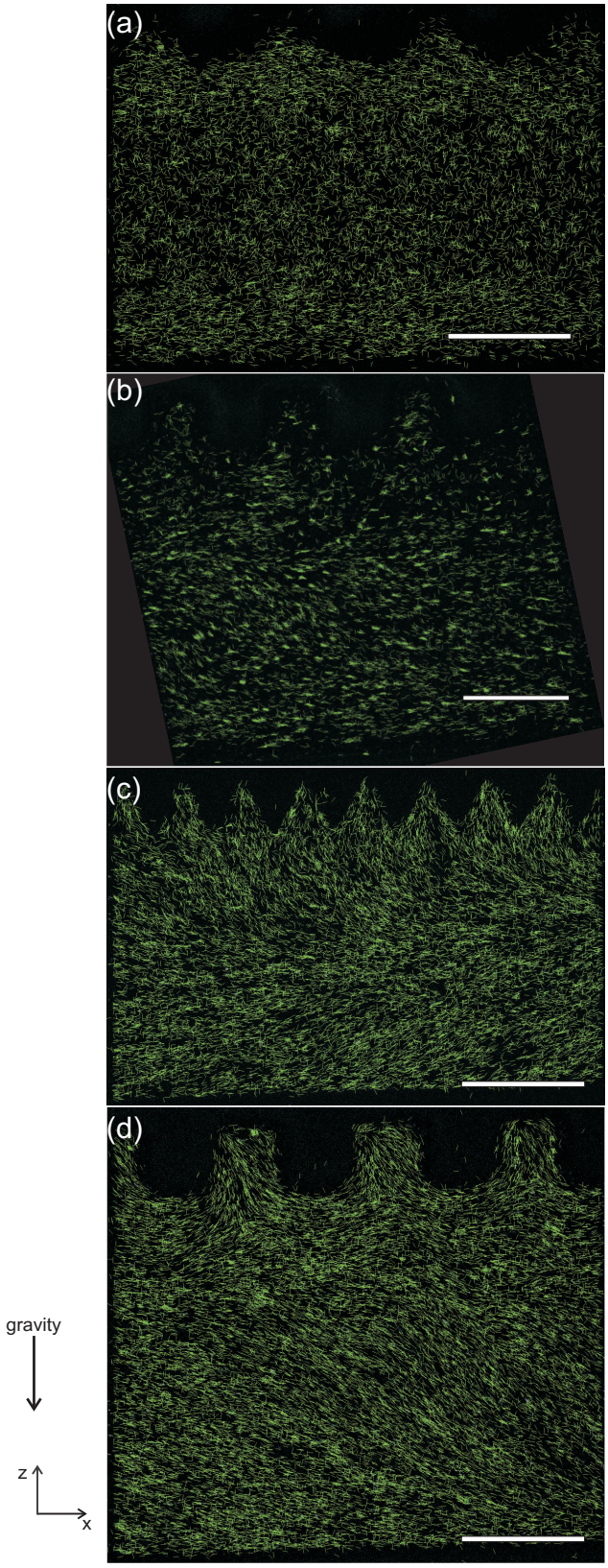

Figure 7.4: Analysed microscope images of biphasic *fd* in channels with a structured top wall. The rods in the original microscope images have been identified using IDL and lines haven been overlaid to increase the clarity of the images. (a) Sinusoidal top wall, phase separation is observed and a nematic layer is induced at the top. (b) Square structured top wall, phase separation is observed. (c) Triangular structured top wall, phase separation is suppressed and a nematic is observed. (d) Square structured top wall, phase separation is suppressed and a nematic is observed. Scale bar = 50 μm.

Summary

This thesis is on colloidal liquid crystals. Specifically, we have focused on examining the equilibrium director fields of the *fd* virus, in confined geometries, in order to study the relationships between confinement, elasticity and anchoring. Chapter 1 gives an introduction to liquid crystals and explains why we chose the *fd* virus as our model system. Soft lithography can fabricate structures on the micrometer scale, and laser scanning confocal microscopy enables observation on the micrometer scale. These powerful techniques are discussed in chapter 2.

In chapter 3 we study the nematic phase of *fd* confined to wedge structured channels. Upon increasing wedge opening angle we observe a splay to bend transition. We use two variants of the *fd* virus with different flexibilities, with the transition shifting to a greater wedge opening angle for the stiffer variant. Our results are interpreted using lattice Boltzmann simulations enabling the K_3/K_1 ratios to be determined. This chapter illustrates that the director field can be engineered using geometry: a reoccurring result of this thesis. Chapter 4 continues the theme of wedge structured confinement, extending the study to the cholesteric phase. Upon increasing wedge angle a splay to twist transition is observed, accompanied by a splay-twist boundary. We directly visualise the 3D nature of the problem, and explain how the transition arises due to competition between the anchoring strength and all three of the elastic terms: splay, bend, and twist.

Chapter 5 deals with the nematic phase confined to 2D rectangular cells. Five distinct director fields are observed, whose frequency varies with the rectangle aspect ratio. Changing the virus flexibility is found not to have a significant effect on the observed director fields, and their frequency. Comparing the frequencies to computations of the Frank-Oseen energies enables a measurement of the extrapolation length, which we find to be of the order of the rod length.

Liquid crystal continuum theories do not take into account the particle size. In chapter 6

we address this issue, by examining the director fields in circular and annular geometries, whose dimensions approach the particle size. For circular geometries, we measure a transition from a bipolar to a uniform director field, upon decreasing radius. For annular geometries, as we increase the diameter of the inner hole, we measure a transition from a bipolar to a bent rotationally symmetric director field, via a range of director fields. These results are in qualitative agreement with Monte Carlo simulations of finite sized rods. We hope that the current work wil inspire the development of theories which can capture these director fields.

Chapter 7 is an exploratory chapter in which we observe the isotropic-nematic interface. In bulk, long phase separation times occur due to tactoids merging slowly with the interface. Decreased phase separation times occur in confinement with sample volumes on the micrometer scale. We observe parallel anchoring at the interface, and measure the width of the interface to be of the order of the rod length. As hinted to in chapter 7, we would like to investigate phase separation at structured walls. This extends the work in this thesis by adding phase separation to the interplay of confinement, anchoring and elasticity.

Bibliography

[1] P. G. de Gennes and J. Prost. *The Physics of Liquid Crystals (2nd Ed)*. Oxford University Press, 1993.

[2] M. J. Stephen and J. P. Straley. Physics of liquid crystals Liquid Crystals. *Reviews ot Modern Physics*, 46, 1974.

[3] F. C. Bawden, N. M. Pirie, J. D. Bernal, and I. Fankuchen. Liquid Crystalline Substances from Virus infected Plants. *Nature*, 138:1051, 1936.

[4] H. Maeda and Y. Maeda. Liquid Crystal Formation in Suspensions of Hard Rodlike Colloidal Particles: Direct Observation of Particle Arrangement and Self-Ordering Behavior. *Physical Review Letters*, 90:018303, 2003.

[5] I. Langmuir. The Role of Attractive and Repulsive Forces in the Formation of Tactoids, Thixotropic Gels, Protein Crystals and Coacervates. *The Journal of Chemical Physics*, 6:873, 1938.

[6] F. M. van der Kooij, K. Kassapidou, and H. N. W. Lekkerkerker. Liquid crystal phase transitions in suspensions of polydisperse plate-like particles. *Nature*, 406:868, 2000.

[7] D. R. Link, G. Natale, R. Shao, N. A. Clark, E. Korblova, and D.M. Walba. Spontaneous Formation of Macroscopic Chiral Domains in a Fluid Smectic Phase of Achiral Molecules. *Science*, 278:1924, 1997.

[8] L. A. Madsen, T. J. Dingemans, M. Nakata, and E. T. Samulski. Thermotropic Biaxial Nematic Liquid Crystals. *Physical Review Letters*, 92:145505, 2004.

[9] L. J. Yu and A. Saupe. Observation of a biaxial nematic phase in potassium laurate-1-decanol-water mixtures. *Physical Review Letters*, 45:1000, 1980.

[10] C. Tschierske and D. J. Photinos. Biaxial nematic phases. *Journal of Materials Chemistry*, 20:4263, 2010.

[11] S. Chandrasekhar. *Liquid Crystals*. Cambridge University Press, 2nd edition, 1992.

[12] L. Onsager. The effects of shape on the interaction of colloidal particles. *Annals of the New York Academy of Sciences*, 51:627, 1949.

[13] A. Harris, R. Kamien, and T. C. Lubensky. Microscopic Origin of Cholesteric Pitch. *Physical Review Letters*, 78:1476, 1997.

[14] W. D. S. John, W. J. Fritz, Z. J. Lu, and D. K. Yang. Bragg reflection from cholesteric liquid crystals. *Physical Review E*, 51:1191, 1995.

[15] C. Binet, M. Mitov, and A. Boudet. Molecular Crystals and Liquid Crystals Science and Technology . Section A . Molecular Crystals and Liquid Crystals Bragg Reflections In Cholesteric Liquid Crystals : From Selectivity To Broadening And Reciprocally. *Mol. Cryst. Liq. Cryst.*, 339:111, 1999.

[16] P. T. Ireland and T. V. Jones. The response time of a surface thermometer employing encapsulated thermochromic liquid crystals. *J. Phys. E: Sci. Instrum.*, 20:1195, 1987.

[17] N. Boden, R. J. Bushby, J. Clements, and B. Movaghar. Device applications of charge transport in discotic liquid crystals. *Journal of Materials Chemistry*, 9:2081, 1999.

[18] E. Grelet. Hexagonal Order in Crystalline and Columnar Phases of Hard Rods. *Physical Review Letters*, 100:168301, 2008.

[19] A. C. Ribeiro, B. Heinrich, C. Cruz, H. T. Nguyen, S. Diele, M. W. Schröder, and D. Guillon. Rectangular to hexagonal columnar phase transition exhibited by a biforked mesogen. *The European physical journal. E, Soft matter*, 10:143, 2003.

[20] K. Pelz, W. Weissflog, U. Baumeister, and S. Diele. Various columnar phases formed by bent-core mesogens. *Liquid Crystals*, 30:1151, 2003.

[21] D. Chakrabarti and D. Wales. Tilted and Helical Columnar Phases for an Axially Symmetric Discoidal System. *Physical Review Letters*, 100:127801, 2008.

[22] V. Tsvetkov. *Acta Physicochim. (USSR)*, 16:132, 1942.

[23] P. G. de Gennes. Short range order effects in the isotropic phase of nematics and cholesterics. *Molecular Crystals and Liquid Crystals*, 12:193, 1971.

[24] P. Poulin, H. Stark, T. C. Lubensky, and D. A. Weitz. Novel Colloidal Interactions in Anisotropic Fluids. *Science*, 275:1770, 1997.

[25] G. Friedel. *Ann. Phys., Paris*, 19:273, 1922.

[26] C. W. Oseen. The theory of liquid crystals. *Transactions of the Faraday Society*, 29:883, 1933.

[27] F. C. Frank. I. Liquid crystals. On the theory of liquid crystals. *Discuss. Faraday Soc.*, 25:19, 1958.

[28] S. Lee and R. B. Meyer. Computations of the phase equilibrium, elastic constants, and viscosities ofd a hard-rod nematic liquid crystal. *J. Chem. Phys*, 84:3443, 1986.

[29] V. G Taratuta, A. J. Hurd, and R. B. Meyer. Light-Scattering Study of a Polymer Nematic Liquid Crystal. *Physical Review Letters*, 55:246, 1985.

[30] V. G Taratuta, F. Lonberg, and R. B. Meyer. Anisotropic mechanical properties of a polymer nematic liquid crystal. *Physical Review A*, 37:1831, 1988.

[31] Z. Dogic and S. Fraden. Cholesteric Phase in Virus Suspensions. *Langmuir*, 16:7820, 2000.

[32] S. Žumer and S. Kralj. Influence of K 24 on the structure of nematic liquid crystal droplets. *Liquid Crystals*, 12:37, 1992.

[33] P. Prinsen and P. van der Schoot. Shape and director-field transformation of tactoids. *Physical Review E*, 68:021701, 2003.

[34] M. Cestari and A. Ferrarini. Curvature elasticity of nematic liquid crystals: simply a matter of molecular shape? Insights from atomistic modeling. *Soft Matter*, 5:3879, 2009.

[35] G. Barbero. Surface geometry and induced orientation of a nematic liquid crystal. *Lettere al nuovo cimento della societa italiana di fisica*, 29, 1980.

[36] D. W. Berreman and S. Meiboom. Tensor representation of Oseen-Frank strain energy in uniaxial cholesterics. *Physical Review A*, 30:1955, 1984.

[37] D. R. Anderson, D. E. Carlson, and E. Fried. A continuum-mechanical theory for nematic elastomers. *Journal of Elasticity*, 56:33, 1999.

[38] C. Denniston, E. Orlandini, and J. M. Yeomans. Lattice Boltzmann simulations of liquid crystal hydrodynamics. *Physical Review E*, 63:056702, 2001.

[39] A. Saupe. Disclinations and properties of the directorfield in nematic and cholesteric liquid crystals. *Molecular Crystals and Liquid Crystals*, 21, 1973.

[40] M. Ravnik and S. Žumer. Landaude Gennes modelling of nematic liquid crystal colloids. *Liquid Crystals*, 36:1201, 2009.

[41] J.K.G. Dhont. *An Introduction to Dynamics of Colloids*. Elsevier, 1996.

[42] W. B. Russell, D. A. Saville, and W. R. Schowalter. *Colloidal Dispersions*. Cambridge University Press, 1989.

[43] P. Atkins and J. de Paula. *Atkins' Physical Chemsitry*. Oxford University Press, 7th edition, 2002.

[44] A. Einstein. *Ann. Phys.*, 17:549, 1905.

[45] D. G. A. L. Aarts, M. Schmidt, and H. N. W. Lekkerkerker. Direct visual observation of thermal capillary waves. *Science*, 304:847, 2004.

[46] D. G. A. L. Aarts, H. N. W. Lekkerkerker, H. Guo, G. H. Wegdam, and D. Bonn. Hydrodynamics of Droplet Coalescence. *Physical Review Letters*, 95:164503, 2005.

[47] S. Asakura and F. Oosawa. On Interaction between Two Bodies Immersed in a Solution of Macromolecules. *The Journal of Chemical Physics*, 22:1255, 1954.

[48] S. Asakura and F. Oosawa. Interaction between particles suspended in solutions of macromolecules. *J. Pol. Sci*, 33:183, 1958.

[49] P. A. Buining, C. Pathmamanoharan, J. B. H. Jansen, and H. N. W. Lekkerkerker. Preparation of colloidal boehmite needles by hydrothermal treatment of aluminium alkoxide precursors. *J. Am. Ceram. Soc*, 74, 1991.

[50] P. A. Buining and H. N. W. Lekkerkerker. Isotropic-nematic phase separation of a dispersion of organophilic boehmite rods. *J. Phys. Chem.*, 97:11510, 1993.

[51] P. A. Buining, A. P. Philipse, and H. N. W. Lekkerkerker. Phase behavior of aqueous dispersions of colloidal boehmite rods. *Langmuir*, 10:2106, 1994.

[52] A. Kuijk, A. van Blaaderen, and A. Imhof. Synthesis of monodisperse, rodlike silica colloids with tunable aspect ratio. *Journal of the American Chemical Society*, 133:2346, 2011.

[53] J. D. Bernal and I. Fankuchen. X-Ray and Crystallographic Studies of Plant Virus Preparations. III. *The Journal of General Physiology*, 1941.

[54] Z. Dogic and S. Fraden. Ordered phases of filamentous viruses. *Current Opinion in Colloid & Interface Science*, 11:47, 2006.

[55] A. J. Hurd, S. Fraden, F. Lonberg, and R. B. Meyer. Field-induced transient periodic structures in nematic liquid crystals : the splay Frederiks transition. *Journal de Physique*, 46:905, 1985.

[56] D. Baltimore. Expression of animal virus genomes. *Bacteriological reviews*, 35(3):235–41, 1971.

[57] Z. Zhang and E. Grelet. Tuning chirality in the self-assembly of rod-like viruses by chemical surface modifications. *Soft Matter*, 9:1015, 2013.

[58] E. Grelet and S. Fraden. What Is the Origin of Chirality in the Cholesteric Phase of Virus Suspensions? *Physical Review Letters*, 90:168301, 2003.

[59] Z. Dogic and S. Fraden. *in Soft Matter, edited by G. Gompper and M. Schick, Vol 2*, volume Vol 2. Wiley-VCH, Weinhiem, 2006.

[60] J. Torbet and G. Maret. High-field magnetic birefringence study of the structure of rodlike phages Pf1 and fd in solution. *Biopolymers*, 20:2657, 1981.

[61] Z. Dogic and S. Fraden. Development of model colloidal liquid crystals and the kinetics of the isotropic-smectic transition. *Philosophical Transactions of the Royal Society A: Mathematical, Physical and Engineering Sciences*, 359:997, 2001.

[62] E. Barry, D. Beller, and Z. Dogic. A model liquid crystalline system based on rodlike viruses with variable chirality and persistence length. *Soft Matter*, 5:2563, 2009.

[63] H. L. Liang, S. Schymura, P. Rudquist, and J. Lagerwall. Nematic-Smectic Transition under Confinement in Liquid Crystalline Colloidal Shells. *Physical Review Letters*, 106:247801, 2011.

[64] T. Ohzono and J. Fukuda. Zigzag line defects and manipulation of colloids in a nematic liquid crystal in microwrinkle grooves. *Nature communications*, 3:701, 2012.

[65] J. Jeong and M. W. Kim. Confinement-Induced Transition of Topological Defects in Smectic Liquid Crystals: From a Point to a Line and Pearls. *Physical Review Letters*, 108:207802, 2012.

[66] T. Maniatis, E. F. Fritsch, and J. Sambrook. *Molecular Cloning*. Cold Spring Harbor Univ. Press, 1989.

[67] M. P. Lettinga, E. Barry, and Z. Dogic. Self-diffusion of rod-like viruses in the nematic phase. *Europhysics Letters*, 71:692, 2005.

[68] E. Pouget, E. Grelet, and M. P. Lettinga. Dynamics in the smectic phase of stiff viral rods. *Physical Review E*, 84:020702, 2011.

[69] H. H. Wensink and G. J. Vroege. Isotropic-nematic phase behavior of length polydisperse hard rods. *J. Chem. Phys*, 119:6868, 2003.

[70] G. M. Whitesides. The origins and the future of microfluidics. *Nature*, 442:368, 2006.

[71] S. Nagrath, L. V. Sequist, S. Maheswaran, D. W. Bell, D. Irimia, L. Ulkus, M. R. Smith, E. L. Kwak, S. Digumarthy, A. Muzikansky, P. Ryan, U. J. Balis, R. G. Tompkins, D. A. Haber, and M. Toner. Isolation of rare circulating tumour cells in cancer patients by microchip technology. *Nature*, 450:1235, 2007.

[72] M. Soares e Silva, J. Alvarado, J. Nguyen, N. Georgoulia, B. M. Mulder, and G. H. Koenderink. Self-organized patterns of actin filaments in cell-sized confinement. *Soft Matter*, 7:10631, 2011.

[73] D. Bartolo and D. G. A. L. Aarts. Microfluidics and soft matter: small is useful. *Soft Matter*, 8:10530, 2012.

[74] P. S. Dittrich and A. Manz. Lab-on-a-chip: microfluidics in drug discovery. *Nature reviews. Drug discovery*, 5:210, 2006.

[75] A. D. Campo and C. Greiner. SU-8: a photoresist for high-aspect-ratio and 3D submicron lithography. *Journal of Micromechanics and Microengineering*, 17:81, 2007.

[76] D. C. Duffy, J. C. Mcdonald, O. J. A. Schueller, and G. M. Whitesides. Rapid Prototyping of Microfluidic Systems in Poly (dimethylsiloxane). *Anal. Chem.*, 70:4974, 1998.

[77] D. Bartolo, G. Degré, P. Nghe, and V. Studer. Microfluidic stickers. *Lab on a chip*, 8:274, 2008.

[78] M. Minsky. Memoir on Inventing the Confocal Scanning Microscope. *Scanning*, 10:128, 1988.

[79] M. Bruchez Jr. Semiconductor Nanocrystals as Fluorescent Biological Labels. *Science*, 281:2013, 1998.

[80] R. H. Webb. Confocal optical microscopy. *Rep. Prog. Phys.*, 59:427, 1996.

[81] T. Wilson. *Confocal Microscopy*. Academic Press Limited, London, 1990.

[82] R. P. A. Dullens. *Structure and dynamics of colloidal hard spheres in real space*. PhD thesis, 2005.

[83] A. A. Verhoeff. *Liquid crystal drops in suspensions of colloidal plates*. PhD thesis, 2011.

[84] J. C. Crocker and D. G. Grier. Methods of Digital Video Microscopy for Colloidal Studies. *Journal of Colloid and Interface Science*, 310:298, 1996.

[85] O. Medalia, I. Weber, A. S. Frangakis, D. Nicastro, G. Gerisch, and W. Baumeister. Macromolecular architecture in eukaryotic cells visualized by cryoelectron tomography. *Science*, 298:1209, 2002.

[86] W. J. Chung, J. W. Oh, K. Kwak, B. Y. Lee, J. Meyer, E. Wang, A. Hexemer, and S. W. Lee. Biomimetic self-templating supramolecular structures. *Nature*, 478:364, 2011.

[87] T. Gibaud, E. Barry, M. J. Zakhary, M. Henglin, A. Ward, Y. Yang, C. Berciu, R. Oldenbourg, M. F. Hagan, D. Nicastro, R. B. Meyer, and Z. Dogic. Reconfigurable self-assembly through chiral control of interfacial tension. *Nature*, 481:348, 2012.

[88] A. J. Davidson, C. V. Brown, N. J. Mottram, S. Ladak, and C. R. Evans. Defect trajectories and domain-wall loop dynamics during two-frequency switching in a bistable azimuthal nematic device. *Physical Review E*, 81:051712, 2010.

[89] A. Majumdar, C. J. P. Newton, J. M. Robbins, and M. Zyskin. Topology and bistability in liquid crystal devices. *Physical Review E*, 75:051703, 2007.

[90] J. Romero-Enrique, C. T. Pham, and P. Patrício. Scaling of the elastic contribution to the surface free energy of a nematic liquid crystal on a sawtoothed substrate. *Physical Review E*, 82:011707, 2010.

[91] P. Patrício, J. Romero-Enrique, N.M. Silvestre, N.R. Bernardino, and M.M. Telo da Gama. Complex fluids at complex surfaces: simply complicated? *Molecular Physics*, 109:1067, 2011.

[92] R. B. Meyer and S. D. Lee. Crossover Behavior of the Elastic Coefficients and Viscosities of a Polymer Nematic Liquid Crystal. *Physical Review Letters*, 61:2217, 1988.

[93] R. Schlinzinger and P. A. A. Laura. *Conformal Mapping: Methods and Applications*. Dover, 1991.

[94] G. Barbero. On the critical angle of a nematic liquid crystal cell. *Lettere al nuovo cimento della societa italiana di fisica*, 32, 1981.

[95] A. J. Davidson and N. J. Mottram. Conformal mapping techniques for the modelling of liquid crystal devices. *European Journal of Applied Mathematics*, 23:99, 2011.

[96] P. Wägli, A. Homsy, and N. F. de Rooij. Norland optical adhesive (NOA81) microchannels with adjustable wetting behavior and high chemical resistance against a range of mid-infrared-transparent organic solvents. *Sensors and Actuators B: Chemical*, 156:994, 2011.

[97] M. P. Lettinga, Z. Dogic, H. Wang, and J. Vermant. Flow behavior of colloidal rodlike viruses in the nematic phase. *Langmuir*, 21:8048, 2005.

[98] I. Zacharoudiou. *Viscous Fingering and Liquid Crystals in Confinement*. PhD thesis, 2012.

[99] A. N. Beris and B. J. Edwards. *Thermodynamics of Flowing Systems: with Internal Microstructure*. Oxford Engineering Science Series, 1994.

[100] M. Doi and S. F. Edwards. *The Theory of Polymer Dynamics*. Oxford University Press, 1986.

[101] K. Schiele and S. Trimper. On the Elastic Constants of a Nematic Liquid Crystal. *Phys. stat. sol.(b)*, 118:227, 1983.

[102] C. Uche, S. J. Elston, and L. A. Parry Jones. Microscopic observation of zenithal bistable switching in nematic devices with different surface relief structures. *Journal of Physics D: Applied Physics*, 38:2283, 2005.

[103] R. H. J. Otten and P. van der Schoot. Private communication, 2010.

[104] L. Pasteur. *Ann. Chim. Phys*, 24, 1848.

[105] H. H. Wensink and G. Jackson. Cholesteric order in systems of helical Yukawa rods. *Journal of physics. Condensed matter : an Institute of Physics journal*, 23:194107, 2011.

[106] D. J. Broer, J. Lub, and G. N. Mol. Wide-band reflective polarizers from cholesteric polymer networks with a pitch gradient. *Nature*, 378, 1995.

[107] P. Kumar, SW Kang, and SH Lee. Advanced bistable cholesteric light shutter with dual frequency nematic liquid crystal. *Optical Materials Express*, 2:1453, 2012.

[108] K. Chari, C. M. Rankin, D. M. Johnson, T. N. Blanton, and R. G. Capurso. Single-substrate cholesteric liquid crystal displays by colloidal self-assembly. *Applied Physics Letters*, 88:043502, 2006.

[109] J. P. Straley. Theory of piezoelectricity in nematic liquid crystals, and of the cholesteric ordering. *Physical Review A*, 14:1835, 1976.

[110] F. Tombolato, A. Ferrarini, and E. Grelet. Chiral Nematic Phase of Suspensions of Rodlike Viruses: Left-Handed Phase Helicity from a Right-Handed Molecular Helix. *Physical Review Letters*, 96:258302, 2006.

[111] S. Tomar, M. M. Green, and L. A. Day. DNA-protein interactions as the source of large-length-scale chirality evident in the liquid crystal behavior of filamentous bacteriophages. *Journal of the American Chemical Society*, 129:3367, 2007.

[112] Z. Dogic and S. Fraden. Smectic Phase in a Colloidal Suspension of Semiflexible Virus Particles. *Physical Review Letters*, 78:2417, 1997.

[113] P. J. Collings and M. Hird. *Introduction to Liquid Crystals*. Taylor & Francis, 1997.

[114] N. A. Clark and S. T. Lagerwall. Submicrosecond bistable electro-optic switching in liquid crystals. *Applied Physics Letters*, 36:899, 1980.

[115] D. W. Berreman. New bistable liquid-crystal twist cell. *Journal of Applied Physics*, 52:3032, 1981.

[116] B. W. Lee and N. A. Clark. Alignment of liquid crystals with patterned isotropic surfaces. *Science*, 291:2576, 2001.

[117] J. H. Kim, M. Yoneya, and H. Yokoyama. Tristable nematic liquid-crystal device using micropatterned surface alignment. *Nature*, 14:159, 2002.

[118] S. Kitson and A. Geisow. Controllable alignment of nematic liquid crystals around microscopic posts: Stabilization of multiple states. *Applied Physics Letters*, 80:3635, 2002.

[119] C. Tsakonas, A. J. Davidson, C. V. Brown, and N. J. Mottram. Multistable alignment states in nematic liquid crystal filled wells. *Applied Physics Letters*, 90:111913, 2007.

[120] Y. Yi, M. Nakata, A. R. Martin, and N. A. Clark. Alignment of liquid crystals by topographically patterned polymer films prepared by nanoimprint lithography. *Applied Physics Letters*, 90:163510, 2007.

[121] C. Luo, A. Majumdar, and R. Erban. Multistability in planar liquid crystal wells. *Physical Review E*, 85:061702, 2012.

[122] A. Lewis. Defects in liquid crystals mathematical and experimental studies (DPhil, Transfer of status thesis). Technical report, 2012.

[123] O. D. Lavrentovich. Topological defects in dispersed words and worlds around liquid crystals, or liquid crystal drops. *Liquid crystals*, 24, 1998.

[124] A. A. Verhoeff, I. A. Bakelaar, R. H. J. Otten, P. van der Schoot, and H. N. W. Lekkerkerker. Tactoids of plate-like particles: size, shape, and director field. *Langmuir*, 27:116, 2011.

[125] T. Govindaraju, P. J. Bertics, R. T. Raines, and N. L. Abbott. Using measurements of anchoring energies of liquid crystals on surfaces to quantify proteins captured by immobilized ligands. *Journal of the American Chemical Society*, 129:11223, 2007.

[126] A. Marino, V. Tkachenko, E. Santamato, N. Bennis, X. Quintana, J. M. Oton, and G. Abbate. Measuring liquid crystal anchoring energy strength by spectroscopic ellipsometry. *Journal of Applied Physics*, 107:073109, 2010.

[127] A. Majumdar and A. Zarnescu. LandauDe Gennes theory of nematic liquid crystals: The OseenFrank limit and beyond. *Archive for rational mechanics and analysis*, 196:227, 2010.

[128] L. Bocquet and E. Charlaix. Nanofluidics, from bulk to interfaces. *Chemical Society reviews*, 39:1073, 2010.

[129] K. S. Han, S. H. Hong, K. I. Kim, J. Y. Cho, K. W. Choi, and H. Lee. Fabrication of 3D nano-structures using reverse imprint lithography. *Nanotechnology*, 24:045304, 2013.

[130] H. Löwen. Twenty years of confined colloids: from confinement-induced freezing to giant breathing. *Journal of physics. Condensed matter : an Institute of Physics journal*, 21:474203, 2009.

[131] T. O. E. Skinner, D. G. A. L. Aarts, and R. P. A. Dullens. Grain-Boundary Fluctuations in Two-Dimensional Colloidal Crystals. *Physical Review Letters*, 105:168301, 2010.

[132] J. Galanis, R. Nossal, W. Losert, and D. Harries. Nematic Order in Small Systems: Measuring the Elastic and Wall-Anchoring Constants in Vibrofluidized Granular Rods. *Physical Review Letters*, 105:168001, 2010.

[133] N. Puech, E. Grelet, P. Poulin, C. Blanc, and P. van der Schoot. Nematic droplets in aqueous dispersions of carbon nanotubes. *Physical Review E*, 82:020702, 2010.

[134] N. Metropolis and S. Ulam. The monte carlo method. *Journal of the American statistical association*, 44:335, 1949.

[135] R. Motwani and P. Raghavan. *Randomized Algorithms*. Cambridge University Press, 1995.

[136] J. P. Straley. Third Virial Coefficient for the Gas of Long Rods. *Molecular Crystals and Liquid Crystals*, 24:1835, 1973.

[137] Z. Y. Chen. Nematic ordering in semiflexible polymer chains. *Macromolecules*, 26:3419, 1993.

[138] M. Dijkstra and D. Frenkel. Simulation study of the isotropic-to-nematic transitions of semiflexible polymers. *Physical Review E*, 51:5891, 1995.

[139] H. N. W. Lekkerkerker, P. Coulon, R. Van der Haegen, and R. Deblieck. On the isotropic liquid crystal phase separation in a solution of rodlike particles of different lengths. *J. Chem. Phys.*, 80:3427, 1984.

[140] M. A. Cotter and D. C. Wacker. Van der Waals theory of nematogenic solutions. I. Derivation of the general equations. *Physical Review A*, 18:2669, 1978.

[141] H. Hansen-Goos and K. Mecke. Fundamental Measure Theory for Inhomogeneous Fluids of Nonspherical Hard Particles. *Physical Review Letters*, 102:018302, 2009.

[142] R. H. J. Otten and P. van der Schoot. Capillary rise of an isotropic-nematic fluid interface: surface tension and anchoring versus elasticity. *Langmuir : the ACS journal of surfaces and colloids*, 25:2427, 2009.

[143] S. Wolfsheimer, C. Tanase, K. Shundyak, R. van Roij, and T. Schilling. Isotropic-nematic interface in suspensions of hard rods: Mean-field properties and capillary waves. *Physical Review E*, 73:061703, 2006.

[144] A. G. Kalugin. Waves on the interface between a nematic liquid crystal and an ideal isotropic fluid. *Fluid Dynamics*, 46:953, 2012.

[145] W. E. McMullen and K. F. Freed. A density functional theory of polymer phase transitions and interfaces. *The Journal of Chemical Physics*, 92:1413, 1990.

[146] Z. Y. Chen and J. Noolandi. Numerical solution of the Onsager problem for an isotropic-nematic interface. *Physical Review A*, 45:2389, 1992.

[147] K. Shundyak and R. Van Roij. Isotropic-nematic interfaces of hard-rod fluids. *Journal of Physics: Condensed Matter*, 13:4789, 2001.

[148] M. Allen. Molecular simulation and theory of the isotropicnematic interface. *The Journal of Chemical Physics*, 112:5447, 2000.

[149] A. McDonald, M. Allen, and F. Schmid. Surface tension of the isotropic-nematic interface. *Physical Review E*, 63:010701, 2000.

[150] J. Elgeti and F. Schmid. Nematic liquid crystals at rough and fluctuating interfaces. *The European physical journal. E, Soft matter*, 18:407, 2005.

[151] M. P. Lettinga. Dynamics and Flow Behaviour of Colloidal Rod-like particles. Technical report, 2010.

[152] H. Hemmen, N. I. Ringdal, E. N. De Azevedo, M. Engelsberg, E. L. Hansen, Y. Méheust, J. O. Fossum, and K. D. Knudsen. The isotropic-nematic interface in suspensions of Na-fluorohectorite synthetic clay. *Langmuir : the ACS journal of surfaces and colloids*, 25:12507, 2009.

[153] D. van der Beek, H. Reich, P. van der Schoot, ., M. Dijkstra, T. Schilling, R. Vink, M. Schmidt, R. van Roij, and H. N. W. Lekkerkerker. Isotropic-Nematic Interface and Wetting in Suspensions of Colloidal Platelets. *Physical Review Letters*, 97:087081, 2006.

[154] S. Faetti and V. Palleschi. Nematic-isotropic interface of some members of the homologous series of 4-cyano-4â-(n-alkyl) biphenyl liquid crystals. *Physical Review A*, 30:3241, 1984.

[155] D. Langevin and M. A. Bouchiat. Molecular Order and Surface Tension for the Nematic-Isotropic Interface of MBBA, deduced from Light Reflectivity and Light Scattering Measurements. *Molecular Crystals and Liquid Crystals*, 22:317, 1973.

[156] A. A. Verhoeff, R. H. J. Otten, P. van der Schoot, and H. N. W. Lekkerkerker. Magnetic field effects on tactoids of plate-like colloids. *The Journal of chemical physics*, 134:044904, 2011.

[157] Z. Dogic, K. Purdy, E. Grelet, M. Adams, and S. Fraden. Isotropic-nematic phase transition in suspensions of filamentous virus and the neutral polymer Dextran. *Physical Review E*, 69:051702, 2004.

[158] Z. Dogic. Surface Freezing and a Two-Step Pathway of the Isotropic-Smectic Phase Transition in Colloidal Rods. *Physical Review Letters*, 91:165701, 2003.

[159] M. P. Lettinga, K. Kang, A. Imhof, D. Derks, and J. K. G. Dhont. Kinetic pathways of the nematicisotropic phase transition as studied by confocal microscopy on rod-like viruses. *Journal of Physics: Condensed Matter*, 17:3609, 2005.

[160] M. P. Lettinga, K. Kang, P. Holmqvist, A. Imhof, D. Derks, and Jan Dhont. Nematic-isotropic spinodal decomposition kinetics of rodlike viruses. *Physical Review E*, 73:011412, 2006.

[161] P. Holmqvist, M. Ratajczyk, G. Meier, H. H. Wensink, and M. P. Lettinga. Supersaturated dispersions of rodlike viruses with added attraction. *Physical Review E*, 80:031402, 2009.

[162] G. J. Vroege and H. N. W. Lekkerkerker. Phase transitions in lyotropic colloidal and polymer liquid crystals. *Rep. Prog. Phys.*, 55, 1992.

[163] J. E. Mayer and M. G. Mayer. *Statistical Mechanics*. New York: Wiley, 1940.

[164] J. P. Straley. Frank Elastic Constants of the Hard-Rod Liquid Crystal. *Physical Review A*, 8:2181, 1973.

[165] D. Frenkel. Onsager's spherocylinders revisited. *Journal of physical chemistry*, 91:4912, 1987.

[166] T. Odijk. Theory of lyotropic polymer liquid crystals. *Macromolecules*, 19:2313, 1986.

[167] J. D. Van der Waals. The thermodynamic theory of capillarity under the hypothesis of a continuous variation of density. *Verh. Konink. Akad. Weten. Amsterdam (Sect. 1)*, 1, 1893.

[168] J. S. Rowlinson and B. Widom. *Molecular Theory of Capillarity*. Claredon Press, 1982.

[169] J. Tang and S. Fraden. Magnetic-field-induced isotropic-nematic phase transition in a colloidal suspension. *Physical review letters*, 71:3509, 1993.

[170] C. Martin, H. Kramer, C. Johner, B. Weyerich, J. Biegel, R. Deike, M. Hagenbuchle, and R. Weber. Electric and magnetic field studies on rodlike fd-virus suspensions. *Macromolecules*, 28:3175, 1995.

[171] P. Patrício, N.M. Silvestre, C. T. Pham, and J. Romero-Enrique. Filling and wetting transitions of nematic liquid crystals on sinusoidal substrates. *Physical Review E*, 84:021701, 2011.

Publications

To date the following publications based upon work in this thesis have been submitted or are in preparation:

Oliver J. Dammone, Ioannis Zacharoudiou, Roel P. A. Dullens, Julia M. Yeomans, M.P. Lettinga, and Dirk G. A. L. Aarts, *Confinement Induced Splay-to-Bend Transition of Colloidal Rods*, Phys. Rev. Lett. 109, 108303 (2012). (Chapter 3)

Oliver J. Dammone, Ioannis Zacharoudiou, Roel P. A. Dullens, Julia M. Yeomans, M.P. Lettinga, and Dirk G. A. L. Aarts, *Effect of rod stiffness on the splay to bend transition of colloidal rods*, about to be submitted. (Chapter 3)

Oliver J. Dammone, Alex Lewis, Jose Alvarado, Gijsje H. Koenderink, Apala Majumdar, M.P. Lettinga, and Dirk G. A. L. Aarts, *Colloidal liquid crystals in rectangular confinement*, in preparation. (Chapter 5)

Ioana C. Garlea, Pieter Mulder, Jose Alvarado, Oliver J. Dammone, Dirk G. A. L. Aarts, M. Pavlik Lettinga, Gijsje H. Koenderink, Bela M. Mulder, *Strong confinement induces defect-mediated domain structures in colloidal liquid crystals*, about to be submitted. (Chapter 6)

Brief Biography

I was born in Leeds, UK to Karen and Luciano Dammone. When I was three my sister Harriet joined me. I spent my whole childhood in Yorkshire, firstly in Leeds and then in Harrogate. It was a great place to grow up. For senior school I attended Leeds Grammar School. In hindsight, I probably worked a little bit too hard and was a bit too serious. At eighteen I left home to start a Chemistry degree at University College, Oxford. Most of term time was spent on the river and discovering girls, something my all male school had not prepared me for. In contrast to term time, most of the holidays were spent frantically working and revising giving my parents the impression I was a diligent student. After the fun of my undergraduate degree it was an easy choice to stay on for a DPhil. Doing a DPhil was very rewarding, but also challenging and frustrating. I have great memories of a conference in Granada, the conference was good, but the cycling even better... The most productive period of my DPhil was a trip to the AMOLF, Amsterdam. During this trip somehow all my experiments worked, it was fantastic, and obviously Amsterdam was a great city to explore once we had finally left the lab.

After seven and half years it is time for a change, and I now leave Oxford and Chemistry to work as in the field of cyber security. However, the people I have met, and the ideas I have heard while in Oxford, will have a huge effect on how I live the rest of my life.

Acknowledgments

I can not thank Dirk Aarts enough. His style suited me down to the ground: he was very approachable, full of ideas, and would always make time to discuss. I would not have had such an enjoyable and productive DPhil without him. I owe equal thanks to Pavlik Lettinga. His expert knowledge and constant enthusiasm were crucial to my DPhil.

The reason I joined the Aarts group was because of Bob Thomas's recommendation. I thank Bob, for his great choice.

A huge thank you to my fellow DPhil/PhD students who I worked on problems with: Ioannis Zacharoudiou, José Alvarado, and Alex Lewis. We started as colleagues, but finish as friends.

Thinking back to my Masters year, I have a lot of fantastic memories. I can not forget Adam, Phoenix, and Adam.

Julia Yeomans is thanked for many discussions and critical reading of manuscripts. Roel Dullens is thanked for his input and always being a friendly face. Lia Verhoeff is thanked for always having the time to share her knowledge of liquid crystals. Working with all the past and current members of the Soft Matter group has always put a smile on my face, especially: Min, Tom, Manolis (Julich), Raam, Harry, Mike, Alice, Sam, Oli B, Francois, Paola, and Arran. I want to wish good luck to Kira and Huzaifah. Go Team Rod.

The best part of my DPhil has been meeting Julia. She has showed me what life is all about.

Finally, I must thank my parents and Harriet. They have always given me unconditional love and support in whatever I have chosen to do, and this DPhil has been no different. I would never achieved what I have without them. This thesis is dedicated with love to them.

One of the things I have learnt during my DPhil is that acknowledgments are one of the few pages of a thesis that people actually read. If this is the case with the current reader, I would like to let you know that chapter 3 is my favourite chapter.